CHAPTER

3

Seismic Sources and Source Parameters

Peter Bormann, Michael Baumbach, Günther Bock, Helmut Grosser,
George L. Choy and John Boatwright

3.1 Introduction to seismic sources and source parameters
(P. Bormann)

3.1.1 Types and peculiarities of seismic source processes

Fig. 3.1 depicts the main kinds of sources which generate *seismic waves* (see Chapter 2). Seismic waves are oscillations due to elastic deformations which propagate through the Earth and can be recorded by *seismographic sensors* (see Chapter 5). The energy associated with these sources can have a tremendous range and, thus, can have a wide range of *intensities* (see Chapter 12) and *magnitudes* (see 3.2 below).

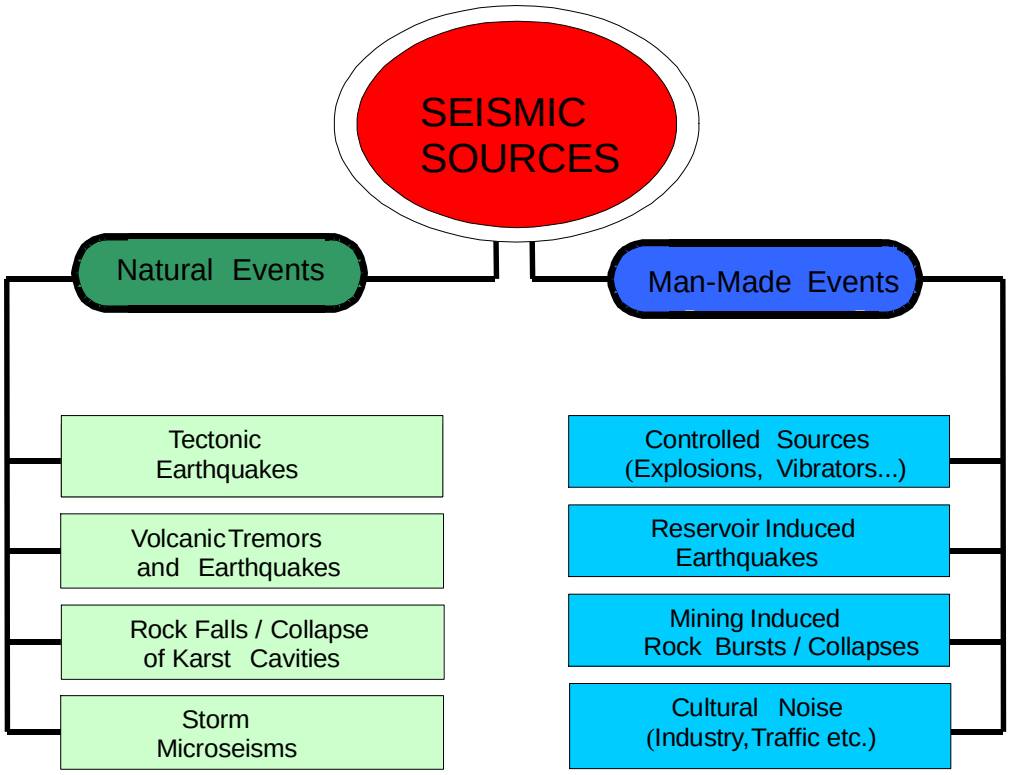

Fig. 3.1 Schematic classification of various kinds of events which generate seismic waves.

3.1.1.1 Tectonic earthquakes

Tectonic earthquakes are caused when the brittle part of the Earth's crust is subjected to stress that exceeds its breaking strength. Sudden rupture will occur, mostly along pre-existing faults or sometimes along newly formed faults. Rocks on each side of the rupture "snap" into a new position. For very large earthquakes, the length of the ruptured zone may be as much as 1000 km and the slip along the fault can reach several meters.

Laboratory experiments show that homogeneous consolidated rocks under pressure and temperature conditions at the Earth's surface will fracture at a volume strain on the order of 10^{-2} - 10^{-3} (i.e., about 0.1 % to 1% volume change) depending upon their porosity. Rock strength is generally smaller under tension or shear than under compression. Shear strains on the order of about 10^{-4} or less may cause fracturing of solid brittle rock. Rock strength is further reduced if the rock is pre-fractured, which is usually the case in the crust. The strength of pre-fractured rock is much less than that of unbroken competent rock and is mainly controlled by the frictional resistance to motion of the two sides of the fault. Frictional resistance, which depends on the orientation of the faults with respect to the stress field and other conditions (see Scholz, 1990), can vary over a wide range. Accordingly, deformations on the order of only 10^{-5} to 10^{-7}, which correspond to bending of a lithospheric plate by about 0.1 mm to 1 cm over a distance of 1 km, may cause shear faulting along pre-existing zones of weakness. But the shear strength depends also on the composition and fabric (anisotropy) of rock, its temperature, the confining pressure, the rate of deformation, etc. as well as the total cumulative strain. More details on the physics of earthquake faulting and related geological and seismotectonic conditions in the real Earth can be found in Scholz (1990) and in section 3.1.3 on *Source representation.* Additional recommended overview articles on the rheology of the stratified lithosphere and its relation to crustal composition, age and heat flow were published by Meissner and Wever (1988), Ranalli and Murphy (1987) and Wever et al. (1987). They also explain the influence of these parameters on the thickness and maximum depth of the seismogenic zone in the crust, i.e., the zone within which brittle fracturing of the rocks is possible when the strains exceed the breaking strength or elastic limit of the rock (see Fig. 2.1).

The break-up of the lithosphere into plates due to deformation and stress loading is the main cause of tectonic earthquakes. The plates are driven, pushed and pulled by the slow motion of convection currents in the more plastic hot material of the mantle beneath the lithosphere. These relative motions are in the order of several cm per year. Fig. 3.2 shows the global pattern of earthquake belts and the major tectonic plates. There are also numerous small plates called sub- or micro-plates. Shallow earthquakes, within the upper part of the crust, take place mainly at plate boundaries but may also occur inside plates (interplate and intraplate earthquakes, respectively). Intermediate (down to about 300 km) and deep earthquakes (down to a maximum of 700 km depth) occur under ocean trenches and related subduction zones where the lithosphere plates are thrusted or pulled down into the upper mantle. The major trenches are found around the Circum-Pacific earthquake and volcanic belt (see Fig. 3.2). However, intermediate and deep earthquakes may occur also in some other marine or continental collision zones (e.g., the Tyrrhenian and Aegean Sea or the Carpathians and Hindu Kush, respectively).

Most earthquakes occur along the main plate boundaries. These boundaries constitute either zones of extension (e.g., in the up-welling zones of the mid-oceanic ridges or intra-plate rifts), transcurrent shear zones (e.g., the San Andreas fault in the west coast of North America or the

North Anatolian fault in Turkey), or zones of plate collision (e.g., the Himalayan thrust front) or subduction (mostly along deep sea trenches). Accordingly, tectonic earthquakes may be associated with many different faulting types (strike-slip, normal, reverse, thrust faulting or mixed; see Figs. 3.32 and 3.33 in 3.4.2).

The largest strain rates are observed near active plate boundaries (about 10^{-8} to 3×10^{-10} per year). Strain rates are significantly less in active plate interiors (about 5×10^{-10} to 3×10^{-11} per year) or within stable continental platforms (about 5×10^{-11} to 10^{-12} per year) (personal communication by Giardini, 1994). Consequently, the critical cumulative strain for the pre-fractured/faulted seismogenic zone of lithosphere, which is on the order of about 10^{-6} to 10^{-7}, is reached roughly after some 100, 1000 to 10,000 or 10,000 to 100,000 years of loading, respectively. This agrees well with estimates of the mean return period of the largest possible events (seismic cycles) in different plate environments (Muir-Wood ,1993; Scholz, 1990).

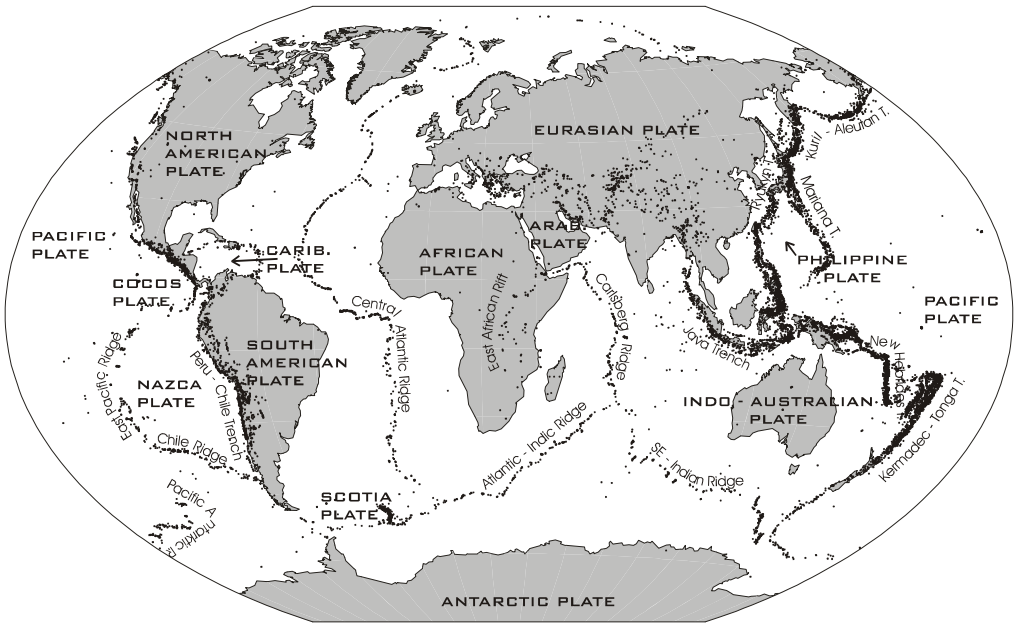

Fig. 3.2 Global distribution of earthquake epicenters according to the data catalog of the United States National Earthquake Information Center (NEIC), January 1977 to July 1997, and the related major lithosphere plates.

Although there are hundreds of thousands of weak tectonic earthquakes globally every year, most of them can only be recorded by sensitive nearby instruments. But in the long-term global statistical average about 100,000 earthquakes are strong enough ($M \geq 3$) to be potentially perceptible by humans in the near-source area. A few thousand are strong enough ($M \geq 5$) to cause slight damage and some 100 with magnitude $M > 6$ can cause heavy damage, if there are nearby settlements and built-up areas; while about 1 to 3 events every year (with $M \geq 8$) may result in wide-spread devastation and disaster. During the 20th century the 1995 Great Hanshin/Kobe earthquake caused the greatest economic loss (about 100 billion US$), the 1976 Tangshan earthquake inflicted the most terrible human loss (about 243,000 people killed) while the Chile earthquake of 1960 released the largest amount of *seismic energy* E_S (see 3.1.2.2 below) of about $5\cdot10^{18}$ to 10^{19} Joule. The latter corresponds to about 25 to 100 years of the long-term annual average of global seismic energy release which is about $1 - 2 \times 10^{17}$ J (Lay and Wallace, 1995) and to about half a year of the total kinetic energy

contained in the global lithosphere plate motion. The total *seismic moment* (see 3.1.2.3. below) of the Chile earthquake was about 3×10^{23} Nm. It ruptured about 800 - 1000 km of the subduction zone interface at the Peru-Chile trench in a width of about 200 km (Boore 1977; Scholz 1990). In summary: about 85 % of the total world-wide seismic moment release by earthquakes occurs in subduction zones and more than 95 % by shallow earthquakes along plate boundaries. The other 5 % are distributed between intraplate events and deep and intermediate focus earthquakes. The single 1960 Chile earthquake accounts for about 25 % of the total seismic moment release between 1904 and 1986.

It should be noted that most of the total energy release, $E_{T,}$ is required to power the growth of the earthquake fracture and the production of heat. Only a small fraction of $E_T = E_S + E_f$ (with E_f - friction energy) goes into producing seismic waves. The seismic efficiency, i.e., the ratio of E_S/E_T , is perhaps only about 0.01 to 0.1. It depends both on the *stress drop* during the rupture as well as on the total stress in the source region (Spence, 1977; Scholz, 1990).

3.1.1.2 Volcanic earthquakes

Although the total energy released by the strongest historically known volcanic eruptions was even larger than E_T of the Chile earthquake, the seismic efficiency of volcanic eruptions is generally much smaller, due to their long duration. Nevertheless, in some cases, volcanic earthquakes may locally reach the shaking strength of destructive earthquakes (e.g., *magnitudes* of about 6; see 3.1.2.2). Most of the seismic oscillations produced in conjunction with sub-surface magma flows are of the tremor type, i.e., long-lasting and more or less monochromatic oscillations which come from a two- or three-phase (liquid- and/or gas-solid) source process which is not narrowly localized in space and time. They can not be analyzed in the traditional way of seismic recordings from tectonic earthquakes or explosions nor with traditional source parameters (see Chapter 13). Volcanic earthquakes contribute only an insignificant amount to the global seismic moment release (see Scholz 1990).

3.1.1.3 Explosions, implosions and other seismic events

Explosions are mostly anthropogenic, i.e., “man-made”, and controlled, i.e., with known location and source time. However, strong natural explosions in conjunction with volcanic eruptions or meteorite impacts, such as the Tunguska meteorite of 30 June 1908 in Siberia, may also occur. Explosions used in exploration seismology for the investigation of the crust have yields, Y, of a few kg to tons of TNT (Trinitrotoluol). This is sufficient to produce seismic waves which can be recorded from several km to hundreds of km distance. Underground nuclear explosions of kt up to Mt of equivalent TNT may be seismically recorded even world-wide (1 kt TNT = 4.2 x 10^{12} J). Nevertheless, even the strongest of all underground nuclear tests with an equivalent yield of about 5 Mt TNT produced body-waves of only magnitude mb ≈ 7. This corresponds to roughly 0.1% of the seismic energy released by the Chile earthquake of 1960. After 1974, underground tests with only Y ≤ 150 kt were carried out. Only well contained underground chemical or nuclear explosions have a sufficiently good seismic coupling factor ε (ε ≈ 10^{-2} to 10^{-3}, i.e., only 1 % to 0.1 % of the total released explosion energy is transformed into seismic energy). The coupling factor of explosions on the surface or in the atmosphere is much less (ε ≈ 10^{-3} to 10^{-6} depending on the altitude).

Fig. 3.3 depicts schematically an idealized sub-surface explosion and tectonic earthquake (of pure strike-slip type) in a homogeneous medium.

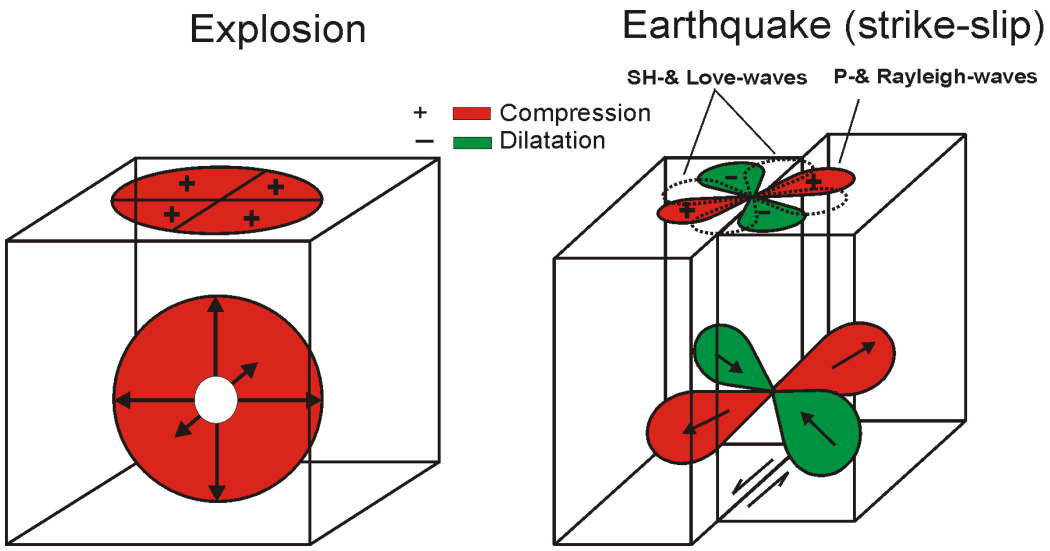

Fig. 3.3 Schematic sketches of an idealized underground explosion and of a strike-slip earthquake along a vertically dipping fault. The fault motion is "left-lateral", i.e., counter-clockwise. The arrows show the directions of compressional (outward, polarity +, red shaded) and dilatational (inward, polarity -, green shaded) motions. The patterns shown on the surface, termed amplitude or polarity patterns indicate the azimuthal variation of observed amplitudes or of the direction of first motions in seismic records, respectively. While point-like explosions in an isotropic medium should show no azimuth-dependent amplitudes and compressional first motions only, amplitudes and polarities vary for a tectonic earthquake. The dotted amplitude lobes in Fig. 3.3, right side, indicate qualitatively the different azimuth dependence of shear (S) waves as compared to longitudinal (P) waves (rotated by 45°) but their absolute values are much larger (about 5 times) than that of P waves.

It is obvious that the explosion produces a homogeneous outward directed compressional first motion in all directions while the tectonic earthquake produces first motions of different amplitude and polarity in different directions. These characteristics can be used to identify the type of source process (see 3.4) and to discriminate between explosions and tectonic earthquakes.

Compared to tectonic earthquakes, the *duration* of the source process of explosions and the *rise time* to the maximum level of displacement is much shorter (milliseconds as compared to seconds up to a few minutes) and more impulsive (Fig. 3.4). Accordingly, explosions of comparable body-wave magnitude excite more high-frequent oscillations (see Fig. 3.5). Rock falls may last for several minutes and cause seismic waves but generally with less distinct onsets and less separation of wave groups.

The collapse of karst caves, mining-induced rock bursts or collapses of mining galleries are generally of an *implosion* type. Accordingly, their first motion patterns should show dilatations in all azimuths if a secondary tectonic event has not been triggered by the collapse. The strongest events may reach magnitudes up to about M = 5.5 and be recorded world-wide (e.g., Bormann et al., 1992). *Reservoir induced* earthquakes have been frequently observed in

conjunction with the impoundment of water or rapid water level changes behind large dams. Since these events are triggered along pre-existing and pre-stressed tectonic faults they show the typical polarity patterns of tectonic earthquakes (e.g., Fig. 3.3). The strongest events reported so far have reached magnitudes up to 6.5 (e.g., Koyna earthquake in 1967).

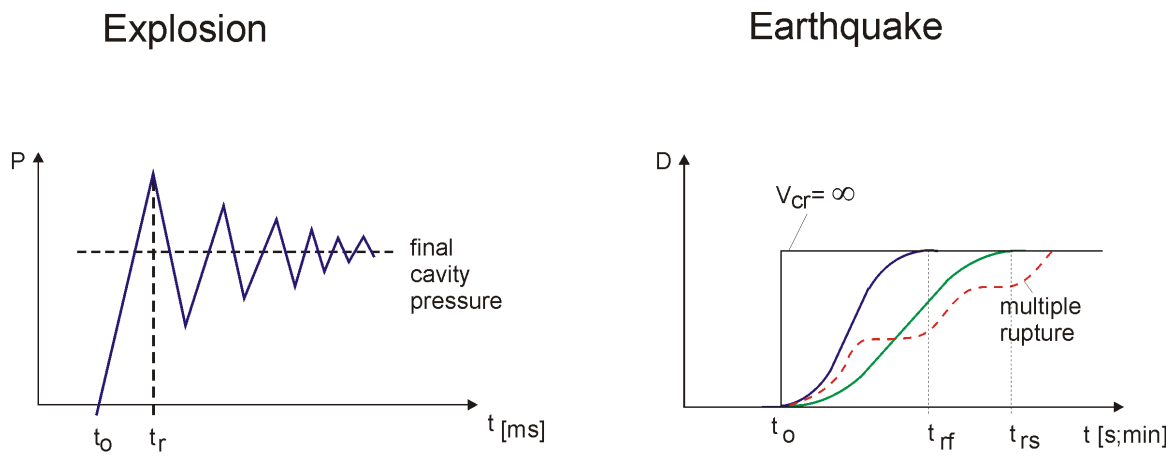

Fig. 3.4 Schematic diagrams of the different source functions of explosions (left) and earthquakes (right). P - pressure in the explosion cavity, D - fault displacement, t - time, t_0 - origin time of the event, t_r - rise time of P or D to its maximum values, t_{rf} - rise time of fast rupture, t_{rs} - rise time of slow rupture; the step function in the right diagram would correspond to an earthquake with infinite velocity of crack propagation v_{cr}. Current rupture models assume v_{cr} to be about 0.6 to 0.9 times of the velocity of shear-wave propagation, v_s.

3.1.1.4 Microseisms

Very different seismic signals are produced by storms over oceans or large water basins (seas, lakes, reservoirs) as well as by wind action on topography, vegetation or built-up surface cover. These seismic signals are called *microseisms*. Seismic signals due to human activities such as rotating or hammering machinery, traffic etc., are *cultural seismic noise*. Rushing waters or gas/steam (in rivers, water falls, dams, pipelines, geysers) may be additional sources of natural or anthropogenic *seismic noise*. They are not well localized in space nor fixed to a defined *origin time*. Accordingly, they produce more or less permanent on-going non-coherent interfering signals of more or less random amplitude fluctuations in a very wide frequency range of about 16 octaves (about 50 Hz to 1 mHz) which are often controlled in their intensity by the season (natural noise) or time of day (anthropogenic noise). Despite the large range of ambient noise displacement amplitudes (about 6 to 10 orders of magnitude; see Fig. 4.7) they are generally much smaller than those of earthquakes and not felt by people. The differences between signals from coherent seismic sources on the one hand and microseisms/seismic noise on the other hand are dealt with in more detail in Chapter 4.

3.1.2 Parameters which characterize size and strength of seismic sources

3.1.2.1 Macroseismic intensity

The effect of a seismic source may be characterized by its *macroseismic intensity*, **I**. Intensity describes the strength of shaking in terms of human perception, damage to buildings and other

structures, as well as changes in the surrounding environment. **I** depends on the distance from the source and the soil conditions and is mostly classified according to macroseismic scales of 12 degrees (e.g., Grünthal, 1998). From an analysis of the areal distribution of felt reports and damage one can estimate the epicentral intensity $\mathbf{I_0}$ in the source area as well as the source depth, h. There exist empirical relationships between $\mathbf{I_0}$ and other instrumentally determined measures of the earthquake size such as the *magnitude* and ground acceleration. For more details see Chapter12.

3.1.2.2 Magnitude and seismic energy

Magnitude is a logarithmic measure of the size of an earthquake or explosion based on instrumental measurements. The magnitude concept was first proposed by Richter (1935). Magnitudes are derived from ground motion amplitudes and periods or from *signal duration* measured from instrumental records. There is no *a priori* scale limitation to magnitudes as exist for macroseismic intensity scales. Magnitudes are often misleadingly referred to in the press as "... according to the open-ended RICHTER scale...". In fact, the maximum size of tectonic earthquakes is limited by nature, i.e., by the maximum size of a brittle fracture in a finite and heterogeneous lithospheric plate. The largest moment magnitude, Mw, observed so far was that of the Chile earthquake in 1960 ($M_w \approx 9.5$; Kanamori 1977). On the other hand, the magnitude scale is open at the lower end. Nowadays, highly sensitive instrumentation close to the sources may record events with magnitude smaller than zero. According to Richter´s original definition these magnitude values become negative. With empirical *energy-magnitude-relationships* the *seismic energy*, E_S radiated by the seismic source as seismic waves can be estimated. Common relationships are those given by Gutenberg and Richter (1954, 1956) between E_S and the surface-wave magnitude M_S and the body-wave magnitude mB: $\log E_S = 11.8 + 1.5$ Ms and $\log E_S = 5.8 + 2.4$ mB, respectively (when E_S is given in erg; 1 erg = 10^{-7} Joule). According to the first relationship, a change of M by two units corresponds to a change in E_S by a factor of 1000. Based on the analysis of digital recordings, there exist also direct procedures to estimate E_S (e.g., Purcaru and Berckhemer, 1978; Seidl and Berckhemer, 1982; Boatwright and Choy, 1986; Kanamori et al., 1993; Choy and Boatwright, 1995) and to define an "energy magnitude" Me (see 3.3). Since most of the seismic energy is concentrated in the higher frequency part around the corner frequency of the spectrum, Me is a more suitable measure of the earthquakes' potential for damage. In contrast, the seismic moment (see below) is related to the final static displacement after an earthquake and consequently, the moment magnitude, Mw, is more closely related to the tectonic effects of an earthquake.

3.1.2.3 Seismic source spectrum, seismic moment and size of the source area

Another quantitative measure of the size and strength of a seismic shear source is the scalar *seismic moment* M_0 (for its derivation see IS 3.1):

$$M_0 = \mu \, \overline{D} \, A \qquad (3.1)$$

with μ - rigidity or shear modulus of the medium, $\overline{D}$ - average final displacement after the rupture, A - the surface area of the rupture. M_0 is a measure of the irreversible inelastic deformation in the rupture area. This inelastic strain is described in (1) by the product $\overline{D}$ A. On the basis of reasonable average assumptions about μ and the stress drop $\Delta\sigma$ (i.e., with

$\Delta\sigma/\mu$ = constant) Kanamori (1977) derives the relationship $E_S = 5\times10^{-5} M_0$ (in J). More information about the deformation in the source is described by the *seismic moment tensor* (IS 3.1). Its determination is now standard in the routine analysis of strong earthquakes by means of waveform inversion of long-period digital records (see 3.5).

In a homogeneous half-space M_0 can be determined from the spectra of seismic waves observed at the Earth's surface by using the relationship:

$$M_0 = 4\pi\, d\, \rho\, v^3_{p,s}\, u_0 / R^{p,s}_{\theta,\varphi} \qquad (3.2)$$

with: d - hypocentral distance between the event and the seismic station; ρ - average density of the rock and $v_{p,s}$ - velocity of the P or S waves around the source; $R^{p,s}_{\theta,\varphi}$ - a factor correcting the observed seismic amplitudes for the influence of the radiation pattern of the seismic source, which is different for P and S waves (see Figs. 3.3, 3.25 and 3.26), u_0 - the low-frequency amplitude level as derived from the seismic spectrum of P or S waves, corrected for the instrument response, wave attenuation and surface amplification. For details see EX 3.4.

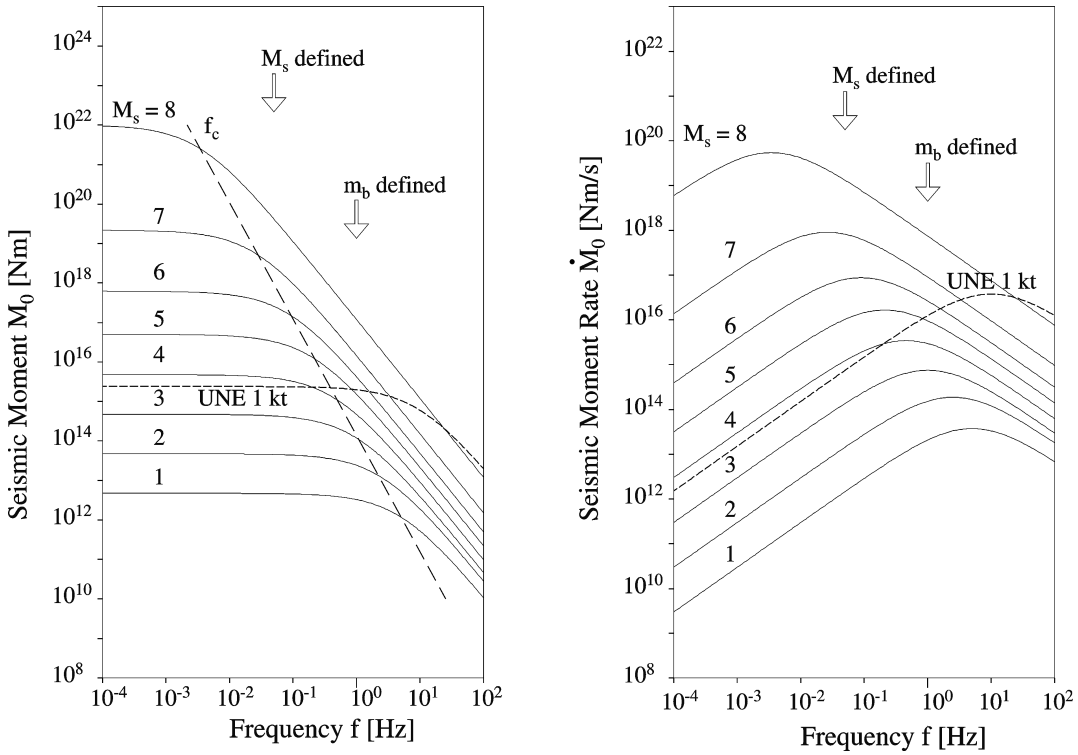

Fig. 3.5 "Source spectra" of ground displacement (left) and velocity (right) for a seismic shear source. "Source spectrum" means here the attenuation-corrected ground displacement *u(f)* or ground velocity $\dot{u}(f)$ respectively, multiplied by the factor $4\pi\, d\, \rho\, v^3_{p,s} / R^{p,s}_{\theta,\varphi}$. The ordinates do not relate to the frequency-dependent spectra proper but rather to the low-frequency scalar seismic moments or moment rates that correspond to the depicted spectra. The broken line (long dashes) shows the increase of corner frequency f_c with decreasing seismic moment of the event, the short-dashed line gives the approximate "source spectrum" for a well contained underground nuclear explosion (UNE) of an equivalent yield of 1 kt TNT. Note the plateau (u_o = const.) in the displacement spectrum towards low frequencies ($f < f_c$) and the high-frequency decay ~ f^2 for frequencies $f > f_c$.

According to Aki (1967) a simple seismic shear source with linear rupture propagation shows in the far-field smooth displacement and velocity spectra. When corrected for the effects of geometrical spreading and attenuation we get "source spectra" similar to the generalized ones shown in Fig. 3.5. There the low-frequency values have been scaled to the scalar seismic moment M_0 (left) and moment rate dM_0/dt (right), respectively. The given magnitude values Ms correspond to a non-linear Ms-log M_0 relationship which is based on work published by Berckhemer (1962) and Purcaru and Berckhemer (1978). Note that the 1960 Chile earthquake had a seismic moment M_0 of about $3 \cdot 10^{23}$ Nm and a "saturated" magnitude (see discussion below) of Ms = 8.5. This corresponds well with Fig. 3.5. There exist also other, non-linear empirical Ms-log M_0 relationships (e.g., Geller, 1976).

The following general features are obvious from Fig. 3.5:

- "source spectra" are characterized by a "plateau" of constant displacement for frequencies smaller than the "corner frequency" f_c which is inversely proportional to the source dimension, i.e., $f_c \sim 1/L$;
- the decay of spectral displacement amplitude beyond $f > f_c$ is proportional to f^{-2};
- the plateau amplitude increases with seismic moment M_0 and magnitude, while at the same time f_c decreases proportional to M_0^{-3} (see Aki, 1967);
- the surface-wave magnitude, Ms, which is, according to the original definition by Gutenberg (1945), determined from displacement amplitudes with frequencies around 0.05 Hz, is not linearly scaled with M_0 for Ms > 7. While for larger events the amplitudes in the spectral plateau, i.e., for $f < f_c$, still increase proportional to M_0 there is no further (or only reduced) increase in spectral amplitudes at frequencies $f > f_c$. Accordingly, for Ms > 7 these magnitudes are systematically underestimated as compared to moment magnitudes Mw determined from M_0 (see 3.2.5.3). No $M_S > 8.5$ has ever been measured although moment magnitudes up to 9.5 to 10 have been observed. This effect is termed *magnitude saturation*;
- this saturation occurs much earlier for mb, which is determined from amplitude measurements around 1 Hz. No mb > 7 has been determined from narrowband short-period recordings, even for the largest events;
- since wave energy is proportional to the square of ground motion particle velocity, i.e., $E_S \sim (2\pi f\, u)^2 = (\omega\, u(\omega))^2$, its maximum occurs at f_c;
- compared with an earthquake of the same seismic moment or magnitude, the corner frequency f_c of a well contained underground nuclear explosion (UNE) in hard rock is about ten times larger. Accordingly, an UNE produces relatively more high-frequent energy and thus has a larger E_S as compared with an earthquake of comparable magnitude mb.

The main causes for this difference in E_S and high-frequency content between UNE and earthquakes are:

- the *duration* of the source process or *rise time*, t_r, to the final level of static displacement is much shorter for the case of explosions than for earthquakes (see Fig. 3.4);
- the shock-wave front of an explosion, which causes the deformation and fracturing of the surrounding rocks and thus the generation of seismic waves, propagates with approximately the P-wave velocity v_p while the velocity of crack propagation along

a shear fracture/fault is only about 0.5 to 0.9 of the S-wave velocity, i.e., about 0.3 to 0.5 times that of v_p;

- the equivalent wave radiating surface area in the case of an explosion is a sphere $A = 4\pi r^2$ and not a plane $A = \pi r^2$. Accordingly, the equivalent source radius in the case of an explosion is smaller and thus the related corner frequency larger.

Note: Details of theoretical "source spectra" depend on the assumptions in the model of the rupture process, e.g., when the rupture is - more realistically - bilateral, the displacement spectrum of the source-time function is for $f >> f_c$ proportional to f^{-2}, whereas this high-frequency decay is proportional to f^{-3} for an unilateral rupture. On the other hand, when the linear dimensions of the fault rupture differ in length and width then two corner frequencies will occur. Another factor is related to the details of the source time function. Whether the two or three corner frequencies are resolvable will depend on their separation. In the case of real spectra derived from data limited in both time and frequency domain, resolvability will depend on the signal-to-noise ratio. Normally, real data are too noisy to allow the discrimination between different types of rupture propagation and geometry.

The general shape of the seismic source spectra can be understood as follows: We know from optics that under a microscope no objects can be resolved which are smaller than the wavelength λ of the light with which it is observed. In this case the objects appear as a blurred point or dot. In order to resolve more details, electron microscopes are used which operate with much smaller wavelength. The same holds true in seismology. When observing a seismic source of radius r with wavelengths $\lambda >> r$ at a great distance, one can not see any information about the details of the source process. One can only see the overall (integral) source process, i.e., one "sees" a point source. Accordingly, spectral amplitudes with these wavelengths are constant and form a spectral plateau (if the source duration can be neglected). On the other hand, wavelengths that have $\lambda << r$ can resolve internal details of the rupture process. In the case of an earthquake they correspond to smaller and smaller elements of the rupture processes or of the fault roughness (asperities and barriers). Therefore, their spectral amplitudes decay rapidly with higher frequencies. The corner frequency, f_c , marks a critical position in the spectrum which is obviously related to the size of the source. According to Brune (1970) and Madariaga (1976), both of whom modeled a circular fault, the corner frequency in the P- or S-wave spectrum, respectively, is $f_{c\ p/s} = c_m\ v_{p,s} / \pi\ r$. In contrast, assuming a rectangular fault, Haskell (1964) gives the relationship $f_{c\ p/s} = c_m\ v_{p,s} / (L \times W)^{1/2}$ with L the length and W the width of the fault. The values c_m are model dependent constants. Accordingly, the critical wavelength $\lambda_c = v/ f_c$, beyond which the source can be realized as a point source only, is $\lambda_c = c_m\ \pi\ r$ or $\lambda_c = c_m\ (L \times W)^{1/2}$, respectively.

Thus, from both the source area (which, of course, is based on model assumptions of the shape of the rupture) and the seismic moment from seismic spectra, one can estimate from Eq. (3.1) the average total displacement, $\overline{D}$. Knowing $\overline{D}$, other parameters such as the *stress drop* in the source area can be inferred. Stress drop means the difference in acting stress at the source region before and after the earthquake. For more details see Figure 10 in IS 3.1 and for practical determination the exercise EX 3.4.

3.1.2.4 Orientation of the fault plane and the fault slip

Assuming that the earthquake rupture occurs along a planar fault surface the orientation of this plane in space can be described by three angles: *strike* ϕ (0° to 360° clockwise from

north), *dip* δ (0° to 90° against the horizontal) and the direction of slip on the fault by the *rake angle* λ (- 180° to + 180° against the horizontal). Fig**.** 3.30 and 3.31 in section 3.4.2 define these angles and show how to determine them from a stereographic (Wulff) net or equal area (Lambert-Schmidt) projection using observations of first motion polarities. It can be shown that a rupture along a plane perpendicular to the above mentioned fault plane with a slip vector perpendicular to the slip on the first plane causes an identical angular distribution of first motions. Therefore, on the basis of first motion analysis alone one can not decide which of the two planes is the true fault plane.

Note that in the case of a shear model the fault-plane solution (i.e., the information about the orientation of the fault plane and of the fault slip in space) forms, together with the information about the static seismic moment M_0 (see 3.1.2.3), the seismic moment tensor M_{ij} (see Equation (25) in IS 3.1). Its principal axes coincide with the direction of the pressure axis, P, and the tension axis, T, associated with fault-plane solutions. They should not be mistaken for the principal axes σ_1, σ_2 and σ_3 (with $\sigma_1 > \sigma_2 > \sigma_3$) of the acting stress field in the Earth which is described by the stress tensor. Only in the case of a fresh crack in a homogeneous isotropic medium in a whole space with no pre-existing faults and vanishing internal friction is P in the direction of σ_1 while T has the opposite sense of σ_3. P and T are perpendicular to each other and each one forms, under the above conditions, an angle of 45° with the two possible conjugate fault planes (*45°-hypothesis*) which are in this case perpendicular to each other (see Figs. 3.24 and 3.31 in 3.4). The orientation of P and T is also described by two angles each: the azimuth and the plunge. They can be determined by knowing the respective angles of the fault plane (see EX 3.2). If the above model assumptions hold true, one can, knowing the orientation of P and T in space, estimate the orientations of σ_1 and σ_3. Most of the data used for compiling the global stress map (Zoback 1992) come from earthquake fault-plane solutions calculated under these assumptions.

In reality, the internal friction of rocks is not zero. For most rocks this results, according to Andersons´s theory of faulting (1951), in the formation of conjugate pairs of faults which are oriented at about ± 30° to σ_1. In this case, the directions of P and T, as derived from fault-plane solutions, will not coincide with the principal stress directions. Near the surface of the Earth one of the principal stresses is almost always vertical. In the case of a horizontal compressive regime, the minimum stress σ_3 is vertical while σ_1 is horizontal. This results, when fresh faults are formed in unbroken rock, in thrust faults dipping about 30° and striking parallel or anti-parallel to σ_2. In an extensional environment, σ_1 is vertical and the resulting dip of fresh normal faults is about 60°. When both σ_1 and σ_3 are horizontal, vertical strike-slip faults will develop, striking with ± 30° to σ_1. But most earthquakes are associated with the reactivation of pre-existing faults rather than occurring on fresh faults. Since the frictional strength of faults is generally less than that of unbroken rock, faults may be reactivated at angles between σ_1 and fault strike that are different from 30°. In a pre-faulted medium this tends to prevent failure on a new fault. Accordingly, there is no straightforward way to infer from the P and T directions determined for an individual earthquake the directions of the acting principal stress. On the other hand, it is possible to infer the regional stress based on the analysis of many earthquakes in that region since the possible suite of rupture mechanisms activated by a given stress regime is constrained. This method aims at finding an orientation for σ_1 and σ_3 which is consistent with as many as possible of the actually observed fault-plane solutions (e.g., Gephart and Forsyth, 1984; Reches, 1987; Rivera, 1989).

3.1.3 Mathematical source representation

It is beyond the scope of the NMSOP to dwell on the physical models of seismic sources and their mathematical representation. There exists quite a number of good text books on these issues (e.g., Aki and Richards, 1980 and 2002; Ben-Menahem and Singh, 1981; Das and Kostrov, 1988; Scholz, 1990; Lay and Wallace, 1995; Udías, 1999). However, most of these texts are rather elaborate and more research oriented. Therefore, we have appended a more concise introduction into the theory of source representation in IS 3.1. It outlines how the basic relationships used in practical applications of source parameter determinations have been derived, on what assumptions they are based and what their limitations are.

3.1.4 Detailed analysis of rupture kinematics and dynamics in space and time

Above we have considered earthquake models to derive suitable parameters for describing the size and behavior of faulting of earthquakes and to some extent also of explosions. In actuality, earthquakes do not rupture along perfect planes, nor are their rupture areas circular or rectangular. They do not occur in homogeneous rock, nor do they slip unilaterally or bilaterally. All these features are at best first order approximations or simplifications to the truth in order to make the problem mathematically and with limited data tractable. Real faults show jogs, steps, branching, splays, etc., both in their horizontal and vertical extent (Fig. 6). Such jogs and steps, depending on their severity, are impediments to smooth or ideal rupture, as are bumps or rough features along the contacting fault surfaces. More examples can be found in Scholz (1990). Since these features exist at all scales, which implies the self-similarity of fracture and faulting processes and their fractal nature, this will necessarily result in heterogeneous dynamic rupturing and finally also in rupture termination.

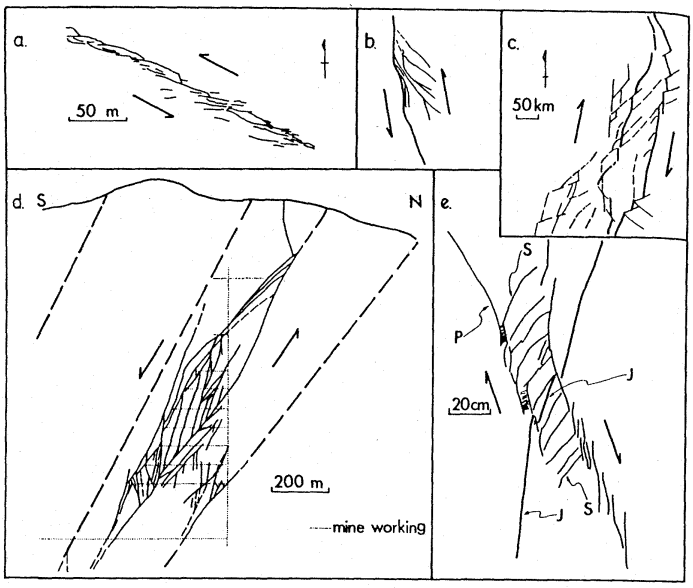

Fig. 3.6 Several fault zones mapped at different scales and viewed approximately normal to slip (from Scholz, The mechanics of earthquakes and faulting, 1990, Fig. 3.6, p. 106; with permission of Cambridge University Press).

As shown in Fig. 3.7 the complexity of the rupture process over time is a common feature of earthquakes, i.e., they often occur as multiple ruptures. This holds true for small earthquakes as well as very large earthquakes (Kikuchi and Ishida, 1993; Kikuchi and Fukao, 1987). And obviously, each event has its own "moment-rate fingerprint".

Only in a few lucky cases have dense strong-motion networks been fortuitously deployed in the very source region of a strong earthquake. Strong-motion records enable a detailed analysis of the rupture history in space and time using the moment-rate density. As an example, Fig. 3.8 depicts an inversion of data by Mendez and Anderson (1991) for the rupture process of the 1985 Michoacán, Mexico earthquake. Shown are snapshots, 4 s apart from each other, of the dip-slip velocity field. One recognizes two main clusters of maximum slip velocity being about 120 km and 30 s apart from each other. The related maximum cumulative displacement was more than 3 m in the first cluster and more than 4 m in the second cluster at about 55 km and 40 km depth, respectively. About 90 % of the total seismic moment was released within these two main clusters which had a rupture duration each of only 8 s while the total rupture lasted for about 56 s (Mendez and Anderson, 1991).

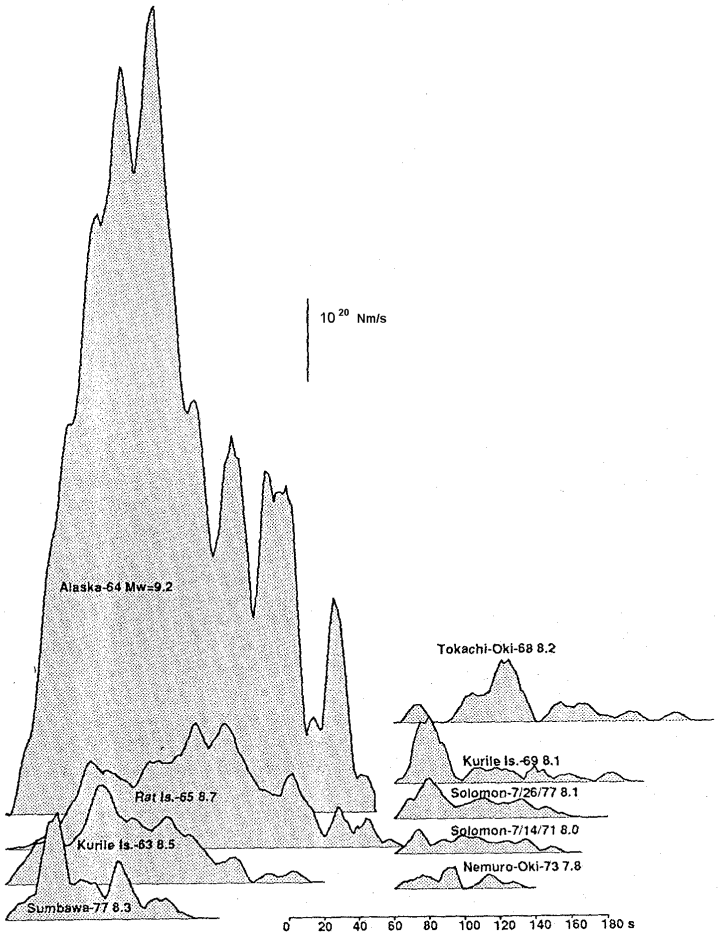

Fig. 3.7 Moment-rate (source time) functions for the largest earthquakes in the1960s and 1970s as obtained by Kikuchi and Fukao (1987) (modified from Fig. 9 in Kikuchi and Ishida, Source retrieval for deep local earthquakes with broadband records, Bulletin Seismological Society of America, Vol. 83, No. 6, p. 1868, 1993, © Seismological Society of America.

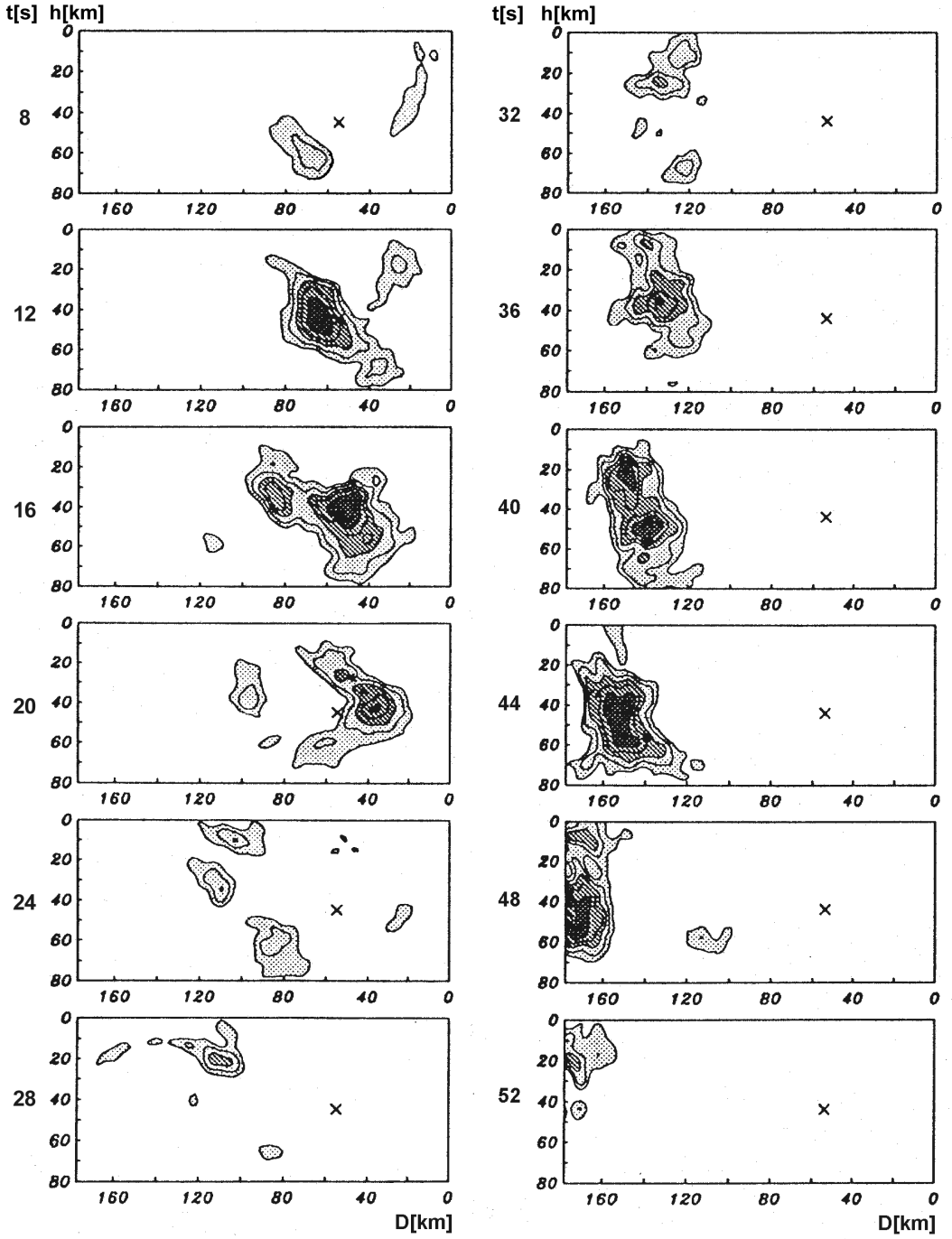

Fig. 3.8 Snapshots of the development in space and time of the inferred rupture process of the 1985 Michoacán, Mexico, earthquake. The contours represent dip-slip velocity at 5 cm/s interval, the cross denotes the NEIC hypocenter. Three consecutively darker shadings are used to depict areas with dip-slip velocities in the range: 12 to 22, 22 to 32, and greater than 32 cm/s, respectively. Abbreviations used: t - snapshot time after the origin time of the event, h - depth, D - distance in strike direction of the fault (redrawn and modified from Mendez and Anderson, The temporal and spatial evolution of the 19 September 1985 Michoacán earthquake as inferred from near-source ground-motion records, Bull. Seism. Soc. Am., Vol. 81, No. 3, Fig. 6, p. 857-858, 1991; © Seismological Society of America).

This rupturing of local asperities produces most of the high-frequency content of earthquakes. Accordingly, they contribute more to the cumulative seismic energy release than to the moment release. This is particularly important for engineering seismological assessments of expected earthquake effects. Damage to (predominately low-rise) structures is mainly due to frequencies > 2 Hz. They are grossly underestimated when analyzing strong earthquakes only on the basis of medium and long-period teleseismic records or when calculating model spectra assuming smooth rupturing along big faults of large earthquakes.

A detailed picture of the fracture process can be obtained only with dense strong-motion networks in source areas of potentially large earthquakes and by complementary field investigations and related modeling of the detailed rupture process in the case of clear surface expressions of the earthquake fault. Although this is beyond the scope of seismological observatory practice, observatory seismologists need to be aware of these problems and the limitations of their simplified standard procedures. Nevertheless, the value of these simplifications is that they allow a quick and rough first order analysis of the dominant type and orientation of earthquake faulting in a given region and their relationship to regional tectonics and stress field. The latter can also been inferred from other kinds of data such as overcoring experiments, geodetic data or field geological evidence. Their comparison with independent seismological data, which are mainly controlled by conditions at greater depth, may provide a deeper insight into the nature of the observed stress fields.

3.1.5 Summary and conclusions

The detailed understanding and quantification of the physical processes and geometry of seismic sources is one of the ultimate goals of seismology, be it in relation to understanding tectonics, improving assessment of seismic hazard or discriminating between natural and anthropogenic events. Earthquakes can be quantified with respect to various geometrical and physical parameters such as time and location of the (initial) rupture and orientation of the fault plane and slip, fault length, rupture area, amount of slip, magnitude, seismic moment, radiated energy, stress drop, duration and time-history (complexity) of faulting, particle velocity, acceleration of fault motion etc. It is impossible, to represent this complexity with just a single number or a few parameters.

There are different approaches to tackle the problem. One aims at the detailed analysis of a given event, both in the near- and far-field, analyzing waveforms and spectra of various kinds of seismic waves in a broad frequency range up to the static displacement field as well as looking into macroseismic data. Such a detailed and complex investigation requires a lot of time and effort. It is feasible only for selected important events. The second simplified approach describes the seismic source only by a limited number of parameters such as the origin time and (initial rupture) location, magnitude, intensity or acceleration of observed/ measured ground shaking, and sometimes the fault-plane solution. These parameters can easily be obtained and have the advantage of rough but quick information being given to the public and concerned authorities. Furthermore, this approach provides standardized data for comprehensive earthquake catalogs which are fundamental for other kinds of research such as earthquake statistics and seismic hazard assessment. But we need to be aware that these simplified, often purely empirical parameters can not give a full description of the true nature and geometry, the time history nor the energy release of a seismic source. In the following we will describe only the most common procedures that can be used in routine seismological practice.

3.2 Magnitude of seismic events (P. Bormann)

3.2.1 History, scope and limitations of the magnitude concept

The concept of magnitude was introduced by Richter (1935) to provide an objective instrumental measure of the size of earthquakes. In contrast to seismic intensity I , which is based on the assessment and classification of shaking damage and human perceptions of shaking and thus depends on the distance from the source, the magnitude M uses instrumental measurements of the ground motion adjusted for epicentral distance and source depth. Standardized instrument characteristics were originally used to avoid instrumental effects on the magnitude estimates. Thus it was hoped that M could provide a single number to measure earthquake size which is related to the released seismic energy, E_S. However, as outlined in 3.1 above, such a simple empirical parameter is not directly related to any physical parameter of the source. Rather, the magnitude scale aims at providing a quickly determined simple " ... parameter which can be used for first-cut reconnaissance analysis of earthquake data (catalog) for various geophysical and engineering investigations; special precaution should be exercised in using the magnitude beyond the reconnaissance purpose" (Kanamori, 1983).

In the following we will use mainly the magnitude symbols, sometimes with slight modification, as they have historically developed and are still predominantly applied in common practice. However, as will be shown later, these “generic” magnitude symbols are often not explicit enough as to recognize on what type of records, components and phases these magnitudes are based. This requires more “specific” magnitude names where higher precision is required (see IS 3.2).

The original Richter magnitude, ML or M_L, was based on maximum amplitudes measured in displacement-proportional records from the standardized short-period Wood-Anderson (WA) seismometer network in Southern California, which was suitable for the classification of local shocks in that region. In the following we will name it Ml (with “l” for “local”) in order to avoid confusion with more specific names for magnitudes from surface waves where the phase symbol L stands for unspecified long-period surface waves. Gutenberg and Richter (1936) and Gutenberg (1945a, b and c) then extended the magnitude concept so as to be applicable to ground motion measurements from medium- and long-period seismographic recordings of both surface waves (Ms or M_s) and different types of body waves (mB or m_B) in the teleseismic distance range. For the magnitude to be a better estimate of the seismic energy, they proposed to divide the measured displacement amplitudes by the associated periods to obtain ground velocities. Although they tried to scale the different magnitude scales together in order to match at certain magnitude values, it was realized that these scales are only imperfectly consistent with each other. Therefore, Gutenberg and Richter (1956a and b) provided correlation relations between various magnitude scales (see 3.2.7).

After the deployment of the World Wide Standardized Seismograph Network (WWSSN) in the 1960s it became customary to determine mB on the basis of short-period narrow-band P-wave recordings only. This short-period body-wave magnitude is called mb (or m_b). The introduction of mb increased the inconsistency between the magnitude estimates from body and surface waves. The main reasons for this are:

- different magnitude scales use different periods and wave types which carry different information about the complex source process;

- the spectral amplitudes radiated from a seismic source increase linearly with its seismic moment for frequencies $f < f_c$ (f_c – corner frequency). This increase with moment, however, is reduced or completely saturated (zero) for $f > f_c$ (see Fig. 3.5). This changes the balance between high- and low-frequency content in the radiated source spectra as a function of event size;
- the maximum seismic energy is released around the corner frequency of the displacement spectrum because this relates to the maximum of the ground-velocity spectrum (see Fig. 3.5). Accordingly, M, which is supposed to be a measure of seismic energy released, strongly depends on the position of the corner frequency in the source spectrum with respect to the pass-band of the seismometer used for the magnitude determination;
- for a given level of long-period displacement amplitude, the corner frequency is controlled by the stress drop in the source. High stress drop results in the excitation of more high frequencies. Accordingly, seismic events with the same long-period magnitude estimates may have significantly different corner frequencies and thus ratios between short-period/long-period energy or mb/Ms, respectively;
- seismographs with different transfer functions sample the ground motion in different frequency bands with different bandwidth. Therefore, no general agreement of the magnitudes determined on the basis of their records can be expected;
- additionally, band-pass recordings distort the recording amplitudes of transient seismic signals, the more so the narrower the bandwidth is. This can not be fully compensated by correcting only the frequency-dependent magnification of different seismographs based on their amplitude-frequency response. Although this is generally done in seismological practice in order to determine so-called "true ground motion" amplitudes for magnitude calculation, it is not fully correct. The reason is that the instrument magnification or amplitude-frequency response curves are valid only for steady-state oscillation conditions, i.e., after the decay of the seismograph's transient response to an input signal (see 4.2). True ground motion amplitudes can be determined only by taking into account the complex transfer function of the seismograph (see Chapter 5) and, in the case of short transient signals, by signal restitution in a very wide frequency band (Seidl, 1980; Seidl and Stammler, 1984; Seidl and Hellweg, 1988). Only recently a calibration function for very broadband P-wave recordings has been published (Nolet et al., 1998), however it has not yet been widely applied, tested and approved.

Efforts to unify or homogenize the results obtained by different methods of magnitude determination into a common measure of earthquake size or energy have generally been unsuccessful (e.g., Gutenberg and Richter, 1956a; Christoskov et al., 1985). Others, aware of the above mentioned reasons for systematic differences, have used these differences for better understanding the specifics of various seismic sources, e.g., for discriminating between tectonic earthquakes and underground nuclear explosions on the basis of the ratio mb/Ms. Duda and Kaiser (1989) recommend the determination of different spectral magnitudes, based on measurements of the spectral amplitudes from one-octave bandpass- filtered digital broadband velocity records.

Another effort to provide a single measure of the earthquake size was made by Kanamori (1977). He developed the seismic moment magnitude Mw. It is tied to Ms but does not saturate for big events because it is based on seismic moment M_0, which is made from the measurement of the (constant) level of low-frequency spectral displacement amplitudes for $f << f_c$. This level increases linearly with M_0. According to Eq. (3.1), M_0 is proportional to the

average static displacement and the area of the fault rupture and is so a good measure of the total deformation in the source region. On the other hand it is (see the above discussion on corner frequency and high-frequency content) neither a good measure of earthquake size in terms of seismic energy release nor a good measure of specifying seismic hazard since most earthquake damage is usually related to medium and low-rise structures with eigenfrequencies f > 0.5 Hz (i.e., lower than about 20 stories) and mainly caused by high-frequency strong ground motion. Consequently, there is no single number parameter available which could serve as a good estimate of earthquake "size" in all its different aspects. What is needed in practice are at least two parameters to characterize roughly both the size and related hazard of a seismic event, namely M_0 and f_c or Mw together with mb or Ml (based on short-period measurements), respectively, or a comparison between the moment magnitude Mw and the energy magnitude Me. The latter can today be determined from direct energy calculations based on the integration of digitally recorded waveforms of broadband velocity (Seidl and Berckhemer, 1982; Berckhemer and Lindenfeld, 1986; Boatwright and Choy 1986; Kanamori et al. 1993; Choy and Boatwright 1995) (see 3.3).

Despite their limitations, standard magnitude estimates have proved to be suitable also for getting, via empirical relationships, quick but rough estimates of other seismic source parameters such as the seismic moment M_0, stress drop, amount of radiated seismic energy E_S, length L, radius r or area A of the fault rupture, as well as the intensity of ground shaking, I_0, in the epicentral area and the probable extent of the area of felt shaking (see 3.6).

Magnitudes are also crucial for the quantitative classification and statistical treatment of seismic events aimed at assessing seismic activity and hazard, studying variations of seismic energy release in space and time, etc. Accordingly, they are also relevant in earthquake prediction research. All these studies have to be based on well-defined and stable long-term data. Therefore, magnitude values – notwithstanding the inherent systematic biases as discussed above - have to be determined over decades and even centuries by applying rigorously clear and well documented stable procedures and well calibrated instruments. Any changes in instrumentation, gain and filter characteristics have to be precisely documented in station log-books or event catalogs and data corrected accordingly. Otherwise, serious mistakes may result from research based on incompatible data.

Being aware now on the one hand of the inherent problems and limitations of the magnitude concept in general and specific magnitude estimates in particular and of the urgent need to strictly observe reproducible long-term standardized procedures of magnitude determination on the other hand we will review below the magnitude scales most commonly used in seismological practice. An older comprehensive review of the complex magnitude issue was given by Båth (1981), a more recent one by Duda (1989). Various special volumes with selected papers from symposia and workshops on the magnitude problem appeared in Tectonophysics (Vol. 93, No.3/4 (1983); Vol. 166, No. 1-3 (1989); Vol. 217, No. 3/4 (1993).

3.2.2. General assumptions and definition of magnitude

Magnitude scales are based on a few simple assumptions, e.g.:

- for a given source-receiver geometry "larger" events will produce wave arrivals of larger amplitudes at the seismic station. The logarithm of ground motion amplitudes A is used because of the enormous variability of earthquake displacements;

- magnitudes should be a measure of seismic energy released and thus be proportional to the velocity of ground motion, i.e., to A/T with T as the period of the considered wave;
- the decay of ground displacement amplitudes A with epicentral distance Δ and their dependence on source depth, h, i.e., the effects of geometric spreading and attenuation of the considered seismic waves is known at least empirically in a statistical sense. It can be compensated for by a calibration function $\sigma(\Delta, h)$. The latter is the log of the inverse of the reference amplitude $A_0(\Delta, h)$ of an event of zero magnitude, i.e., $\sigma(\Delta, h) = -\log A_0(\Delta, h)$;
- the maximum value $(A/T)_{max}$ in a wave group for which $\sigma(\Delta, h)$ is known should provide the best and most stable estimate of the event magnitude;
- regionally variable preferred source directivity may be corrected by a regional source correction term, C_r , and the influence of local site effects on amplitudes (which depend on local crustal structure, near-surface rock type, soft soil cover and/or topography) may be accounted for by a station correction, C_S, which is not dependent on azimuth.

Accordingly, the general form of all magnitude scales based on measurements of ground *displacement amplitudes* A_d and periods T is:

$$M = \log(A_d/T)_{max} + \sigma(\Delta, h) + C_r + C_S. \qquad (3.3)$$

Note: Calibration functions used in common practice do not consider a frequency dependence of σ. This is a serious omission. Theoretical calculations by Duda and Janovskaya (1993) show that, e.g., the differences in $\sigma(\Delta, T)$ for P waves may become > 0.6 magnitude units for T < 1 s, however they are < 0.3 for T > 4 s and thus they are more or less negligible for magnitude determinations in the medium- and long-period range (see Fig. 3.15).

3.2.3 General rules and procedures for magnitude determination

Magnitudes can be determined on the basis of Eq. (1) by reading $(A/T)_{max}$ for any body wave (e.g., P, S, Sg, PP) or surface waves (LQ or Lg, LR or Rg) for which calibration functions for either vertical (V) and/or horizontal (H) component records are available. If the period being measured is from a seismogram recorded by an instrument whose response is already proportional to velocity, then $(A_d/T)_{max} = A_{vmax}/2\pi$, i.e., the measurement can be directly determined from the maximum trace amplitude of this wave or wave group with only a correction for the velocity magnification. In contrast, with displacement records one may not know with certainty where $(A/T)_{max}$ is largest in the displacement waveform. Sometimes smaller amplitudes associated with smaller periods may yield larger $(A/T)_{max}$. In the following we will always use A for A_d, if not otherwise explicitely specified.

In measuring A and T from seismograms for magnitude determinations and reporting them to national or international data centers, the following definitions and respective instructions given in the Manual of Seismological Observatory Practice (Willmore, 1979) as well as in the recommendations by the IASPEI Commission on Practice from its Canberra meeting in 1979 (slightly modified and amended below) should be observed:

- the trace amplitude B of a seismic signal on a record is defined as its largest peak (or trough) deflection from the base-line of the record trace;

- for many phases, surface waves in particular, the recorded oscillations are more or less symmetrical about the zero line. B should then be measured either by direct measurement from the base-line or - preferably - by halving the peak-to-trough deflection (Figs. 3.9 a and c - e). For phases that are strongly asymmetrical (or clipped on one side) B should be measured as the maximum deflection from the base-line (Fig. 3.9 b);
- the corresponding period T is measured in seconds between those two neighboring peaks (or troughs) - or from (doubled!) trace crossings of the base-line - where the amplitude has been measured (Fig. 3.9);
- the trace amplitudes B measured on the record should be converted to ground displacement amplitudes A in nanometers (nm) or some other stated SI unit, using the A-T response (magnification) curve Mag(T) of the given seismograph (see Fig.3.11); i.e., A = B /Mag(T). (Note: In most computer programs for the analysis of digital seismograms, the measurement of period and amplitude is done automatically after marking the position on the record where A and T should be determined);
- amplitude and period measurements from the vertical component (Z = V) are most important. If horizontal components (N - north-south; E - east-west) are available, readings from both records should be made at the same time (and noted or reported separately) so that the amplitudes can be combined vectorially, i.e., $A_H = \sqrt{(A_N^2 + A_E^2)}$;
- when several instruments of different frequency response are available (or in the case of the analysis of digital broadband records filtered with different standard responses), A_{max} and T measurements from each should be reported separately and the type of instrument used should be stated clearly (short-, medium- or long-period, broadband, Wood-Anderson, etc., or related abbreviations given for instrument classes with standardized response characteristics; see Fig. 3.11 and Tab. 3.1). For this, the classification given in the old Manual of Seismological Observatory Practice (Willmore 1979) may be used;
- broadband instruments are preferred for all measurements of amplitude and period;
- note that earthquakes are often complex multiple ruptures. Accordingly, the time, t_{max} , at which a given seismic body wave phase has its maximum amplitude may be quite some time after its first onset. Accordingly, in the case of P and S waves the measurement should normally be taken within the first 25 s and 40-60 s, respectively, but in the case of very large earthquakes this interval may need to be extended to more than a minute. For subsequent earthquake studies it is also essential to report the time t_{max} (see Fig. 3.9).
- for teleseismic ($\Delta > 20°$) surface waves the procedures are basically the same as for body waves. However, $(A/T)_{max}$ in the Airy phase of the dispersed surface wave train occurs much later and should normally be measured in the period range between 16 and 24 s although both shorter and longer periods may be associated with the maximum surface wave amplitudes (see 2.3).
- note that in displacement proportional records $(A/T)_{max}$ may not coincide in time with $B_{max.}$ Sometimes, in dispersed surface wave records in particular, smaller amplitudes associated with significantly smaller periods may yield larger $(A/T)_{max}$. In such cases also A_{max} should be reported separately. In order to find $(A/T)_{max}$ on horizontal component records it might be necessary to calculate A/T for several amplitudes on both record components and select the largest vectorially combined value. In records proportional to ground velocity, the maximum trace amplitude is always related to $(A/T)_{max}$. Note, however, that as compared to the displacement amplitude A_d the velocity amplitude is $A_v = A_d\, 2\pi/T$.
- if mantle surface waves are observed, especially for large earthquakes (see 2.3), amplitudes and periods of the vertical and horizontal components with the periods in the neighborhood of 200 s should also be measured;

- on some types of short-period instruments (in particular analog) with insufficient resolutions it is not possible to measure the period of seismic waves recorded from nearby local events and thus to convert trace deflections properly to ground motion. In such cases magnitude scales should be used which depend on measurements of maximum trace amplitudes only;
- often local earthquakes will be clipped in (mostly analog) records of high-gain short-period seismographs with insufficient dynamic range. This makes amplitude readings impossible. In this case magnitude scales based on record duration (see 3.2.4.3) might be used instead, provided that they have been properly scaled with magnitudes based on amplitude measurements.

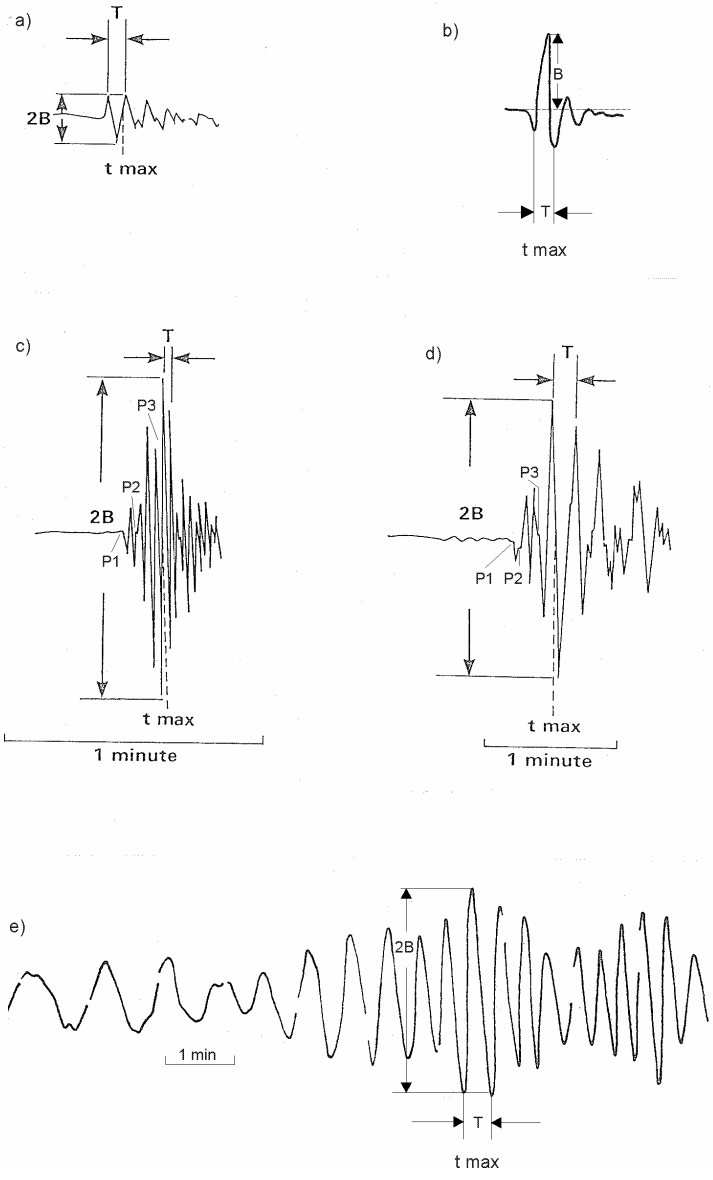

Fig. 3.9 Examples for measurements of trace amplitudes B and periods T in seismic records for magnitude determination: a) the case of a short wavelet with symmetric and b) with asymmetric deflections, c) and d) the case of a more complex P-wave group of longer duration (multiple rupture process) and e) the case of a dispersed surface wave train. Note: c) and d) are P-wave sections of the same event but recorded with different seismographs (classes A4 and C) while e) was recorded by a seismograph of class B3 (see Fig. 3.11).

Tab. 3.1 Example from the former bulletin of station Moxa (MOX), Germany, based on the analysis of analog photographic recordings. The event occurred on January 1967. Note the clear annotation of the type of instruments used for the determination of onset times, amplitudes and periods. Multiple body wave onsets of distinctly different amplitudes, which are indicative of a multiple rupture process, have been separated. Seismographs of type A, B and C were nearly identical with the response characteristics A4, B3 and C in Fig. 3.11. V = Z - vertical component; H - vectorially combined horizontal components; Lm - maximum of the long-period surface wave train.

Day	Phase	Seismograph	h m s	Remarks
5.	+eiP1	A	00 24 15.5	Mongolia 48.08°N 102.80°E
	iP2	A	24 21.5	H = 00 14 40.4 h = normal MAG = 6.4
	iP3	A,C	24 28.0	Δ = 55.7° Az = 309.6° (USCGS)
	Pmax	C	24 31	
	ePP2	C	26 27.5	PV1 A 1.2s 71.8nm MPV1(A)=5.6
	ePP3	C	26 34	PV2 A 1.8s 1120nm MPV2(A)=6.6
	eS2	C	32 04	PV3 A 1.6s 1575nm MPV3(A)=6.8
	i S3	C	32 11	PV3 C 8s 16.3µm MPV3(B)=7.1
	eiSS	B	35 56	SH3 C 18s 60µm MSH3(B)=7.3
	iSSS	B	36 44	LmV C 17s 610µm MLV(B) =7.8
	LmH	C	48.0	Note: P has a period of about 23s in the long-period seismograph of type B!

Note in Tab. 3.1 the distinct differences between individual magnitude determinations and the clear underestimation of short-period (type A) magnitudes. This early practice of specifying magnitude annotation has been officially recommended by the IASPEI Sub-Committee on Magnitudes in 1977 (see Willmore, 1979) but is not yet standard. However, current deliberations in IASPEI stress again the need for more specific magnitude measurements and reports to databases along these lines (see IS 3.2). When determining magnitudes according to more modern and physically based concepts such as radiated energy or seismic moment, special procedures have to be applied (see 3.3 and 3.5).

Global or regional data analysis centers calculate mean magnitudes on the basis of many A/T or M data reported by seismic stations from different distances and azimuths with respect to the source. This will more or less average out the influence of regional source and local station conditions. Therefore, A/T or M data reported by individual stations to such centers should not yet be corrected for C_r and C_S. These corrections can be determined best by network centers themselves when comparing the uncorrected data from many stations (e.g., Hutton and Boore, 1987). They may then use such corrections for reducing the scatter of individual readings and thus improve the average estimate.

When determining new calibration functions for the local magnitude Ml, station corrections have to be applied before the final data fit in order to reduce the influence of systematic biases on the data scatter. According to the procedure proposed by Richter (1958) these station corrections for Ml are sometimes determined independently for readings in the N-S and E-W components (e.g., Hutton and Boore, 1987). When calculating network magnitudes some centers prefer the median value of individual station reports of Ml as the best network estimate. As compared to the arithmetic mean it minimizes the influence of widely diverging individual station estimates due to outliers or wrong readings (Hutton and Jones, 1993).

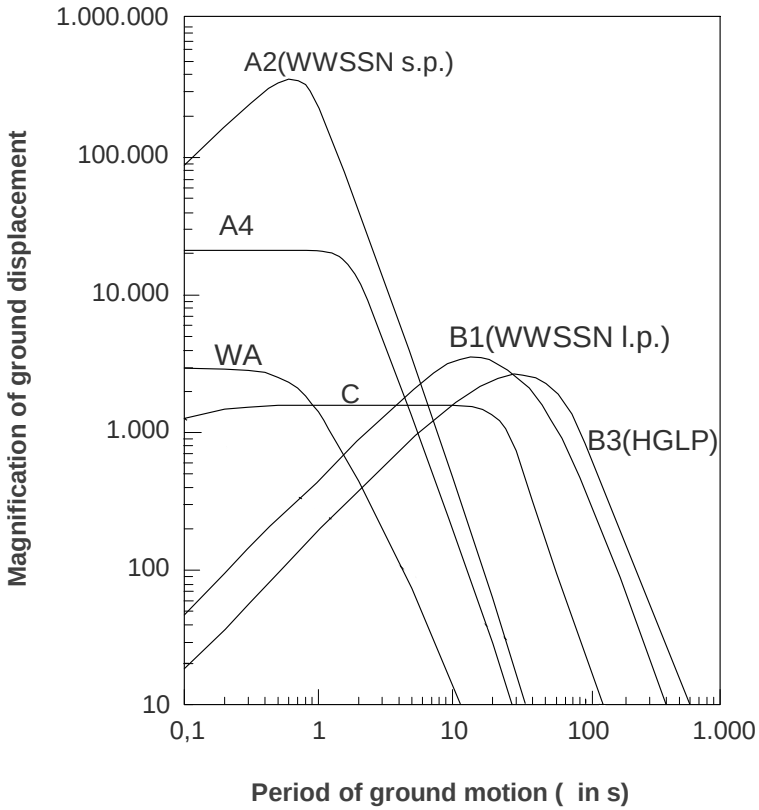

Fig. 3.11 Relative magnification curves for ground displacement for various classes of standardized analog recordings (partially redrawn from the old Manual of Seismological Observatory Practice, Willmore 1979 and amended). A4 and C are the magnification curves of the standard short-period and displacement broadband (Kirnos SKD) seismographs of the basic network of seismological stations in the former Soviet Union and Eastern European states while A2 and B1 are the standard characteristics for short- and long-period recordings at stations of the World Wide Standardized Seismograph Network (WWSSN) which was set up by the United States Geological Survey (USGS) in the 1960s and 1970s. The other magnification curves are: WA - Wood-Anderson torsion seismometer (see below), which was instrumental in the definition of the magnitude scale; HGLP - High Gain Long Period system.

In the following we will outline the origin, general features, formulae and specific differences of various magnitude scales currently in use. We will highlight which of these scales are at present accepted as world-wide standards and will also spell out related problems which still require consideration, clarifying discussion, recommendations or decisions by the IASPEI Commission on Seismological Observation and Interpretation. Data tables and diagrams on calibration functions used in actual magnitude determinations are given in Datasheet 3.1.

3.2.4 Magnitude scales for local events

The large variability of velocity and attenuation structure of the crust does in fact not permit the development of a unique, internationally standardized calibration function for local events. However, the original definition of magnitude by Richter (1935) did lead to the development of the local magnitude scale Ml (originally ML) for California. Ml scales for

other areas are usually scaled to Richter's definition and also the procedure of measurement is more or less standardized.

3.2.4.1 The original Richter magnitude scale Ml

Following a recommendation by Wadati, Richter (1935) plotted the logarithm of maximum trace amplitudes, A_{max}, measured from standard Wood-Anderson (WA) horizontal component torsion seismometer records as a function of epicentral distance Δ. The **WA seismometers** had the following parameters: natural period T_S = 0.8 s, damping factor D_S = 0.8, maximum **magnification V_{max} = 2800**. Richter found that log A_{max} decreased with distance along more or less parallel curves for earthquakes of different size. This led him to propose the following definition for the magnitude as a quantitative measure of earthquake size (Richter 1935, p. 7): *" The magnitude of any shock is taken as the logarithm of the maximum trace amplitude, expressed in microns, with which the standard short-period torsion seismometer ... would register that shock at an epicentral distance of 100 km".*

Note 1: Uhrhammer and Collins (1990) found out that the magnification of 2800 of WA seismometers had been calculated on the basis of wrong assumptions on the suspension geometry. **A more correct value** (also in Fig. 3.11) **is 2080 ± 60** (see also Uhrhammer et al., 1996). Accordingly, magnitude estimates based on synthesized WA records or amplification corrected amplitude readings assuming a WA magnification of 2800 systematically underestimate the size of the event by 0.13 magnitude units!

This local magnitude was later given the symbol ML (Gutenberg and Richter, 1956b). In the following we use Ml (l = local). In order to calculate Ml also for other epicentral distances, Δ, between 30 and 600 km, Richter (1935) provided attenuation corrections. They were later complemented by attenuation corrections for Δ < 30 km assuming a focal depth h of 18 km (Gutenberg and Richter, 1942; Hutton and Boore, 1987). Accordingly, one gets

$$Ml = \log A_{max} - \log A_0 \qquad (3.4)$$

with A_{max} in mm of measured zero-to-peak trace amplitude in a Wood-Anderson seismogram. The respective corrections or calibration values $-\log A_0$ were published in tabulated form by Richter (1958) (see Table 1 in DS 3.1).

Note 2: In contrast to the general magnitude formula (3.3), Eq. (3.4) considers only the maximum displacement amplitudes but not their periods. Reason: WA instruments are short-period and their traditional analog recorders had a limited paper speed. Proper reading of the period of high-frequency waves from local events was rather difficult. It was assumed, therefore, that the maximum amplitude phase (which in the case of local events generally corresponds to Sg, Lg or Rg) always had roughly the same dominant period. Also, $-\log A_0$ does not consider the above discussed depth dependence of $\sigma(\Delta, h)$ since seismicity in southern California was believed to be always shallow (mostly less than 15 km). Eq. (3.4) also does not give regional or station correction terms since such correction terms were already taken into account when determining $-\log A_0$ for southern California.

Note 3: Richter's attenuation corrections are valid for southern California only. Their shape and level may be different in other regions of the world with different velocity and attenuation structure, crustal age and composition, heat-flow conditions and source depth. Accordingly, when determining Ml calibration functions for other regions, the amplitude attenuation law

has to be determined first and then this curve has to be scaled to the original definition of Ml at 100 km epicentral distance (or even better at closer distance; see problem 1 below). Examples for other regional Ml calibration functions are shown in Fig. 3.12).

Note 4: The smallest events recorded in local microearthquake studies have negative values of Ml while the largest Ml is about 7 , i.e., the Ml scale also suffers *saturation* (see Fig. 3.18). Despite these limitations, Ml estimates of earthquake size are relevant for earthquake engineers and risk assessment since they are closely related to earthquake damage. The main reason is that many structures have natural periods close to that of the WA seismometer (0.8s) or are within the range of its pass-band (about 0.1 - 1 s).

A review of the development and use of the Richter scale for determining earthquake source parameters is given by Boore (1989).

Problems:

1) According to Hutton and Boore (1987) the *distance corrections developed by Richter for local earthquakes (Δ < 30 km) are incorrect*. This leads to magnitude estimates from nearby stations that are smaller than those from more distant stations. Bakun and Joyner (1984) came to the same conclusion for weak events recorded in Central California at distances of less than 30 km.
2) In 3.2.3 it was said that, as a general rule, in the case of horizontal component recordings, A_{Hmax} is the maximum vector sum amplitude measured at t_{max} in both the N and E component. Deviating from this, Richter (1958) says: *"... In using ...both horizontal components it is correct to determine magnitude independently from each and to take the mean of the two determinations. This method is preferable to combining the components vectorially, for the maximum motion need not represent the same wave on the two seismograms, and it even may occur at different times*." In most investigations aimed at deriving local Ml scales $A_{Hmax} = (A_N + A_E)/2$ has been used instead to calculate ML although this is not fully identical with $Ml = (Ml_N + Ml_E)/2$ and might give differences in magnitude of up to about 0.1 units.
3) The Richter Ml from arithmetically averaged horizontal component amplitude readings will be smaller by at least 0.15 magnitude units as compared to Ml from A_{Hmax} vector sum! In the case of significantly different amplitudes A_{Nmax} and A_{Emax} this difference might reach even several tenths of magnitude units. However, the method of combining vectorially the N and E component amplitudes, as generally practiced in other procedures for magnitude determination from horizontal component recordings, is hardly used for Ml because of reasons of continuity in earthquake catalogs, even though it would be easy nowadays with digital data.

3.2.4.2 Other Ml scales based on amplitude measurements

The problem of vector summing of amplitudes in horizontal component records or of arithmetic averaging of independent Ml determinations in N and E components can be avoided by using A_{Vmax} from vertical component recordings instead, provided that the respective -log A_0 curves are properly scaled to the original definition of Richter for Δ = 100 km. Several new formulas for Ml determinations based on readings of A_{Vmax} have been proposed for other regions (see Tab. 2 in DS 3.1). They mostly use Lg waves, sometimes well beyond the distance of 600 km for which -log A_0 was defined by Richter (1958). Alsaker et

al. (1991) and Greenhalgh and Singh (1986) showed that A_{Zmax} is ≈ 1 to 1.2 times $A_{Hmax} = 0.5 (A_{Nmax} + A_{Emax})$ and thus yields practically the same magnitudes.

Since Richter's $\sigma(\Delta) = -\log A_0$ for southern California might not be correct for other regions, local calibration functions have been determined for other seismotectonic regions. Those for continental shield areas revealed significantly lower body-wave attenuation when compared with southern California. Despite scaling $-\log A_0(\Delta)$ for other regions to the value given by Richter for Δ = 100 km, deviations from Richter's calibration function may become larger than one magnitude unit at several 100 km distances. Fig. 3.12 shows examples of Ml scaling relations for other regions. Although cut in this figure for epicentral distances Δ > 600 km some of the curves shown are defined for much larger distances (see Table 2 in DS 3.1).

Problem:
Hutton and Boore (1987) proposed that local magnitude scales be defined in the future such that Ml = 3 correspond to 10 mm of motion on a Wood-Anderson instrument at 17 km hypocentral distance rather than 1 mm of motion at 100 km. While being consistent with the original definition of magnitude in southern California this definition will allow more meaningful comparison of earthquakes in regions having very different wave attenuation within the first 100 km. This proposal has already been taken into consideration when developing a local magnitude scale for Tanzania, East Africa (Langston et al., 1998) and should be considered by IASPEI for assuring standardized procedures in the further development of local and regional Ml scales.

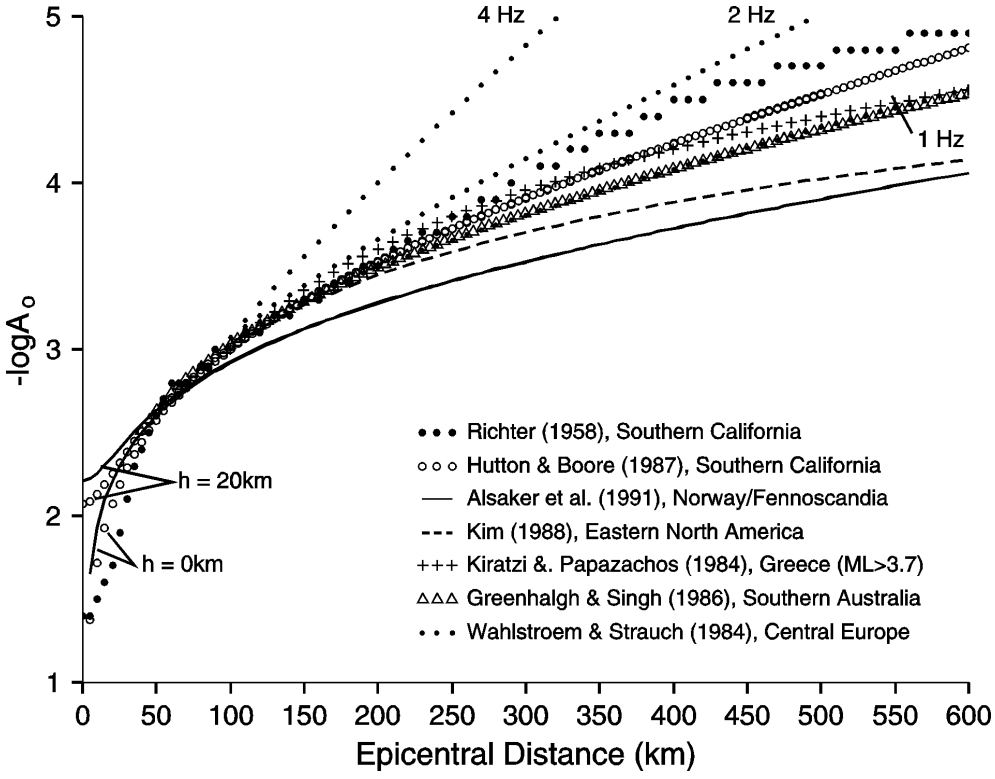

Fig. 3.12 Calibration functions for Ml determination for different regions. Note that the one for Central Europe is frequency dependent. The related Ml relationships and references are given in Table 2 of DS 3.1.

Some of the calibration functions shown in Fig. 3.12 for Lg waves extend in fact far beyond 600 km, e.g., that for Norway up to 1500 km distance. At this distance -log A_0 differs by 1.7 magnitude units from the extrapolated calibration curve for southern California!

Note 1: Station corrections in some of these studies varied between -0.6 to +0.3 magnitude units (Bakun and Joyner, 1984; Greenhalgh and Singh, 1986; Hutton and Jones, 1993) and correlated broadly with regional geology. This points to the urgent need to determine both calibration functions and station corrections for Ml on a regional basis.

Note 2: Since sources in other regions may be significantly deeper than in southern California, either $\sigma(\Delta, h)$ should be determined or at least the epicentral distance Δ should be replaced in the magnitude formulas by the "slant" or hypocentral distance $R = \sqrt{(\Delta^2 + h^2)}$. The latter is common practice now.

Procedures are currently available to synthesize precisely the response characteristic of Wood-Anderson seismographs from digital broadband recordings (e.g., Plešinger et al., 1996; see also 11.3.2). Therefore, WA seismographs are no longer required for carrying out Ml determinations. Savage and Anderson (1995) and Uhrhammer, et al. (1996) demonstrated the ability to determine an unbiased measure of local magnitude from synthetic WA seismograms. Thus, a seamless catalog of Ml could be maintained at Berkeley, California. In a first approximation (although not identical!) this can also be achieved by converting record amplitudes from another seismograph with a displacement frequency response $Mag(T_i)$ into respective WA trace amplitudes by multiplying them with the ratio $Mag_{WA}(T_i)/Mag(T_i)$ for the given period of A_{max}.

Sufficient time resolution of today's high-frequency digital records is likewise no longer a problem. There have been efforts to develop frequency-dependent calibration functions matched to the Richter scale at 100 km distance (e.g., Wahlström and Strauch, 1984; see Fig. 3.12) but this again breaks with the required continuity of procedures and complicates the calibration relationship for Ml.

The increasing availability of strong-motion records and their advantage of not being clipped even by very strong nearby events have led to the development of (partially) frequency-dependent Ml^{SM} scales for strong-motion data (Lee et al., 1990; Hatzidimitriou et al., 1993). The technique to calculate synthetic Wood-Anderson seismograph output from strong-motion accelerograms was first introduced by Kanamori and Jennings (1978).

3.2.4.3 Duration magnitude Md

Analog paper or film recordings have a very limited dynamic range of only about 40 dB and analog tape recordings of about 60 dB. For many years widely used digital recorders with 12 or 16 bit A-D converters enabled amplitude recordings with about 66 or 90 dB, respectively. Nevertheless, even these records were often clipped for strong local seismic events. This made magnitude determinations based on measurements of A_{max} impossible. Therefore, alternative magnitude scales such as Md were developed. They are based on the signal duration of an event. Nowadays with 24 bit A-D converters and ≈140 dB usable dynamic range, clipping is no longer a pressing problem. It is rare that an event is not considered for analysis.

In the case of local seismic events the total signal duration, d, is primarily controlled by the length of the coda which follows the Sg onset. A theoretical description of the coda envelopes as an exponentially decaying function with time was presented by Herrmann (1975). He proposed a duration magnitude formula of the general form:

$$Md = a_0 + a_1 \log d + a_2 \Delta \qquad (3.5)$$

Different procedures have been proposed for determining signal or coda duration such as:

- duration from the P-wave onset to the end of the coda, i.e., where the signal disappears in the seismic noise of equal frequency;
- duration from the P-wave onset to that time when the coda amplitudes have decayed to a certain threshold level, given in terms of average signal-to-noise ratio or of absolute signal amplitudes or signal level;
- total elapsed time = coda threshold time minus origin time of the event.

An early formula for the determination of local magnitudes based on signal duration was developed for earthquakes in Kii Peninsula in Central Japan by Tsumura (1967) and scaled to the magnitudes M_{JMA} reported by the Japanese Meteorological Agency:

$$Md = 2.85 \log (F - P) + 0.0014 \Delta - 2.53 \qquad \text{for } 3 < M_{JMA} < 5 \qquad (3.6)$$

with P as the onset time of the P wave and F as the end of the event record (i.e., where the signal has dropped down to be just above the noise level), F – P in s and Δ in km.

Another duration magnitude equation of the same structure has been defined by Lee et al. (1972) for the Northern California Seismic Network (NCSN). The event duration, d (in s), is measured from the onset of the P wave to the point on the seismogram where the coda amplitude has diminished to 1 cm on the Develocorder film viewer screen with its 20 times magnification. With Δ in km these authors give:

$$Md = 2.00 \log d + 0.0035 \Delta - 0.87 \qquad \text{for } 0.5 < Ml < 5. \qquad (3.7)$$

The location program HYPO71 (Lee and Lahr, 1975) employs Eq. (3.7) to compute duration magnitudes, called FMAG. But it was found that Eq. (3.7) yields seriously underestimated magnitudes of events Ml > 3.5. Therefore, several new duration magnitude formulae have been developed for the NCSN, all scaled to Ml. One of the latest versions by Eaton (1992) uses short-period vertical-component records, a normalization of instrument sensitivity, different distant correction terms for $\Delta < 40$ km, $40 \text{ km} \le \Delta \le 350$ km and $\Delta > 350$ km, as well as a depth correction for $h > 10$ km.

According to Aki and Chouet (1975) coda waves from local earthquakes are commonly interpreted as back-scattered waves from numerous heterogeneities uniformly distributed in the crust. Therefore, for a given local earthquake at epicentral distances shorter than 100 km the total duration of a seismogram is therefore almost independent of distance and azimuth and of structural details of the direct wave path from source to station. Also the shape of coda envelopes, which decay exponentially with time, remains practically unchanged. The dominating factor controlling the amplitude level of the coda envelope and signal duration is the earthquake size. This allows development of duration magnitude scales without a distance term, i.e.:

$$Md = a_0 + a_1 \log d \qquad (3.8)$$

Thus, quick magnitude estimates from local events are feasible even without knowing the exact distance of the stations to the source.

Note: Crustal structure, scattering and attenuation conditions vary from region to region. No general formulas can therefore be given. They must to be determined locally for any given station or network and be properly scaled to the best available amplitude-based Ml scale. In addition, the resulting specific equation will depend on the chosen definition for d, the local noise conditions and the sensor sensitivity at the considered seismic station(s) of a network.

3.2.5 Common teleseismic magnitude scales

Wave propagation in deeper parts of the Earth is more regular than in the crust and can be described sufficiently well by 1-D velocity and attenuation models. This permits derivation of globally applicable teleseismic magnitude scales. Fig. 3.13 shows smoothed A-Δ relationships for short-period P and PKP waves as well as for long-period surface waves for teleseismic distances, normalized to a magnitude of 4.

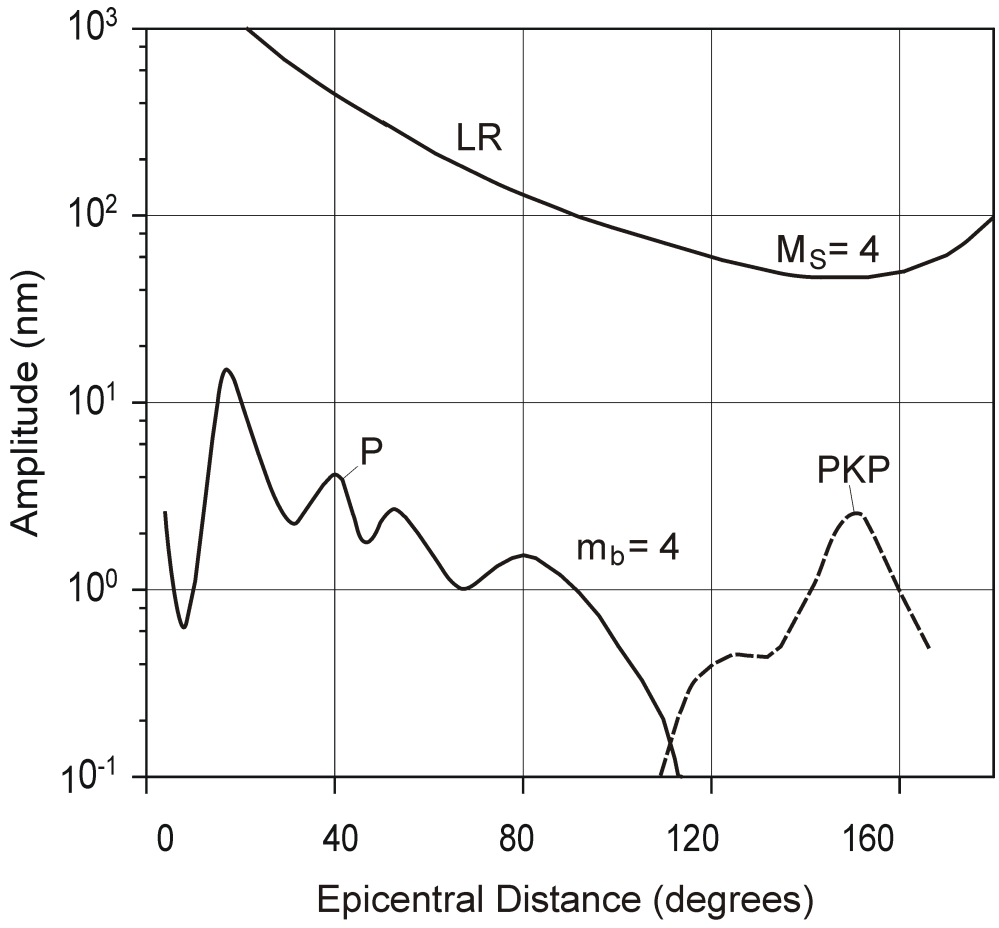

Fig. 3.13 Approximate smoothed amplitude-distance functions for P and PKP body waves (at about 1 Hz) and of long-period Rayleigh surface waves (LR, Airy phase, T ≈ 20 s) for an event of magnitude 4.

From Fig. 3.13 the following general conclusions can be drawn:

- surface waves and body waves have a different geometric spreading and attenuation. While the former propagate in two dimension only, the latter spread three-dimensionally. Accordingly, for shallow seismic events of the same magnitude, surface waves have generally larger amplitudes than body waves;
- surface wave amplitudes change smoothly with distance. They generally decay up to about 140° and increase again beyond about 150°-160°. The latter is due to the increased geometric focusing towards the antipode of the spherical Earth's surface which then overwhelms the amplitude decay due to attenuation;
- in contrast to surface waves, the A-Δ relations for first arriving longitudinal waves (P and PKP) show significant amplitude variations. The latter are mainly caused by energy focusing and defocusing due to velocity discontinuities in deeper parts of the Earth. Thus the amplitude peaks at around 20° and 40° are related to discontinuities in the upper mantle at 410 km and 670 km depth, the rapid decay of short-period P-wave amplitudes beyond 90° is due to the strong velocity decrease at the core-mantle boundary ("core shadow"), and the amplitude peak for PKP near 145° is caused by the focusing effect of the outer core (see Fig. 11.59).

Other body wave candidates for magnitude determinations again behave differently, e.g. PP which is reflected at the Earth's surface half way between the source and receiver. PP does not have a core shadow problem and is well observed up to antipode distances. Furthermore, one has to consider that body waves are generated efficiently by both shallow and deep earthquakes. This is not the case for surface waves. Accordingly, the different A-Δ-h behavior of surface and body waves requires different calibration functions if one wants to use them for magnitude determination.

3.2.5.1 Surface-wave magnitude scale Ms

Gutenberg (1945a) developed the magnitude scale Ms for teleseismic surface waves:

$$Ms = \log A_{Hmax}(\Delta) + \sigma_S(\Delta). \qquad (3.9)$$

It is based on measurements of the maximum horizontal "true" ground motion displacement amplitudes $A_{Hmax} = \sqrt{(A_N^2 + A_E^2)}$ of the surface wave train at periods $T = 20 \pm 2$ s. This maximum corresponds to the Airy phase, a local minimum in the group velocity dispersion curve of Rayleigh surface waves which arises from the existence of a low-velocity layer in the upper mantle (see 2.3). There was no corresponding formula given for using vertical component surface waves because no comparably sensitive and stable vertical component long-period seismographs were available at that time.

The calibration function $\sigma_S(\Delta)$ is the inverse of a semi-empirically determined A-Δ-relationship scaled to an event of Ms = 0, thus compensating for the decay of amplitude with distance. Richter (1958) gave tabulated values for $\sigma_S(\Delta)$ in the distance range $20° \le \Delta \le 180°$ (see Table 3 in DS 3.1).

This relationship was further developed by Eastern European scientists. Soloviev (1955) proposed the use of the maximum ground particle velocity $(A/T)_{max}$ instead of the maximum

ground displacement A_{max} since the former is more closely related to seismic energy. It also better accounts for the large variability of periods at the surface-wave amplitude maximum (Airy phase) depending on distance and crustal structure (see 2.3). For most continental Rayleigh waves the Airy phase periods are around 20 s and fall indeed within the narrow period window of 20 ± 2 s set by Gutenberg. However, periods as small as 7 s have been observed at 10° and of 16 s at 100° epicentral distances while the largest periods observed for continental paths may reach 28 s and be still somewhat higher for oceanic paths.

Collaboration between research teams in Prague, Moscow and Sofia resulted in the proposal of a new Ms scale and calibration function, termed Moscow-Prague formula, by Karnik et al. (1962):

$$Ms = \log (A/T)_{max} + \sigma_S(\Delta) = \log (A/T)_{max} + 1.66 \log \Delta + 3.3 \qquad (3.10)$$

for epicentral distances $2° < \Delta < 160°$ and source depth $h < 50$ km. The IASPEI Committee on Magnitudes recommended at its Zürich meeting in 1967 the use of this formula as **standard for Ms determination for shallow seismic events ($h \leq 50$ km).**

Another scale, said to be well calibrated with the Gutenberg and Richter Ms scale, however based on records from 5-s instruments, is used by the Japan Meteorological Agency for regional events only (Tsuboi, 1954):

$$M(JMA) = \log \sqrt{(A_N^2 + A_E^2)} + 1.73 \log \Delta - 0.83$$

with Δ in km and A ground amplitudes in μm.

Note 1: For 20 s surface waves of the same amplitudes Eq. (3.10) yields, on average, magnitudes which are about 0.2 units larger than the original Gutenberg-Richter Ms according to (3.9) and tabulated in Table 3 of DS 3.1. This has been confirmed by Abe (1981). He gave the following relationship between Ms determinations by NEIC using Eq. (3.10) and Ms according to Gutenberg-Richter:

$$Ms(\text{“Prague”, NEIC}) = Ms(\text{Gutenberg-Richter}) + 0.18. \qquad (3.11)$$

Note 2: Eq. (3.10) is defined only up to 160°. It does not account for the amplitude increase beyond 160°. However, the latter is obvious in the tabulated version of $\sigma(\Delta)_H$ issued by the Moscow-Prague-Sofia group (see Table 4 in DS 3.1).

Note 3: As shown in Fig. 3.5, surface-wave spectra from events with Ms > 7 and a seismic moment $M_0 > 10^{20}$ Nm will have their corner period at T > 20 s. Consequently, Ms scales based on $(A/T)_{max}$ measurements for periods $T \approx 20$ s will systematically underestimate the size of larger events and saturate around Ms = 8.5 (see Fig. 3.18). Such was the case with the strongest earthquake of the 20th century in Chile 1960, which had a seismic moment $M_0 = 2\text{-}3 \times 10^{23}$ Nm for the main shock but an Ms of only 8.5 (see Lay and Wallace, 1995). Several efforts have therefore been made to develop a moment magnitude Mw (see 3.2.5.3) and other non-saturating magnitude scales (see 3.2.6.1 and 3.2.6.2).

Note 4: There may be significant regional biases due to surface-wave path effects. Lateral velocity variations in the crust and upper mantle as well as refraction at plate boundaries may result in significant focusing and de-focusing effects and related regional over- or underestimation of Ms (Lazareva and Yanovskaya, 1975). According to Abercrombie (1994)

this seems to be the main cause for the anomalous high surface-wave magnitudes of continental earthquakes relative to their seismic moments rather than differences in the source process. Therefore, in order to obtain reliable, unbiased estimates of regional seismic strain rate and hazard, local/regional moment-magnitude relationships should be preferred to global ones.

The 1979 edition of MSOP (Willmore 1979) recommends the use of the standard formula Eq. (3.10) for both horizontal and vertical components. Bormann and Wylegalla (1975) and Bormann and Khalturin (1975) used a large global data set of long-period surface-wave magnitudes MLH and MLV determined at station MOX, Germany to show that this is justified. They used $(A/T)_{max}$ surface-wave readings for the horizontal (H) and vertical (V) components of instruments of type C (see Fig. 3.11) in the magnitude range $3.7 < Ms < 8.2$ and adjusted them with the tabled calibration values (Table 4 in DS 3.1) corresponding to Eq. (3.10). They obtained the orthogonal regression relationship MLV - 0.97 MLH = 0.19 with a correlation coefficient 0.98 and a standard deviation of only ± 0.11.

The NEIC adopted the vertical component as its standard in May 1975 (Willmore 1979), i.e., Ms is determined from the Rayleigh-wave maximum only. Table 5 in DS 3.1 may aid in finding the appropriate part of the record.

Today, both the ISC and NEIC use Eq. (3.10) for the determination of Ms from events with focal depth $h < 60$ km without specifying the type of waves or components considered. The ISC accepts both vertical or resultant horizontal amplitudes of surface waves with periods between 10 - 60 s from stations in the distance range 5° - 160° but calculates the representative average Ms only from observations between 20° - 160°. In contrast, the NEIC calculates Ms only from vertical component readings of stations between $20° \leq \Delta \leq 160°$ and for reported periods of $18 \text{ s} \leq T \leq 22$ s. This limitation in period range is not necessary and limits the possibility of Ms determinations from regional earthquakes.

Very recently Yacoub (1998) presented a method for accurate estimation of Rayleigh-wave spectral magnitudes M_R by velocity and frequency window analysis of digital records. He applied it to records of underground nuclear explosions in the distance range 5° to 110°and compared M_R with the classical time-window magnitude estimates, Ms, according to Eq. (3.10). While both agreed well, in general M_R had smaller standard deviations. Another advantage is that the procedure for M_R determination can easily be implemented for on-line automated magnitude measurements. (Note: According to proposed specific magnitude names M_R should be termed MLR; see IS 3.2).

Problems:

1) Herak and Herak (1993) found that $\sigma_S(\Delta)$ in the Moscow-Prague formula does not yield consistent magnitude estimates independent of Δ. They proposed instead the formula:

$$Ms = \log (A/T)_{max} + 1.094 \log \Delta + 4.429. \qquad (3.12)$$

This formula is based on USGS data, i.e., on amplitude readings in the period range 18 to 22 s. It provides distance-independent estimates of Ms over the whole distance range $4° < \Delta < 180°$. Ms values according to Eq. (3.12) are equal to those from Eq. (3.10) at $\Delta = 100°$, larger by 0.39 magnitude units at $\Delta = 20°$ and smaller by 0.12 units for $\Delta = 160°$. Eq. (3.12) is practically equal to the magnitude formulae earlier proposed by von Seggern (1977) and similar to more recent results obtained by Rezapour and Pearce (1998).

2) The possible introduction of Eq. (3.12) as a new standard calibration function for Ms has not yet been discussed or recommended by the IASPEI Commission on Practice. The same applies to depth corrections for σ_S. Empirically derived corrections for intermediate and deep earthquakes were published by Båth (1985). They range between 0.1 and 0.5 magnitude units for focal depths of 50 - 100 km and between 0.5 and 0.7 units for depths of 100 - 700 km. But theoretical calculations by Panza et al. (1989) indicate that the depth correction may already exceed one magnitude unit even for shallow sources ($h \leq 60$ km). This is confirmed by an empirical formula used at seismic stations in Russia for determining the depth of shallow earthquakes ($h < 70$ km) from the ratio mB/Ms (Ochozimskaya, 1974): **h (in km) = 54 mB – 34 Ms – 107** (correlation coefficient 0.88).
3) Recently, there has been again a tendency to determine the surface-wave magnitude by specifying the type of the waves and/or components used, e.g., MLRH or MLRV from Rayleigh waves and MLQH from Love waves or simply MLH and MLV as was the practice in Eastern Germany in the 1960's (see Tab. 3.1) and recommended already in 1967 by the IASPEI Committee on Magnitude at Zürich. Since the newly proposed IASPEI Seismic Format (see 10.2.5) accepts such specifications in data reports to data centers, the IASPEI WG on Magnitude Measurements will elaborate recommendations for unambiguous standards and "specific" magnitude names (see IS 3.2).

3.2.5.2 Magnitude scales for teleseismic body waves

Gutenberg (1945b and c) developed a magnitude relationship for teleseismic body waves such as P, PP and S in the period range 0.5 s to 12 s. It is based on theoretical amplitude calculations corrected for geometric spreading and (only distance-dependent!) attenuation and then adjusted to empirical observations from shallow and deep-focus earthquakes, mostly in intermediate-period records:

$$mB = \log (A/T)_{max} + Q(\Delta, h). \qquad (3.13)$$

Gutenberg and Richter (1956a) published a table with $Q(\Delta)$ values for P-, PP- and S-wave observations in vertical (V=Z) and horizontal (H) components for shallow shocks (see Tab. 6 in DS 3.1), complemented by diagrams $Q(\Delta, h)$ for PV, PPV and SH (Figures. 1a-c in DS 3.1) which enable also magnitude determinations for intermediate and deep earthquakes. These calibration functions are correct when ground displacement amplitudes are measured in intermediate-period records and given in micrometers ($1\ \mu m = 10^{-6}$ m).

Gutenberg and Richter (1956a) also proposed a *unified magnitude m* as a weighted average of the individual mB values determined for these different types of body waves. Because of their different propagation paths they also differ in their frequency spectra. In addition, these body waves leave the source at different take-off angles and have different radiation pattern coefficients. Using these body waves jointly for the computation of magnitude significantly reduces the effect of the source mechanism on the magnitude estimate. Gutenberg and Richter (1956a) also scaled *m* (and thus, in a first approximation, also individual mB) to the earlier magnitude scales Ml and Ms so as to match these scales at magnitudes between about 6 to 7. Since mB is based on amplitude measurements at shorter periods than those observed in the Airy phase of surface waves, the mB scale saturates somewhat earlier than Ms (see Fig. 3.18).

Later, with the introduction of the WWSSN short-period 1s-seismometers (see Fig. 3.11, type A2) it became common practice at the NEIC to use the calibration function $Q(\Delta, h)$ for short-period PV only. In addition, it was recommended that the largest amplitude be taken within

the first few cycles (see Willmore, 1979) instead of measuring the maximum amplitude in the whole P-wave train. One should be aware that this practice was due to the focused interest on discriminating between earthquakes and underground nuclear explosions. The resulting short-period mb values strongly underestimated the body-wave magnitudes for mB > 5 (see Tab. 3.1) and, as a consequence, overestimated the annual frequency of small earthquakes in the magnitude range of kt-explosions. Also, mb saturated much earlier than the original Gutenberg-Richter mB for intermediate-period body waves or Ms for long-period surface waves (see Figs. 3.5 and 3.16). Therefore, the IASPEI Commission on Practice issued a revised recommendation in 1978 according to which the maximum P-wave amplitude for earthquakes of small to medium size should be measured within 20 s from the time of the first onset and for very large earthquakes even up to 60 s (see Willmore, 1979, p. 85). This somewhat reduced the discrepancy between mB and mb but in any event both are differently scaled to Ms and the short-period mb necessarily saturates earlier than medium-period mB (see Fig. 3.5). Interestingly, the effect of the source radiation pattern on the amplitudes used for mb determination is relatively small (Schweitzer and Kværna, 1999).

However, some of the national and international agencies have only much later or not even now changed their practice of measuring $(A/T)_{max}$ for mb determination in a very limited time-window, e.g., the International Data Centre for the monitoring of the CTBTO still uses a time window of only 6 s (5.5s after the P onset), regardless of the event size. In contrast with this and early practice at the NEIC of measuring A/T in P-wave records, the Soviet/Russian practice of analyzing short-period records was always to measure the true maximum on the entire record. These magnitudes were denoted as mPVA (or mSKM, using the abbreviation of the short-period Kirnos instrument type code) in order to differentiate them from mb of NEIC derived from short-period Benioff instruments. Nevertheless, for the latter, similar magnitudes were determined for large earthquakes when using (A/T)max in the whole P-wave train, e.g., by Koyama and Zeng (1985), denoted as m_b^*, and by Houston and Kanamori (1986), denoted $\hat{m}_b$.With respect to saturation, mSKM, m_b^* and $\hat{m}_b$ behave much like Ml, as could be expected from their common frequency band and considering that Ml is determined also from the maximum amplitude in the whole short-period record. Ml saturates around 7.5.

Problems:

1) Despite the strong recommendation of the Committee on Magnitudes at the IASPEI General Assembly in Zürich (1967) to report the magnitude for all waves for which calibration functions are available, both the ISC and NEIC continue to determine body-wave magnitudes only from vertical component short-period P wave readings of T ≤ 3 s. No body-wave magnitudes from PP or S waves are determined despite their merits discussed above and the fact that digital broadband records, which now allow easy identification and parameter determination of these later phases, are more and more widely available.
2) Both NEIC and ISC still use for short-period mb determination the Gutenberg and Richter (1956a) $Q(\Delta, h)_{PZ}$ functions although these were mainly derived from and used for intermediate-period data, as the Q-functions for PP and S too. However, in this context one has to consider that Gutenberg and Richter did not believe in the frequency-dependent attenuation model. The calibration curves were derived by assuming a linear model for attenuation proportional to exp-0.00006 L, where L is the total length of the ray path from the station to the source. This seems to make the $Q(\Delta, h)$ functions equally applicable to 10 s data and 10 Hz data, which is not the case. Duda and Yanovskaya (1993) showed that theoretical spectral logA-D curves, calculated on the basis of the PREM model (see Fig. 2.53), differed in the teleseismic distance range between 20° and

100° for periods of 1 s and 10 s, respectively, by about 0.3 to 0.6 and, when calculated for the ABM attenuation model, by even 0.9 to 1.4 magnitude units (see Fig. 3.15). Between 1 Hz and 10 Hz these differences are even larger. When neglecting the frequency-dependent attenuation, amplitude readings at higher frequency systematically underestimate the magnitude when scaled with $Q(\Delta, h)_{PV}$. For medium-period waves, however, e.g., for periods between 4 and 16 s, these differences become < 0.3 magnitude units, independent of the attenuation model. This is another strong argument in favor of using preferably medium-period or even better broadband data for the determination of teleseismic body-wave magnitudes, thus also reducing or avoiding the saturation effect.

3) None of the more recent studies (see 3.2.6) has received world-wide consideration and endorsement for routine use, and the major international agencies are therefore continuing to apply the tables of Gutenberg and Richter (1956a) as recommended in 1967 by the Committee on Magnitudes.
4) No proper discrimination has been made yet at the international data centers between data readings from different kinds of instruments or filters although respective recommendations have already been made at the joint IASPEI/IAVCEI General Assembly in Durham, 1977 (see below).
5) Observations less than 21° or more than 100° are also ignored although good PP readings are available far beyond 100° and calibration functions $Q(\Delta, h)$ exist for PPH and PPV up to 170°. As shown by Bormann and Khalturin (1975), mB for P and PP waves are perfectly scaled (orthogonal regression mB(PP) – mB(P) = 0.05 with a standard deviation of only ±0.15 magnitude units!). When using short-period amplitude readings for P and PP instead, the orthogonal relationship becomes magnitude-dependent (mb(PP) = 1.25 mb(P) -1.22) and the standard deviation is much larger (±0.26). This testifies the greater stability of body-wave magnitude determinations based on medium-period readings.
6) The suitability of PKP readings in the distance range of the core caustic around 145° and beyond has also been ignored so far (see 3.2.6.5).

Recommendations:

1) The IASPEI Commission on Seismological Observation and Interpretation with its WG on Magnitude Measurements must take the lead in recommending standards for magnitude-parameter readings. It should also propose a nomenclature that permits a more specific and unique reporting of measurements. For preliminary discussions along these lines see IS 3.2. They further develop earlier practices (as demonstrated with Tab. 3.1) and earlier recommendations at the joint General Assembly of the IASPEI/IAVCEI at Durham (1977). The latter are reproduced in the old MSOP (see Willmore, 1979, page 124) which is still accessible on the web site http://216.103.65.234/iaspei.html via the links “Supplementary Volumes on CDs”, “Literature in Seismology”, and then “MSOP”.

2) While these early recommendations for standard magnitude determinations were based on analog instrument classes as depicted in Fig. 3.11 and given in detail in Chapter INST 1.1 of the old MSOP, p. 41, broadband digital recordings are becoming more and more the standard. This requires to define the standard response characteristics required for standard magnitude determinations in terms of poles and zeros, with the range of tolerance for appropriate filters. These are required to synthesize these standard responses from original, usually velocity-proportional, digital broadband records (see 11.3.2).

3) More recently developed magnitude scales for short-period and broadband P-wave readings, PKP and mantle surface waves etc. (see 3.2.6) should be rigorously tested and, in the case of their suitability and known relationship to other commonly used scales, be recommended for standardized routine practice.

3.2.5.3 Moment magnitude Mw

According to Eq. (3.2) and Fig. 3.5 the scalar seismic moment $M_0 = \mu \bar{D} A$ is determined from the asymptote of the displacement amplitude spectrum as frequency $f \rightarrow 0$ Hz and it does not saturate. Kanamori (1977) proposed, therefore, a moment magnitude, Mw, which is tied to Ms but which would not saturate. He reasoned as follows: According to Kostrov (1974) the radiated seismic strain energy is proportional to the stress drop $\Delta\sigma$, namely $E_S \approx \Delta\sigma \bar{D} A/2$. With Eq. (3.2) one can write $E_S \approx (\Delta\sigma/2\mu) M_0$. (For definition and determination of M_0 and $\Delta\sigma$ see IS 3.1 and EX 3.4). Assuming a reasonable value for the shear modulus μ in the crust and upper mantle (about $3\text{-}6 \times 10^4$ MPa) and assuming that, according to Kanamori and Anderson (1975) and Abe (1975), the stress drop of large earthquakes is remarkably constant (ranging between about 2 and 6 MPa; see Fig. 3.39), one gets as an average $E_S \approx M_o/2x10^4$ (see Fig. 3.38). Inserting this into the relationship proposed by Gutenberg and Richter (1956c) between the released seismic strain energy E_S and Ms, namely

$$\log E_S = 4.8 + 1.5\ Ms \text{ (in SI units Joule J = Newton meter Nm)} \qquad (3.14)$$

it follows:

$$\log M_0 = 1.5\ Ms + 9.1. \qquad (3.15)$$

Solving (3.15) for the magnitude and replacing Ms with Mw one gets

$$Mw = 2/3\ (\log M_0 - 9.1). \qquad (3.16)$$

Note that Mw scales well with the logarithm of the rupture area (see Eq. (3.107)). The determination of M_0 on the basis of digital broadband records is becoming increasingly standard at modern observatories and network centers. This applies not only to very strong and teleseismic events but also to comparable scaling of moderate and weak events, both in the teleseismic and the local/regional range. The computed M_0, however, depends on details of the individual inversion methodologies and thus related Mw may differ. A simple, fast and robust method of Mw determination from broadband P waveforms has been developed by Tsuboi et al. (1995) for rapid evaluation of the tsunami potential of large earthquakes.

3.2.6 Complementary magnitude scales

Below we describe several other complementary procedures for magnitude estimation. They are not (yet) based on internationally recommended standards but are also useful for applications in seismological practice.

3.2.6.1 Mantle magnitude Mm

Okal and Talandier (1989;1990) describe in detail the further development and use of a "mantle magnitude" which was earlier introduced by Brune and Engen (1969). Based on

observations of very long-period mantle surface waves (see 2.3), Mm was first developed for Rayleigh waves and later extended to Love waves. Mm is a magnitude scale which is also firmly related to the seismic moment M_0 and thus avoids saturation. On the other hand, it is closer to the original philosophy of a magnitude scale by allowing quick, even one-station automated measurements (Hyvernaud et al., 1993), that do not require the knowledge of either the earthquake's focal geometry or its exact depth. The latter parameters would be crucial for refining a moment estimate and require (global) network recordings. Mm is defined as $Mm = \log X(\omega) + C_S + C_D - 0.90$ with $X(\omega)$ as the spectral amplitude of a Rayleigh wave in μm-s. C_S is a source correction, and C_D is a frequency-dependent distance correction. For details of the correction terms, see Okal and Talandier (1989 and 1990).

Applications of Mm to the reassessment of the moment of shallow, intermediate and deep historical earthquakes are extensively described by Okal (1992 a and b). Mm is an estimate of ($\log M_0$ - 13) (when M_0 is given in Nm). For the Chile 1960 earthquake Okal (1992a) calculated values Mm ≈ 10 to 10.3 and for $M_0 = 3.2 \cdot 10^{23}$ Nm. Mm determinations were extensively verified and are said to be accurate by about ± 0.2 magnitude units (Hyvernaud et al., 1993).

3.2.6.2 Energy magnitude Me

According to Kanamori (1977) Mw agrees very well with Ms for many earthquakes with a rupture length of about 100 km . Furthermore, he suggested that Eq. (3.14) also gives a correct value of the seismic-wave energy for earthquakes up to rupture dimensions ≤ about 100 km. Thus, he considered the Mw scale to be a natural continuation of the Ms scale for larger events. Inserting into the $\log E_S$-Ms relationship the value of Mw = 9.5 for the Chile 1960 earthquake instead of the saturated value Ms = 8.5 one gets a seismic energy release that is 30 times larger!

When substituting in Eq. (3.14) the surface-wave magnitude Ms by an energy magnitude Me, one gets

$$Me = 2/3 \, (\log E_S - 4.8) \qquad (3.17)$$

which reduces to $Me = 2/3 \, (\log M_0 - 9.1) = Mw$ (see Eq. (3.16)) if Kanamori´s condition $E_S/M_0 \approx 5 \cdot 10^{-5}$ holds. This result has been published earlier by Purcaru and Berckhemer (1978). But this is valid only for the average apparent stresses (and related stress drop) on which the Kanamori condition is based. As Choy and Boatwright (1995) showed, apparent stress, which is related to the ratio of E_S/M_0, may vary even for shallow events over a wide range between about 0.03 and 20.7 MPa. They found systematic variations in apparent stress as a function of focal mechanism, tectonic environment and seismic setting. Oceanic intraplate and ridge-ridge transform earthquakes with strike-slip mechanisms tend to have higher stress drops than interplate thrust earthquakes. Accordingly, Me for the former will often be significantly larger than Mw. The opposite will be true for the majority of thrust earthquakes: Mw will be larger than Me. Riznichenko (1992) gave a correlation on the basis of data from various authors. It predicts (despite rather large scatter) an average increase of $\Delta\sigma$ with source depth h according to $\Delta\sigma = 1.7 + 0.2$ h, i.e., stress drops ranging over 100 MPa can be expected for very deep earthquakes. On the other hand, Kikuchi and Fukao (1988) found from analyzing 35 large earthquakes in all depth ranges that $E_S/M_0 \approx 5 \cdot 10^{-6}$, i.e., a ratio that is one order of magnitude less than the condition used by Kanamori for deriving Mw. Therefore, Me is not uniquely determined by Mw. Me and Mw can be considerably different.

A striking example has been presented by G. Choy at the spring meeting 2002 of the American Geophysical Society (see Tab. 3.2 in 3.3.5). Nowadays, with digital broadband recordings and fast computer programs, it is feasible to determine directly the seismic energy, $E_{S,}$ by integrating the radiated energy flux in velocity-squared seismograms over the duration of the source process and correcting it for the effects of geometric spreading, attenuation and radiation pattern. A method developed by Boatwright and Choy (1986) is now routinely applied at NEIC to compute radiated energies for shallow earthquakes of mb > 5.8 (see 3.3) but its application is not so trivial and not for use with single stations. Using almost 400 events, Choy and Boatwright derived the relationship for E_S-Ms as

$$\log E_S = 1.5\ Ms + 4.4 \tag{3.18}$$

It indicates that (3.14) slightly overestimates E_S. On the basis of these direct energy estimates these authors developed the non-saturating energy magnitude (see also 3.3.3)

$$Me = 2/3\ (\log E_S - 4.4) \tag{3.19}$$

which yields for earthquakes satisfying Kanamori´s condition

$$Me = 2/3 \log M_0 - 5.80 = Mw + 0.27 \tag{3.20}$$

i.e., an Me that is somewhat larger than Mw and an Me derived from the Gutenberg-Richter Es/Ms relationship. Me may become significantly larger for high stress drop earthquakes and much smaller than Mw for slow or “tsunami” earthquakes. The latter may generate a strong (namely long-period) tsunami but only weak short-period ground motion, which may cause no shaking-damage and might not even be felt by people such as the September 2, 1992 Nicaragua mb 5.3 and Mw 7.6 earthquake (see also 3.2.6.9).

A strong argument to use Me instead of Mw is that it follows more closely the original intent of the Gutenberg-Richter formula by relating magnitude to the velocity power spectrum and, thus, to energy. In contrast, Mw is related to the seismic moment M_0 that is derived from the low-frequency asymptote of the displacement spectrum. Consequently, Me is more closely related to the seismic potential for damage while Mw is related to the final static displacement and the rupture area and thus related more to the tectonic consequences of an earthquake.

3.2.6.3 Broadband and spectral P-wave magnitude scales

A calibration function $Q_b(\Delta, h)$ based on broadband recordings of P waves (bandpass between 0.01 and 2 Hz) was derived recently by Nolet et al. (1998). It differs markedly from both $P(\Delta, h)_{SP}$ and $Q(\Delta, h)_{PZ}$.

Duda and Kaiser (1989) recommended instead the determination of spectral magnitudes based on measurements of spectral amplitudes from one-octave bandpass-filtered digital broadband records of P waves. As can be seen from Fig. 3.14, earthquakes of about the same magnitude mb and recorded within about the same distance range may have, depending also on focal depth and the type of rupture mechanism, very different amplitudes in different spectral ranges. This is due to regional differences in ambient stress conditions and related stress drop. Duda and Yanovskaya (1993) also calculated theoretical spectral amplitude-distance curves based on the IASP91 velocity model (Kennett and Engdahl, 1991) and two different

attenuation models so as to allow the magnitude calibration of spectral amplitude measurements (see Fig. 3.15). This effort is a response to the problems discussed above. It also yields smoothed averaged estimates of the radiated seismic spectrum, its spectral plateau, corner frequency and high-frequency decay and thus of M_0 and stress drop of the given event. Thus one may draw inferences on systematic differences in the prevailing source processes (e.g., low, normal or high stress drop) and related ambient stress conditions in different source regions. However, this is not so much the concern of seismological routine practice, which is aimed at providing a simple one (or two) parameter size-scaling of seismic events for general earthquake statistics and hazard assessment. Rather, this is more a research issue, which can be best tackled, along with proper quantification of earthquake size, by determining both Me and Mw or analyzing both M_0 and the shape of the overall source spectrum. On the other hand there is merit in determining the maximum spectral amplitude A_{vmax} of ground velocity directly from velocity broadband records by filtering them with constant bandwidth around the predominant period of the considered body-wave group and correcting it for the frequency-dependent attenuation. This should yield a saturation-free mB based on simple amplitude and period measurements at a single station, which comes closest to Me and thus to the original intention of Gutenberg for the teleseismic body-wave magnitude. Preconditions are that the period of A_{vmax} is within the passband of the velocity response and the frequency-dependent attenuation is sufficiently well known. Such an mB, given together with the period of A_{vmax}, allows to assess the frequency content where the maximum seismic energy has been released. This is of great importance for assessing the damage potential of a given event.

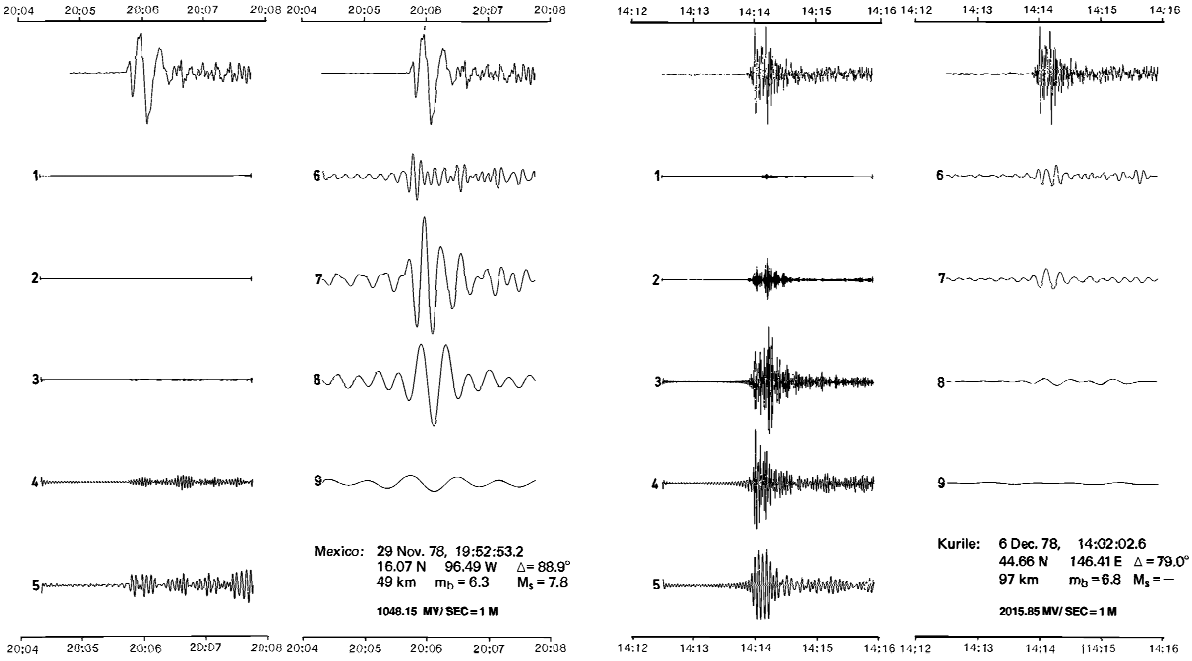

Fig. 3.14 Examples of broadband digital records proportional to ground velocity of the P-wave group from two earthquakes of similar magnitude mb in different source regions (uppermost traces) and their one-octave bandpass-filtered outputs. The numbers 1 to 9 on the filtered traces relate to the different center periods between 0.25 s (1) and 64 s (9) in one-octave distance. Note that the event record on the left has its maximum ground velocity (or maximum A/T) at trace 7, which corresponds to a center period of 16 s while it is at 1 s in the case of the records from the Kuril earthquake (copied from Duda, 1986; with permission of the BGR Hannover).

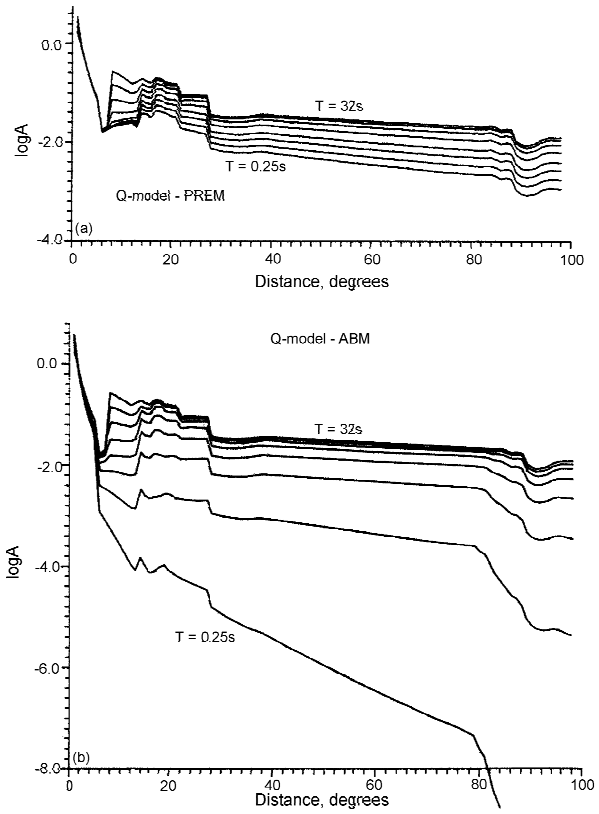

Fig. 3.15 Spectral amplitude-distance curves (in one-octave steps) as calculated for the IASP91 velocity model (Kennett and Engdahl, 1991) and two alternative Q-models according to Liu et al. (1976) as in the PREM model (upper diagram) and according to the ABM model of Anderson and Given (1982) (lower diagram) (modified from Tectonophysics, Vol. 217, Duda and Yanovskaya, 1993, Fig. 5, p. 263; with permission from Elsevier Science).

3.2.6.4 Short-period P-wave magnitude scale

Veith and Clawson (1972) developed a calibration function, $P(\Delta, h)_{SP}$, for short-period vertical-component P waves (Fig. 3.16) using data from underground nuclear explosions. It is consistent with observations and present-day concepts of attenuation. It looks much smoother than the curves $Q(\Delta, h)_{PZ}$ published by Gutenberg and Richter (1956a) and resembles an inverse A-Δ relationship for short-period P waves (see Fig. 3.13). For shallow events mb(P) values agree well with mb(Q) (average difference of - 0.03 magnitude units; Veith, 2001) but have less scatter. For deeper events, however, mb(P) is systematically lower than mb(Q) (up to about 0.4 magnitude units) due to a different attenuation law assumed in the upper mantle and transition zone (Veith, 2001). Deviating from the use of the Gutenberg-Richter Q functions, P values as given in Fig. 3.16 have to be used in conjunction with maximum P-wave peak-to-trough (2A) displacement amplitudes in units of nm (instead of μm). The Veith-Clawson calibration functions P(Δ, h) for short-period mb determination should be carefully considered by the IASPEI WG on Magnitude Measurements and existing discrepancies for deep earthquakes should be clarified. If P(Δ, h) in its present form or corrected for the currently best available attenuation model for short-period P waves promises to yield more reliable and stable mb values than mb(Q) its introduction as a new standard may be considered. Some related discussion is given below.

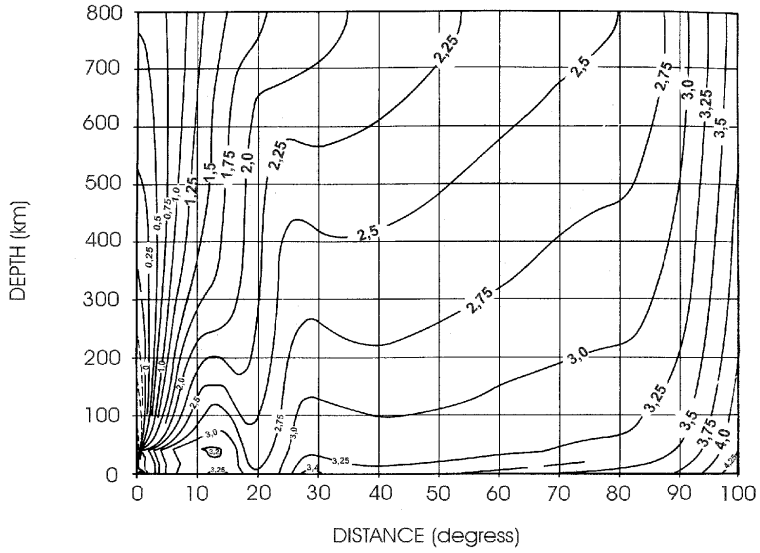

Fig. 3.16 Calibration functions P(Δ, h) for mb determination from narrow-band vertical-component short-period records with peak displacement magnification around 1 Hz (WWSSN-SP characteristic) according to Veith and Clawson (1972). **Note:** P values have to be used in conjunction with maximum P-wave peak-to-trough (2A!) amplitudes in units of nanometers (1 nm = 10^{-9}m). (Modified from Veith and Clawson, Magnitude from short-period P-wave data, BSSA, 62, 2, p. 446, © Seismological Society of America).

The Veith-Clawson magnitude calibration functions are officially used by the IDC in Vienna for mb determination although the IDC filter applied to the digital velocity-proportional broadband data prior to the amplitude measurements for mb results in a displacement response peaked around 4.5 Hz instead of around 1 Hz as required for the use of P(Δ, h). According to the spectral logA-D curves calculated by Duda and Yanovskaya (1993) for the PREM attenuation model, logA is, in the distance range between 10° and 100°, at 5 Hz at least 0.1 to 0.5 units smaller than at 1 Hz. The deviation may be even larger for other attenuation models (e.g., ABM; see Fig. 3.15). Thus, the use of P(Δ, h) in conjunction with the IDC filter response is physically not correct and tends to systematically underestimate mb. This is further aggravated by the fact that IDC determines A_{max} within a time window of only 5 s after the P onset. This heuristic procedure, although very suitable for a best possible discrimination between earthquakes and underground explosions on the basis of the mb/Ms criterion (see 11.2.5.2), is not appropriate, however, for proper earthquake scaling, at least for larger events with corner frequencies $f_c < 1$ Hz and multiple rupture process longer than 5 s.

Granville et al. (2002) analyzed 10 medium-size earthquakes in the depth range > 0 km to 530 km and with magnitudes mb between 6.4 and 6.8 according to the PDE (Preliminary Determination of Epicenters) reports of the United States Geological Survey (USGS) and 13 underground nuclear tests (UNTs) with PDE magnitudes mb between 4.6 and 6.1. They compared these data, which were derived from simulated WWSSN-SP records, by using the traditional procedure of mb determination based on the Gutenberg-Richter Q-functions, with a) the mb for the same WWSSN-SP data but calibrated with the Veith-Clawson relationship and b) the body-wave magnitudes reported in the REB (Reviewed Event Bulletin) of the PIDC. From this study the following conclusions were drawn:

- the agreement between mb(Q) (Gutenberg-Richter) and mb(P) (Veith-Clawson) based on WWSSN-SP data was reasonably good for the earthquakes (average difference mb(Q)-mb(P) = 0.2);
- for underground explosions (only shallow-depth events!) the agreement was even better (average mb(P)-mb(Q) = 0.09);
- the average discrepancy between mb(P) and mb(PIDC/REB) is much larger (0.5 magnitude units), although the latter are also scaled with the Veith-Clawson calibration functions. For 63% of the earthquake observations the difference was at least 0.4 mb units, and several of them had even an mb offset greater than 1 magnitude unit!;
- in contrast, the average discrepancy between mb(P) and mb(PIDC/REB) is 0.0 and 75% of the observations fall between – 0.1 and +0.1;
- the PIDC (now IDC in Vienna) procedure is adequate for mb determination of underground nuclear explosions, but not for earthquakes.

3.2.6.5 Short-period PKP-wave magnitude

Calibration functions $Q(\Delta, h)_{PKP}$ for short-period amplitude and period readings from all three types of direct core phases (PKPab, PKPbc and PKPdf) have been developed by Wendt (see Bormann and Wendt, 1999; explanations and Figure 3 in DS 3.1). These phases appear in the distance range $\Delta = 145° - 164°$ (see Fig. 3.13, Figs. 11.62-63 and Figure 1 in EX 11.3) with amplitude levels comparable to those of P waves in the distance range $25° < \Delta < 80°$. Many earthquakes, especially in the Pacific (e.g., Tonga-Fiji-Kermadec Islands) occur in areas with no good local or regional seismic networks. Often these events, especially the weaker ones, are also not well recorded by more remote stations in the P-wave range but often excellently observed in the PKP distance range, e.g., in Central Europe. This also applies to several other event-station configurations. Available seismic information from PKP wave recordings could, therefore, improve magnitude estimates of events not well covered by P-wave observations.

3.2.6.6 Lg-wave magnitudes

Sg and Lg waves (see 2.3.3), recorded at local and regional distances and with periods T < 3 s, are often used for magnitude determination. Lg propagates well in continental platform areas and may be prominent up to about 30°. Lg magnitudes are calibrated either with respect to (or in a similar way as) Ml or to teleseismic mb. In the latter case they are usually termed mbLg or Mn (Ebel, 1982). Lg magnitudes allow rather stable magnitude estimates with small scatter. NEIC uses the original formulas derived by Nuttli (1973) for eastern North America:

$$mbLg = 3.75 + 0.90 \log\Delta + \log(A/T), \text{ for } 0.5° \le \Delta \le 4° \quad (3.21a)$$

$$mbLg = 3.30 + 1.66 \log\Delta + \log(A/T), \text{ for } 4° \le \Delta \le 30°. \quad (3.21b)$$

where A is the ground amplitude of the Lg trace maximum in μm and T its period in the range $0.6 \text{ s} \le T \le 1.4$ s. Båth et al. (1976) developed a similar Lg scale for Sweden which is widely used in Scandinavia. Street (1976) recommended a unified mbLg magnitude scale between central and northeastern North America. Herrmann and Nuttli (1982) showed (later also Kim, 1998) that mbLg values are commonly similar to Ml when based on amplitude readings with periods around 1 s. They also proposed to define regional attenuation relations so that mbLg/Mn from different regions predict the same near source ground motions. Herrmann and

Kijko (1983) developed a frequency-dependent scales mLg(f) in order to broaden the frequency domain within which mbLg is applicable. Ebel (1994) proposed mLg(f), calibrated to mb and computed with appropriate Lg spatial attenuation functions, to become the standard for regional seismic networks in northeastern North America. Ambraseys (1985) published calibration Q_g (for Sg and Lg) and Q_R (for crustal Rayleigh waves), respectively that are applicable for northwestern European earthquakes in the distance range $0.5° < D < 11°$.

Stable single-station estimates of magnitudes from Nevada test site underground nuclear explosions have been made by Mayeda (1993) using 1-Hz Lg-coda envelopes. As compared with Lg-magnitude estimates using third peak or RMS amplitudes, these coda magnitudes have generally a five times smaller scatter (0.03 to 0.04 magnitude units only). Rautian et al. (1981) had proposed earlier the use of coda amplitude, not duration, in the definition of coda-based magnitude. They designed two particular scales based on the records of short-period (SP) and medium-period (MP) instruments. A scale of this kind is used routinely by the Kamchatka seismic network (Lemzikov and Gusev, 1989). The main advantage of such magnitude scales is their unique intrinsic accuracy; even a single-station estimate has a root-mean-square (RMS) error of only 0.1 or even less.

3.2.6.7 Macroseismic magnitudes

Other efforts are directed at developing magnitude scales which are best suited for earthquake engineering assessment of potential damage and thus seismic risk. These efforts go in two directions: by relating M to macroseismic intensity I and/or shaking area A_I or by focusing on the high-frequency content of seismic records.

Macroseismic magnitudes, M_{ms} are particularly important for the analysis and statistical treatment of historical earthquakes. They were initially proposed by Kawasumi (1951) as the intensity at the 100 km distance, following Richter's definition of Ml as closely as possible. This approach is physically quite reasonable because for most earthquakes a distance of 100 km is already the far field and source finiteness can be ignored. This approach was further developed by Rautian et al. (1989). On the other hand, I_0 based definitions implicitly assume the point source model and must be often misleading. Of course, with historic catalogs, there is no other way. There are three main ways to compute macroseismic magnitudes:

1) M_{ms} is derived from the epicentral intensity I_0 (or the maximum reported intensity, I_{max}) assuming that the earthquake effects in the epicentral area are more or less representative of the strength of the event;
2) M_{ms} is derived from taking into consideration the whole macroseismic field, i.e., the size of the shaking is related to different degrees of intensity or the total area of perceptibility, A;
3) M_{ms} is related to the product $P = I_0 \times A$ which is nearly independent of the focal depth, h, which is often not reliably known.

Accordingly, formulae for M_{ms} have the general form of

$$M_{ms} = a\, I_0 + b\,, \tag{3.22}$$

or, whenever the focal depth h (in km) is known

$$M_{ms} = c\ I_0 + \log h + d, \tag{3.23}$$

or, when using the shaking area A_{Ii} (in km^2) instead,

$$M_{ms} = e \log A_{Ii} + f \tag{3.24}$$

with A_{Ii} in km^2 shaken by intensities I_i with $i \geq$ III, ..., VIII, respectively. Sometimes the mean radius R_{Ii} of the shaking area related to a given isoseismal intensity is used instead of the area A_i and (3.22) is then written (e.g., by Greenhalgh et al. 1989 and with M_{ms} scaled to M_L) as

$$M_{ms} = g \log R_{Ii}^2 + h \log R_{Ii} + j. \tag{3.25}$$

In these relationships a through j are different constants. They have to be determined independently for different regions. Most often M_{ms} is scaled to Ml which has proven to be best related to earthquake damage and engineering applications. Examples for regionally best fitting relationships according to equation (3.22) to (3.25) have been published for California and Western Nevada by Toppozada (1975), for Italy by Tinti et al. (1987) and for Australia by Greenhalgh et al. (1989). For Europe, the relationship by Karnik (1969) yields the best results:

$$M_{ms} = 0.5\ I_0 + \log h + 0.35. \tag{3.26}$$

Frankel (1994) compared felt area and moment magnitudes for California with its young mountain ranges with a global data set of earthquakes in stable continental regions (SCRs) such as central USA (Fig. 3.17). The main reason is that the average attenuation is at frequencies around 2-4 Hz, which is the range of best human perceptibility to ground shaking, is very different in these regions. After Frankel (1994), Q is about 490 and 1600, respectively.

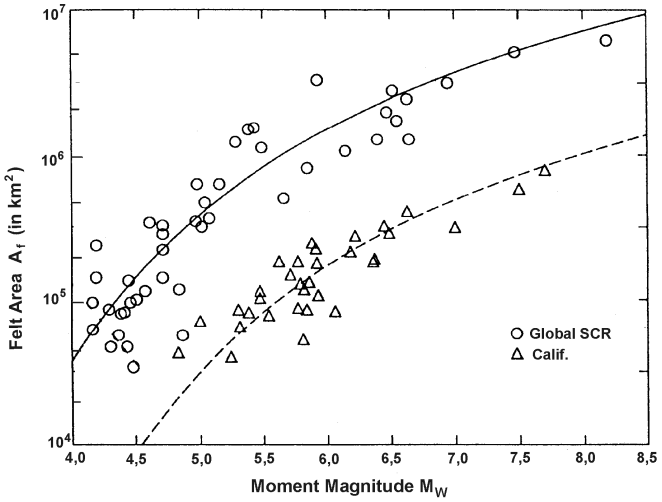

Fig. 3.17 Felt area A_f (in km^2) plotted against moment magnitude, $M_{w,}$ for global data from stable continental regions (SCR) (open circles; from Johnston, 1993) and California data (triangles, from Hanks et al., 1975; Hanks and Johnston, 1992). Solid and dashed lines are fits according to an equation given by Frankel (1994) (modified from Frankel, Implications of felt area-magnitude relations for earthquake scaling and the average frequency of perceptible ground motion, Bull. Seism. Soc. Am., Vol. 84, No. 2, Fig. 1, p. 463, 1994; © Seismological Society of America).

Another M_{ms} scale based on $P = I_0 \times A$ (in km^2) had been published by Galanopoulos (1961):

$$M_{ms} = \log P + 0.2 (\log P - 6). \quad (3.27)$$

A macroseismic magnitude scaled to the body-wave magnitude of Central United States earthquakes in the range $2.7 \le mb \le 5.5$ was developed by Nuttli and Zollweg (1974):

$$mb = 2.65 + 0.098 \log A_f + 0.054 (\log A_f)^2. \quad (3.28)$$

It is applicable for magnitude estimates of central United States earthquakes with felt areas of shaking $A_f \le 10^6$ km^2 for which there are intensity maps but no instrumental data available.

A related problem is the determination of magnitudes of prehistoric and historic (pre-instrumental) earthquakes from dimensions (length L, width W and/or dislocation D) of observed seismo-dislocations (e.g., Khromovskikh, 1989; Wells and Coppersmith, 1994; Mason, 1996) based on correlation relationships between magnitudes and respective field data from recent events (see 3.6).

3.2.6.8 High-frequency moments and magnitudes

Koyama and Zheng (1985) developed a kind of short-period seismic moment M_1 which is related to the source excitation of short-period seismic waves and scaled to mb according to

$$\log M_1 = 1.24\ mb + 10.9 \quad (\text{with } M_l \text{ in } J = Nm). \quad (3.29)$$

They determined M_1 from WWSSN short-period analog recordings by applying an innovative approximation of spectral amplitudes

$$Y(f) = 1.07\ A_{max}\ (\tau/f_0)^{1/2} \quad (3.30)$$

with A_{max} - maximum amplitude, f_0 - dominant frequency and τ - a characteristic duration of the complicated wave-packets. They analyzed more than 900 short-period recordings from 79 large earthquakes throughout the world in the moment range $7.5 \times 10^{17} \le M_0 \le 7.5 \times 10^{22}$ Nm. M_1 did not saturate in this range!

More recently, Atkinson and Hanks (1995) proposed a high-frequency magnitude scale

$$\mathbf{m} = 2 \log a_{hf} + 3 \quad (3.31)$$

with a_{hf} as the high-frequency level of the Fourier amplitude spectrum of acceleration in cm/s, i.e., for $f >> f_c$. They use average or random horizontal component accelerometer amplitudes at a distance of 10 km from the hypocenter or from the closest fault segment. **m** has been scaled to the moment magnitude **M** = Mw for events of average stress drop in eastern North America and California. When **M** is known, **m** is a measure of stress drop. For large pre-instrumental earthquakes **m** can more reliably be estimated than **M** from the felt area of earthquake shaking (see 3.2.6.7). When used together, **m** and **M** provide a good index of ground motion over the entire engineering frequency band, allow better estimates of response spectra and peak ground motions and thus of seismic hazard.

3.2.6.9 Tsunami magnitudes

A different kind of magnitude is the tsunami magnitude scale M_t. According to Abe (1989)

$$M_t = \log H_{max} + a \log \Delta + C \qquad (3.32)$$

where H_{max} is the maximum single (crest or trough) amplitude of tsunami waves in m as measured by tide-gage records and /or as derived from maximum inundation height, Δ - epicentral distance in km to the respective tide station and a and C - constants (a was found to be almost 1). In case of the long-wave approximation, i.e., with tsunami wavelengths being much larger than the bathymetric depths, the maximum tsunami height is strictly related to the maximum *vertical* deformation of the ocean bottom, $D_{\perp max}$, and thus to the seismic moment M_0. M_t was calibrated, therefore, with the average condition M_t = Mw for the calibration data set. This resulted in:

$$M_t = \log H_{max} + \log \Delta + 5.8. \qquad (3.33)$$

(3.33) shows no saturation. For the Chile earthquake 1960 M_t = 9.4 while M_w = 9.5. Sometimes, very slow but large ruptures with a large seismic moment cause much stronger tsunami than would have been expected from their surface wave, energy or body-wave magnitudes Ms, Me or mb, respectively. Such events are called "tsunami earthquakes". A striking example is the April 1, 1946 Aleutian earthquake with Ms = 7.3 and M_t = 9.3. Such strong but very slow earthquakes may have negligibly small energy in the high-frequency range and cause no or only minor shaking damage (see paragraph below Eq. 3.20).

3.2.7 Relationships among magnitude scales

Gutenberg and Richter (1956a and b) provided correlation relations between various magnitude scales:

$$m = 2.5 + 0.63\ Ms \qquad (3.34)$$

$$m = 1.7 + 0.8\ Ml - 0.01\ Ml^2 \quad \text{and} \qquad (3.35)$$

$$Ms = 1.27\ (Ml - 1) - 0.016\ Ml^2, \qquad (3.36)$$

where m is the unified magnitude as the weighted mean of the body-wave magnitudes mB determined from medium-period recordings. Practically the same relation as (3.34) was derived later by Abe and Kanamori (1980): mB = 2.5 + 0.65 Ms, which is good up to Mw = 8-8.5; thereafter it shows saturation. Note, however, when using Eq. (3.34) and Eq. (3.84) in section 3.6.2 that the average difference between the Gutenberg-Richter Ms and the “Prague” Ms is about 0.2 magnitude units (see Eq. (3.11).

Note that all these relations resulted from single random-variable parameter regression analysis assuming that the independent variable X (on the right side of the equation) is known and not afflicted with random errors and that the data scatter observed is due to random errors in the Y- (ordinate) direction only. Often they are wrongly applied, e.g., by solving Eq. (3.34) for Ms and calculating Ms for short-period mb values as published by international data centers and finally calculating seismic energy E_S via E_S-Ms relationships (see 3.6). Note that Eq. (3.34) is an optimal estimator for mB but not for Ms! In fact, both mB and Ms

determinations are afflicted with random errors and both account for the data scatter in an empirical mB-Ms diagram. Therefore, only a two random-variable parameter regression (so-called "orthogonal regression") analysis yields equations which can be used both ways for optimal parameter estimation (Bormann and Khalturin, 1975; Bormann and Wylegalla, 1975, Ambraseys, 1990). Equivalent to it are non-linear “maximum-likelihood” regressions as they have been systematically applied by Gusev (1991) to investigate the relationship between Mw and the magnitudes mb (with A_{max} within first few seconds only), mSKM (with A_{max} in the whole P-wave group), mB, m_b^* and $\widehat{m}_b$, Ml, Ms, and M(JMA) in both graphic and tabular form. Another paper comparing different magnitude scales was published by Utsu (1982).

When using medium-period readings of P and surface waves in displacement broadband records of type C (Kirnos SKD; see Fig. 3.11) and single random parameter regression, practically identical relationships to Eq. (3.34) were found both by Bune et al. (1970) on the basis of records of the former Soviet station network and by Bormann and Wylegalla (1975) for a single station in Germany (MOX; magnitude range 4.7 to 8.5). The latter is

$$MPV = 2.5 + 0.60\ MLH. \qquad (3.37)$$

Note that the related orthogonal regression to Eq. (3.37), calculated for the same data set, is rather different:

$$MPV - 0.70\ MLH = 1.83 \qquad (3.38)$$

and that the respective best fitting single random-parameter regression with respect to MLH is

$$MLH = - 1.54 + 1.25\ MPV. \qquad (3.39)$$

The latter is clearly different from

$$MLH = - 4.17 + 1.67\ MPV \qquad (3.40)$$

which one gets when resolving incorrectly Eq. (3.37) for MLH. As compared to Eq. (3.39), Eq. (3.40) results in an overestimation of MLH by about 1.2 magnitude units for mB = 8 and an underestimation of 0.8 units for mB = 5!

The single random-parameter regression relationship between short-period mb and Ms is very different from Eq. (3.34), namely, according to Gordon (1971),

$$mb = (0.47 \pm 0.02)\ Ms + (2.79 \pm 0.09) \qquad (3.41)$$

for a global station-earthquake data set. This agrees very well with the single-station average formula derived by Karnik (1972) for the Czech station Pruhonice (PRU):

$$mb(sp, PRU) = 0.47\ MLH + 2.95. \qquad (3.42)$$

The orthogonal correlation between surface-wave magnitudes determined from vertical and horizontal component recordings using the so-called Prague-Moscow calibration function Eq. (3.10) is, according to Bormann and Wylegalla (1975), nearly ideal, namely:

$$MLV - 0.97\ MLH = 0.19 \qquad (3.43)$$

with a standard deviation of only 0.11 and a correlation coefficient of r = 0.98. This clearly justifies the use of this calibration function, which was originally derived from horizontal amplitude readings, for vertical component (Rayleigh wave) magnitude determinations, too.

When using medium-period broadband data only, the orthogonal regression relation between magnitude determinations from PV and PPV or SH waves, respectively, are almost ideal. Gutenberg and Richter (1956a) had published Q-functions for all three phases (see Figures 1a-c and Table 6 in DS 3.1). Bormann and Wylegalla (1975) found for a global earthquake data set recorded at station MOX the orthogonal fits:

$$MPPV - MPV = 0.05 \tag{3.44}$$

with a standard deviation of only ± 0.15 magnitude units and

$$MSH - 1.1\ MPV = -\ 0.64, \tag{3.45}$$

with a standard deviation of ± 0.19 and magnitude values for P and S waves, which differ in the whole range of MPV(=mB) between 4 and 8 less than 0.25 units from each other. This confirms the good mutual scaling of these original body-wave calibration functions with each other, provided that they are correctly applied to medium-period data only. Therefore, it is not understandable why the international data centers do not encourage data producers to report also amplitudes from PPV and SH waves for proper determination of mB.

Kanamori (1983) summarized the relationship between the various magnitude scales in graphical form (Fig. 3.18). It also gives the ranges of uncertainty for the various magnitude scales due to observational errors and intrinsic variations in source properties related to differences in stress drop, complexity, fault geometry and size, source depth etc. The range of periods for which these magnitudes are determined are for mb: ≈1 s; for Ml: ≈ 0.1 - 3 s; for mB: ≈ 0.5 - 15 s; for Ms: ≈ 20 s and for Mw: ≈ 10 → ∞ s. Accordingly, these different magnitude scales saturate differently: the shorter the dominating periods the earlier saturation occurs, i.e., for mb around 6.5, Ml around 7, mB at about 8 and Ms at about 8.5 while Mw does not saturate. This is in good agreement with the general conclusions drawn on the basis of seismic source spectra (see Fig. 3.5).

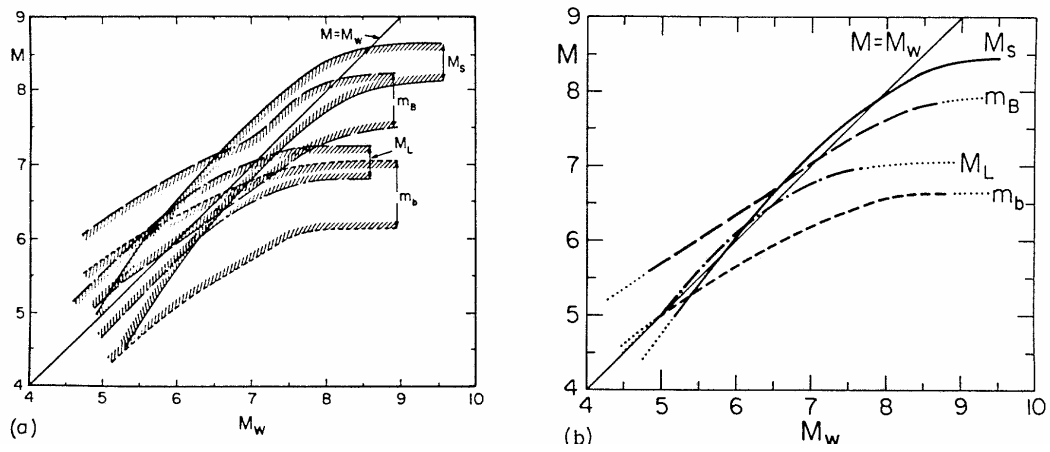

Fig. 3.18 Relations between magnitude scales (reprinted from Tectonophysics, 93, No. 3/4 Kanamori, Magnitude scale and quantification of earthquakes, 1983, Fig. 4, p. 193; with permission from Elsevier Science Publishers). Note the saturation of mb, mB, Ml and Ms.

Ambrasseys (1990), in an effort to arrive at uniform magnitudes for European earthquakes, re-evaluated magnitudes in the range 3 < M < 8. He derived the following *orthogonal regression relationships* between the various common magnitude scales:

$$0.75\ mb - 0.66\ mB = 0.21 \tag{3.46}$$

$$0.77\ mb - 0.64\ Ml = 0.73 \tag{3.47}$$

$$0.86\ mb - 0.49\ Ms = 1.94 \tag{3.48}$$

$$0.80\ Ml - 0.60\ Ms = 1.04 \tag{3.49}$$

with mb being determined according to the ISC procedure from short-period P-wave recordings and mB using medium-period P-wave records. These relations can be solved for either one of the two variables. Other relationships have been published by Nuttli (1985) which allow estimating Ms for plate-margin earthquakes when mb is known. For mb > 5 their results differ less than 0.2 magnitude units from those of Eq. (3.48) when solved for Ms.

3.2.8 Summary remarks about magnitudes and their perspective

Magnitude was originally intended to be a measure of earthquake size in terms of the seismic energy E_S released by the source. E_S, which is proportional to the squared velocity of ground motion, can theoretically be obtained by integrating spectral energy density over all frequencies contained in the transient waveform, e.g., of the P-, S- or surface-wave train. This procedure could not be carried out efficiently with analog recordings. Therefore, Gutenberg (1945 a, b and c) assumed that the maximum amplitude observed in a wave group was a good measure of the total energy in that arrival. As classical seismographs were relatively broadband displacement sensors, he obtained a measure of ground motion velocity by dividing the measured maximum ground displacement by the associated period [see Eqs. (3.10) and (3.13) for surface- and body-wave magnitudes]. Note, however, that the related calibration functions did not account for frequency-dependent attenuation. Calibration functions are, therefore, usually applied only over rather limited frequency ranges, e.g., around 1 Hz and 0.05 Hz, respectively.

According to Fig. 3.5, magnitude can be a reasonable measure of E_S only if it samples the maximum amplitudes in the velocity spectrum which occur at the corner frequency f_c of the displacement "source spectrum"; f_c decreases with increasing seismic moment and, thus, with magnitude. Most classical band-limited seismic recordings sampled the ground motion over a bandwidth of not more than 0.3 to 0.9 decades (see Fig. 3.11). Hence, sampling of spectral amplitudes at frequencies smaller or larger than f_c of the wave spectrum underestimates the maximum ground velocity and, thus, E_S. This is the case for the body-wave magnitude mb, which is determined from narrow-band short-period recordings centered around 1 Hz, for magnitudes larger than about 5. Similarly, Ms, which is determined from surface waves with $T \approx 20$ s, underestimates maximum ground velocity and E_S for Ms < 6 and for Ms> 7.5.

One must also recognize that all band-limited magnitudes saturate, e.g., mb saturates for magnitudes > 6.5 and Ms saturates for magnitudes > about 8.5. However, mB, determined from medium-period records saturates later than mb (see Fig. 3.18). To overcome this problem, magnitude determinations should be based on broadband digital recordings with a bandwidth of ideally about 4 decades or even more. Only then it can be assured that the peak of the ground-velocity spectrum as well as a fair part of higher and lower frequencies on both

sides of the corner frequency are covered within the passband of the seismograph. This passband is sufficient to allow determination of both the scalar seismic moment M_0 (and the associated moment magnitude Mw) and the radiated energy E_S (and the associated energy magnitude Me). Both Mw and Me do not saturate. However, note that they express different aspects of the seismic source and may differ by more than one magnitude unit (see Tab. 3.2). Also, direct determination of E_S is not trivial and requires a good distribution of stations. Nevertheless, a single station, when equipped with a velocity-proportional digital broadband sensor, could easily determine a non-saturating mB (see 3.2.6.3) by sampling the maximum amplitudes of ground velocity. Such an mB might be a good preliminary estimate of Me and the high-frequency energy released by the source. This needs to be tested with real data, however, the required frequency-dependent calibration functions are not yet well established. This should become a priority task of the IASPEI WG on magnitudes.

Despite the advantage of more physically based broadband magnitudes, the overwhelming majority of magnitude data is and will continue to be based for quite some more time on band-limited recordings using the classical formulas. In many earthquake-prone regions, particularly those lacking historical macroseismic data and strong-motion records, seismic hazard assessment rests on the availability of such data. Moreover, band-limited magnitudes sometimes have value for purposes other than energy or moment estimates. E.g., the mb/Ms ratio is a very powerful teleseismic discriminator between earthquakes and underground nuclear explosions, and Ml is, at least up to medium-size earthquakes, well scaled with macroseismic intensity and, thus, damage. Therefore, magnitudes of different kinds will still be needed in the foreseeable future. Their proper use, however, requires an understanding of their potentials, limitations, original definitions and mutual relationships. Finally, one has to assure the long-term continuity and stability of magnitude values according to agreed standards of measurement by annotating different magnitudes in an unambiguous way (see IS 3.2), and by refraining from one-sided, internationally unrecognized and improperly documented changes in procedures which may cause baseline changes in earthquake catalogs. This section aimed at creating awareness and setting standards on this important issue.

3.3 Radiated seismic energy and energy magnitude (G. L. Choy and J. Boatwright)

3.3.1 Introduction

One of the most fundamental parameters for describing an earthquake is radiated seismic energy. In theory, its computation simply requires an integration of radiated energy flux in velocity-squared seismograms. In practice, energy has historically almost always been estimated with empirical formulas. The empirical approach dominated for two major reasons. First, until the 1980's most seismic data were analog, a format which was not amenable to spectral processing on a routine basis. Second, an accurate estimate of radiated energy requires the analysis of spectral information both above and below the corner frequency of an earthquake, about which energy density is most strongly peaked.

Prior to the worldwide deployment of broadband seismometers, which started in the 1970's, most seismograms were recorded by conventional seismographs with narrowly peaked instrument responses. The difficulties in processing analog data were thus compounded by the limitations in retrieving reliable spectral information over a broad bandwidth. Fortunately, theoretical and technological impediments to the direct computation of radiated energy have

been removed. The requisite spectral bandwidth is now recorded digitally by a number of seismograph networks and arrays with broadband capability, and frequency-dependent corrections for source mechanism and wave propagation are better understood now than at the time empirical formulas were first developed.

3.3.2 How is radiated seismic energy measured?

3.3.2.1 Method

The method described below for estimating the radiated seismic energy of teleseismic earthquakes is based on Boatwright and Choy (1986). Velocity-squared spectra of body waves are corrected for effects arising from source mechanism, depth phases, and propagation through the Earth.

For shallow earthquakes where the source functions of direct and surface-reflected body-wave arrivals may overlap in time, the radiated energy of a *P*-wave group (consisting of *P*, *pP* and *sP*) is related to the energy flux by

$$E_S^P = 4\pi \, <F^P>^2 \left(\frac{R^P}{F^{gP}} \right)^2 \varepsilon_{gP}^* \tag{3.50}$$

where the P-wave energy flux, ε_{gP}^*, is the integral of the square of the ground velocity, taken over the duration of the body-wave arrival,

$$\varepsilon_{gP}^* = \rho\alpha \int_0^\infty \dot{u}(t)^2 \, dt \tag{3.51}$$

Here, $\dot{u}$ is velocity, which must be corrected for frequency-dependent attenuation; ρ and α are density and velocity at the receiver, respectively; $<F^P>^2$ is the mean-square radiation-pattern coefficient for *P* waves; R^P is the *P*-wave geometrical spreading factor; F^{gP} is the generalized radiation pattern coefficient for the *P*-wave group defined as

$$\left(F^{gP}\right)^2 = \left(F^P\right)^2 + \left(\hat{PP} \;\; F^{pP}\right)^2 + \frac{2\alpha q}{3\beta}\left(\hat{SP} \;\; F^{sP}\right)^2 \tag{3.52}$$

where F^i are the radiation-pattern coefficients for $i = P$, pP, and sP; $\hat{PP}$ and $\hat{SP}$ are plane-wave reflection coefficients of *pP* and *sP* at the free surface, respectively, corrected for free-surface amplification; and q is 15.6, the ratio of *S*-wave energy to *P*-wave energy (Boatwright and Fletcher, 1984). The correction factors explicitly take into account our knowledge that the earthquake is a double-couple, that measurements of the waveforms are affected by interference from depth phases, and that energy is partitioned between *P* and *S* waves. For teleseismically recorded earthquakes, energy is radiated predominantly in the bandwidth 0.01 to about 5.0 Hz. The wide bandwidth requires a frequency-dependent attenuation correction (Cormier, 1982). The correction is easily realized in the frequency domain by using Parseval's theorem to transform Eq. (3.51),

$$\varepsilon_{gP}^* = \frac{\rho\alpha}{\pi} \int_0^\infty \dot{u}(\omega)^2 e^{\omega t_\alpha^*} \, d\omega \tag{3.53}$$

where t_α^* is proportional to the integral over ray path of the imaginary part of complex slowness in an anelastic Earth. An appropriate operator, valid over the requisite broad

bandwidth, is described by Choy and Cormier (1986) and shown in Fig. 3.19. The t_α^* of the *P*-wave operator ranges from 1.0 s at 0.1 Hz to 0.5 s at 2.0 Hz.

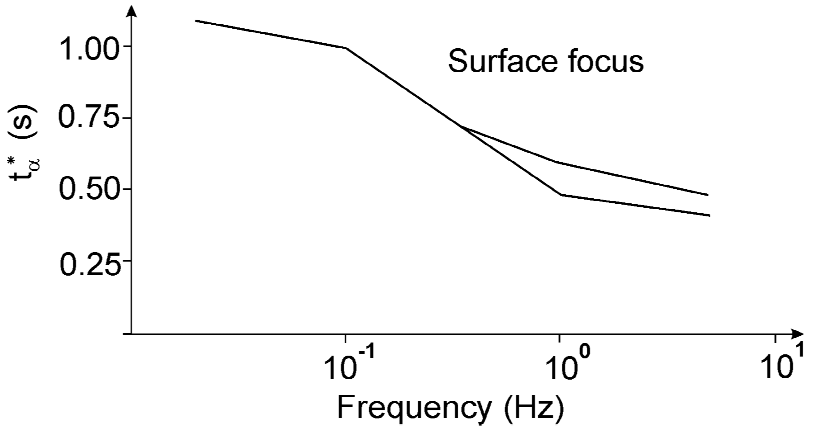

Fig. 3.19 Teleseismic t_α^* derived by Choy and Cormier (1986) plotted as a function of frequency for a surface-focus source and a surface receiver at a distance of 60°. The split in the curve at frequencies higher than 0.3 Hz indicates the variation in regional t_α^* expected for different receiver sites. In practice the mean of the two curves is used for the attenuation correction.

The numerical integration of Eq. (3.53) is limited to either the frequency at which signal falls below the noise level (typically at frequencies greater than 2.0-3.0 Hz) or to the Nyquist frequency. If this limiting or cutoff frequency, ω_c, is greater than the corner frequency, the remainder of the velocity spectrum is approximated by a curve that falls off by ω^{-1}. In practice, therefore, Eq. (3.53) consists of a numerical integral, *N*, truncated at ω_c, and a residual integral, *R*, which approximates the remainder of the integral out to infinite frequency,

$$\varepsilon_{gP}^* = \rho\alpha N + \rho\alpha R \tag{3.54}$$

where, as shown in Boatwright and Choy (1986),

$$R = \frac{\omega_c}{\pi}\left[\dot{u}_c(\omega_c)\right]^2 \tag{3.55}$$

in which $\dot{u}_c$ is the attenuation-corrected value of velocity at ω_c.

Although teleseismic *SH*- and *SV*-wave groups from shallow earthquakes can be analyzed through a straightforward extension of Eq. (3.50) as described in Boatwright and Choy (1986), shear waves suffer substantially more attenuation in propagation through the Earth than the *P* waves. The loss of seismic signal due to shear attenuation usually precludes retrieving useful spectral information for frequencies higher than about 0.2-0.3 Hz for all but the largest earthquakes. Thus, for the routine estimation of energy, it is more practical and more accurate to use only the *P*-wave group (Eqs. (3.50) and (3.53)). The formula for computing the total radiated energy when using the *P*-wave group alone is

$$E_s = (1+q)\,E_s^P\,. \tag{3.56}$$

3.3.2.2 Data

Data used in the direct measurement of energy must satisfy three requirements. First, the implementation of Eq. (3.53) requires that the velocity data contain spectral information about, above and below the corner frequency of an earthquake. Because the corner frequency can vary from earthquake to earthquake depending on source size and rupture complexity, the bandwidth of the data must be sufficiently wide so that it will always cover the requisite range of frequencies above and below the corner frequency. For body waves from teleseismically recorded earthquakes, a spectral response that is flat to ground velocity between 0.01 Hz through 5.0 Hz is usually sufficient. The second requirement is that the duration of the time window extracted from a seismogram should correspond to the time interval over which the fault is dynamically rupturing. As shown by the examples in Fig. 3.20, when broadband data are used, delimiting the time window is generally unequivocal regardless of the complexity of rupture or the size of the earthquake. The initial arrival of energy is obviously identified with the onset of the direct *P* wave. The radiation of energy becomes negligible when the amplitude of the velocity-squared signal decays to the level of the coda noise. The final requirement is that we use waveforms that are not complicated by triplications, diffractions or significant secondary phase arrivals. This restricts the usable distance range to stations within approximately 30°-90° of the epicenter. In addition, waveforms should not be used if the source duration of the *P*-wave group overlaps a significant secondary phase arrival. For example, this may occur when a very large earthquake generates a *P*-wave group with a duration of such length that it does not decay before the arrival of the *PP*-wave group.

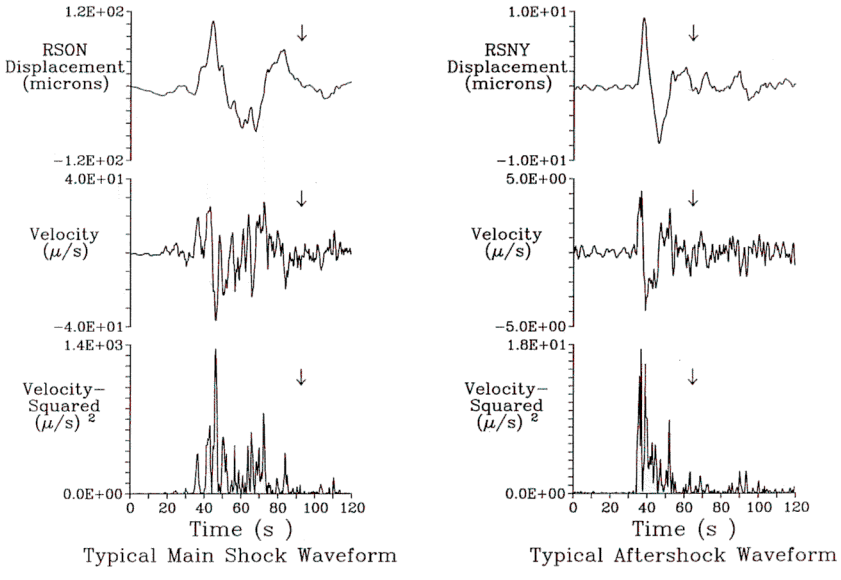

Fig. 3.20 (Left) Broadband displacement, velocity, and velocity-squared records for the large (Ms = 7.8, Me = 7.5, Mw = 7.7) Chilean earthquake of 3 March 1985. Rupture complexity, in the form of a tiny precursor and a number of sub-events, is typical for large earthquakes. (Right) Broadband displacement, velocity and velocity-squared records for an aftershock (mb = 5.9, Me = 6.2, Mw = 6.6) to the Chilean earthquake that occurred 17 March 1985. The waveforms are less complex than those of the main shock. Despite the differences in rupture complexity, duration and amplitude, the time window over which energy arrives is unequivocal. In each part of the figure the arrows indicate when the velocity-squared amplitude has decreased to the level of the coda noise.

3.3.3 Development of an energy magnitude, Me

In the Gutenberg-Richter formulation, an energy is constrained once magnitude is known through log E_S = a + b M where *a* and *b* are constants. For surface-wave magnitude, Ms, the Gutenberg-Richter formula takes the form

$$\log E_S = 4.8 + 1.5\ Ms \tag{3.57}$$

where E_S is in units of Joules (J). In the normal usage of Eq. (3.57), an energy is derived after an Ms is computed. However, it is now recognized that for very large earthquakes or very deep earthquakes, the single frequency used to compute Ms is not necessarily representative of the dimensions of the earthquake and, therefore, might not be representative of the radiated energy. Since radiated energy can now be computed directly, it is an independent parameter from which a unique magnitude can be defined. In Fig. 3.21, the radiated energies for a set of 378 global shallow earthquakes from Choy and Boatwright (1995) are plotted against their magnitudes, Ms. The Gutenberg-Richter relationship is plotted as a dashed line in Fig. 3.21. Assuming a b-value of 1.5, the least-squares regression fit between the actual energies and magnitude is

$$\log E_S = 4.4 + 1.5\ Ms \tag{3.58}$$

which is plotted as the solid line in Fig. 3.21. The *a*-value of 4.4 indicates that on average the original Gutenberg-Richter formula overestimates the radiated energy by a factor of two. To define energy magnitude, Me, we replace Ms with Me in Eq. (3.58)

$$\log E_S = 4.4 + 1.5\ Me \tag{3.59}$$

or

$$Me = 2/3 \log E_S - 2.9. \tag{3.60}$$

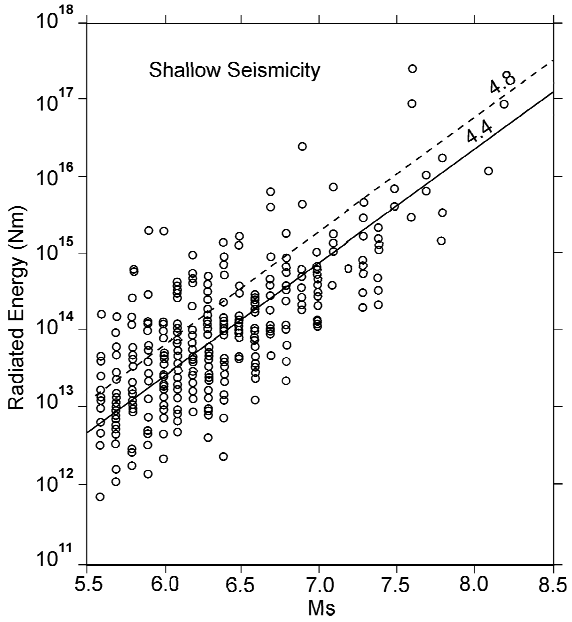

Fig. 3.21 Radiated energy (E_S) of global data as a function of surface-wave magnitude (Ms). The energy predicted by the Gutenberg-Richter formula, log E_S = 4.8 + 1.5 Ms (in units of Newton-meters), is shown by the dashed line. From a least-squares regression, the best-fitting line with the slope of 1.5 is log E_S= 4.4 + 1.5 Ms (according to Choy and Boatwright, 1995).

The usage of Eq. (3.60) is conceptually antithetical to that of Eq. (3.57). In Eq. (3.60) magnitude is derived explicitly from energy, whereas in Eq. (3.57) energy is dependent on the value of magnitude.

3.3.4 The relationship of radiated energy to moment and apparent stress

The energy and moment for a particular earthquake are related by apparent stress, σ_{app} (see Equation (59) in IS 3.1),

$$\sigma_{app} = \mu \, E_S / M_0 \tag{3.61}$$

where μ is the average rigidity at the source. When radiated energy, E_S, is plotted against seismic moment, M_0, for global shallow earthquakes (Fig. 3.22), the best fit by least-squares regression of E_S on M_0 (solid line) yields

$$E_S = 1.6 \cdot 10^{-5} M_0. \tag{3.62}$$

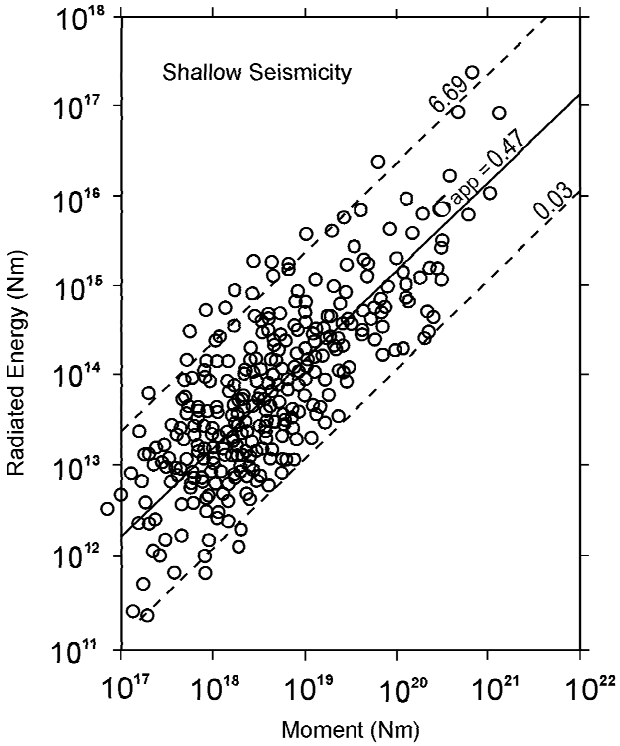

Fig. 3.22 Radiated energy, E_S, of 394 shallow-focus earthquakes as a function of seismic moment, M_0 . The slope of the least-squares log-normal regression (solid line) yields a global average apparent stress $\overline{\sigma}_{app}$ of about 0.5 MPa assuming a source rigidity of $0.3 \cdot 10^5$ MPa. The 95% spread (or width of distribution) about the regression line is indicated by the dashed lines (according to Choy and Boatwright, 1995).

Assuming an average rigidity for shallow earthquakes of $0.3 \cdot 10^5$ MPa, the slope of the regression line yields a worldwide average apparent stress, $\overline{\sigma}_{app}$ of about 0.47 MPa. The spread about the regression line is very large. In terms of apparent stress it is between 0.03 to 6.69 MPa. Empirical formulas, like those employing M_0 or Ms, ignore the spread and, thus,

would be poor predictors of energy. Viewing the spread of E_S-M_0 values about the regression line in terms of apparent stress, rather than random scatter, may provide significant insight into the physics of earthquake occurrence. For example, the release of energy and apparent stress could vary systematically as a function of faulting type, lithospheric strength and tectonic region (Choy and Boatwright,1995). As more statistics on the release of energy are accumulated, spatial and temporal variations in energy release and apparent stress might also be identified.

3.3.5 The relationship of Me to Mw

Although Me and Mw are magnitudes that describe the size of an earthquake, they are not equivalent. Me, being derived from velocity power spectra, is a measure of the radiated energy in form of seismic waves and thus of the seismic potential for damage to anthropogenic structures. Mw, being derived from the low-frequency asymptote of displacement spectra, is physically related to the final static displacement of an earthquake. Because they measure different physical properties of an earthquake, there is no *a priori* reason that they should be numerically equal for any given seismic event. The usual definition of Mw is:

$$Mw = 2/3 \log M_0 - 6.0 \qquad \text{(with } M_0 \text{ in Nm).} \qquad (3.63)$$

The condition under which Me is equal to Mw, found by equating Eq. (3.60) and Eq. (3.63), is $E_S/M_0 \sim 2.2 \cdot 10^{-5}$. From Eq. (3.61) this ratio is equivalent to $\sigma_{app} \sim 2.2 \cdot 10^{-5} \mu$. For shallow earthquakes, where $\mu \sim 0.3\text{-}0.6 \times 10^5$ MPa, this condition implies that Me and Mw will be coincident only for earthquakes with apparent stresses in the range 0.66-1.32 MPa. As seen in Fig. 3.22, this range is but a tiny fraction of the spread of apparent stresses found for earthquakes. Therefore, the energy magnitude, Me, is an essential complement to moment magnitude, Mw, for describing the size of an earthquake. How different these two magnitudes may be is illustrated in Tab. 3.2. Two earthquakes occurred in Chile within months of each other and their epicenters were less than 1° apart. Although their Mw's and Ms's were similar, their mb's and Me's differed by 1 to 1.4 magnitude units! Table 3.2 describes the macroseismic effects from the two earthquakes. The event with larger Me caused significantly greater damage!

Tab. 3.2 (Reprinted from Choy et al., 2001.)

Date	LAT (°)	LON (E)	Depth (km)	Me	Mw	mb	Ms	$sigma_a$ (bars)	Faulting Type
6 JUL 1997 (1)	-30.06	-71.87	23.0	6.1	6.9	5.8	6.5	1	interplate-thrust
15 OCT 1997 (2)	-30.93	-71.22	58.0	7.5	7.1	6.8	6.8	44	intraslab-normal

(1) Felt (III) at Coquimbo, La Serena, Ovalle and Vicuna.

(2) Five people killed at Pueblo Nuevo, one person killed at Coquimbo, one person killed at La Chimba and another died of a heart attack at Punitaqui. More than 300 people injured, 5,000 houses destroyed, 5,700 houses severely damaged, another 10,000 houses slightly damaged, numerous power and telephone outages, landslides and rockslides in the epicentral region. Some damage (VII) at La Serena and (VI) at Ovalle. Felt (VI) at Alto del Carmen and Illapel; (V) at Copiapo, Huasco, San Antonio, Santiago and Vallenar; (IV) at Caldera, Chanaral, Rancagua and Tierra Amarilla; (III) at Talca; (II) at Concepcion and Taltal. Felt as far south as Valdivia. Felt (V) in Mendoza and San Juan Provinces, Argentina. Felt in Buenos Aires, Catamarca, Cordoba, Distrito Federal and La Rioja Provinces, Argentina. Also felt in parts of Bolivia and Peru.

3.3.6 Regional estimates of radiated seismic energy

Radiated energy from local and regional records can be computed in a fashion analogous to the teleseismic approach if suitable attenuation corrections, local site and receiver effects, and hypocentral information are available or can be derived. Boatwright and Fletcher (1984) demonstrated that integrated ground velocity from S waves could be used to estimate radiated energy in either the time or frequency domain by,

$$E_s = 4\pi C^2 r^2 \rho_r \beta_r \int_0^\infty \dot{u}_c(t)^2 dt \tag{3.64}$$

$$= 4\pi C^2 r^2 \rho_r \beta_r \int_0^\infty \dot{u}_c(\omega)^2 \, d\omega \tag{3.65}$$

where the ground velocity has been corrected for anelastic attenuation, C is a correction for radiation pattern coefficient and free-surface amplification, r is the source-receiver distance, and ρ_r and β_r are density and S-wave velocity at the receiver. The attenuation correction is usually of the type $exp(\omega r/\beta Q)$, where Q is the whole-path attenuation. Similarly, Kanamori et al. (1993) use a time-domain method to estimate the S-wave energy radiated by large earthquakes in southern California,

$$E_\beta = 4\pi r^2 C_f^{-2} [r_0 q(r_0)/rq(r)]^2 \rho_0 \beta_0 \int_0^\infty \dot{u}^2(t) dt \tag{3.66}$$

where ρ_0 and β_0 are hypocentral density and S-wave velocity, C_f is the free-surface amplification factor, r is the source-receiver distance estimated from the epicentral distance Δ and a reference depth h of 8 km (such that $r^2=\Delta^2+h^2$). Attenuation is described by $q(r) = cr^{-n} \exp(-kr)$, which is the Richter (1935) attenuation curve as corrected by Jennings and Kanamori (1983). For southern California earthquakes, c=0.49710, n=1.0322, and k=0.0035 km^{-1}.

3.3.7 Conclusions

Energy gives a physically different measure of earthquake size than moment. Energy is derived from the velocity power spectra, while moment is derived from the low-frequency asymptote of the displacement spectra. Thus, energy is a better measure of the severity of shaking and thus of the seismic potential for damage, while moment, being related to the final static displacement, is more related to the long-term tectonic effects of the earthquake process. Systematic variations in the release of energy and apparent stress as a function of faulting type and tectonic setting can now be identified that were previously undetectable because of the lack of reliable energy estimates. An energy magnitude, Me, derived from an explicit computation of energy, can complement Mw and Ms in evaluating seismic and tsunamigenic potential.

3.4 Determination of fault-plane solutions (M. Baumbach, H. Grosser)

3.4.1 Introduction

The direction (polarity) and amplitude of motion of a seismic wave arriving at a distant station depends both on the wave type considered and the position of the station relative to the motion in the earthquake source. This is illustrated by Figs. 3.23a and b.

Fig. 3.23a represents a linear displacement of a point source **S** while Fig. 3.23b depicts a right lateral (dextral) shear dislocation along a fault plane **F**. Shear dislocations are the most common model to explain earthquake fault ruptures. Note that in the discussion below we consider the source to be a point source with rupture dimension much smaller than the distance to the stations and the wave length considered. First we look into the situation depicted in Fig. 3.23a. When S moves towards Δ1 then this station will observe a *compressional* (+) P-wave arrival (i.e., the first motion is *away* from **S**), Δ4 will record a P wave of opposite sign (-) , a *dilatation* (i.e., first motion *towards* **S**), and station Δ2 will receive no P wave at all. On the other hand, S waves, which are polarized parallel to the displacement of **S** and perpendicular to the direction of wave propagation, will be recorded at Δ2 but not at Δ1 and Δ4 while station Δ3 will receive both P and S waves.

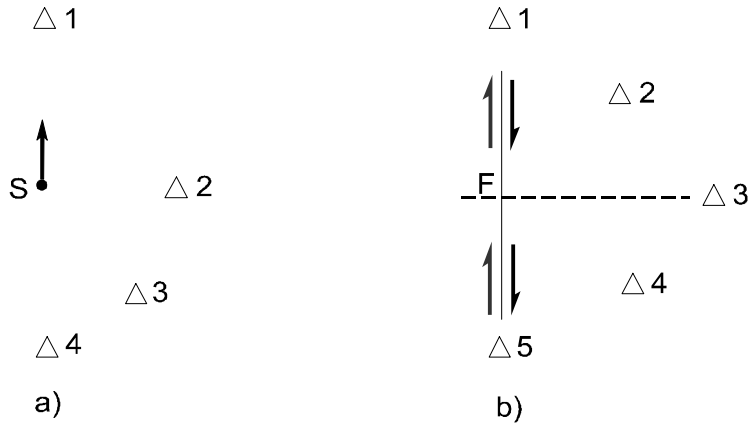

Fig. 3.23 Direction of source displacement with respect to seismic stations Δi for a) a single force at point S and b) a fault rupture F. Note that in the discussion below we consider the source to be a point source with a rupture dimension much smaller than the distance to the stations.

Somewhat different is the case of a fault rupture (Fig. 3.23b). At stations Δ1 and Δ5, which are positioned in the strike direction of the fault, the opposite signs of P motion on both side of the fault will cancel, i.e., no P waves will be observed. The latter also applies for station Δ3 which is sited perpendicular to the fault. On the other hand, stations Δ2 and Δ4, which are positioned at an angle of 45° with respect to the fault, will record the P-wave motions with maximum amplitudes but opposite sign. This becomes clear also from Fig. 3.25a. It shows the different polarities and the amplitude "lobes" in the four quadrants. The length of the displacement arrows is proportional to the P-wave amplitudes observed in different directions from the fault. Accordingly, by observing the sense of first motions of P waves at many stations at different azimuths with respect to the source it will be possible to deduce a "fault-

plane solution". But because of the symmetry of the first-motion patterns, two potential rupture planes, perpendicular to each other, can be constructed. Thus, on the basis of polarity data alone, an ambiguity will remain as to which one was the acting fault plane. This can only be decided by taking into account additional data on azimuthal amplitude and frequency or wave-form patterns, which are controlled by the Doppler effect of the moving source, and/or field data on the orientation and nature of seismotectonic faults.

In accordance with the above, the amplitude distribution of P waves for a point source with pure double-couple shear mechanism is described in a spherical co-ordinate system (θ, ϕ) (Aki and Richards, 1980; see Fig. 3.24) by

$$A_P(\theta, \phi) = \cos\phi \sin 2\theta. \tag{3.67}$$

This expression divides the focal sphere into four quadrants. The focal sphere for a seismic point source is conceived of as a sphere of arbitrarily small radius centered on the source. Within each quadrant the sign of the P-wave first motion (polarity) does not change but amplitudes are large in the center of the quadrant and small (or zero) near to (or at) the fault plane and the auxiliary plane. The nodal lines for P waves, on which $A_P(\theta, \phi) = \cos\phi \sin 2\theta = 0$, separate the quadrants. They coincide with the horizontal projection of the two orthogonal fault planes traces through the focal sphere. Opposite quadrants have the same polarity, neighboring quadrants different polarities. Note that *compression* is observed at stations falling in the *tension quadrant* (force directed away from the point source) while *dilatation* is observed at stations falling in the *compression quadrant* (force directed towards the point source).

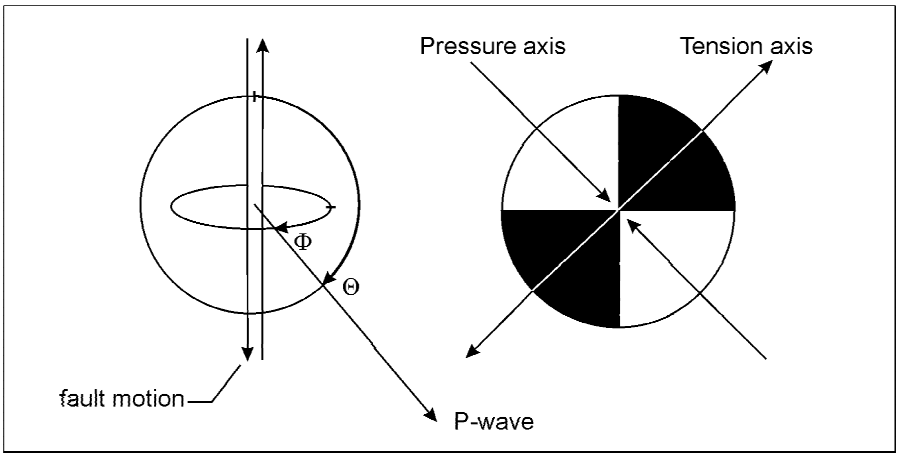

Fig. 3.24 Map view of P-wave radiation pattern for a shear fault. θ is the azimuth in the plane while ϕ is in fact three-dimensional. See also Fig. 3.23. Black areas: polarity +, white areas - .

The position of the quadrants on the focal sphere depends on the orientation of the active fault and of the slip direction in space. This is illustrated by Fig. 3.25, which shows the P-wave radiation pattern for a thrust event with some strike-slip component. Thus, the estimation of the P-wave first motion polarities and their back-projection onto the focal sphere allows us to identify the type of focal mechanism of a shear event (fault-plane solution). The only problem is, that the hypocenter and the seismic ray path from the source to the individual stations must be known. This may be difficult for a heterogeneous model with 2-D or 3-D velocity structure.

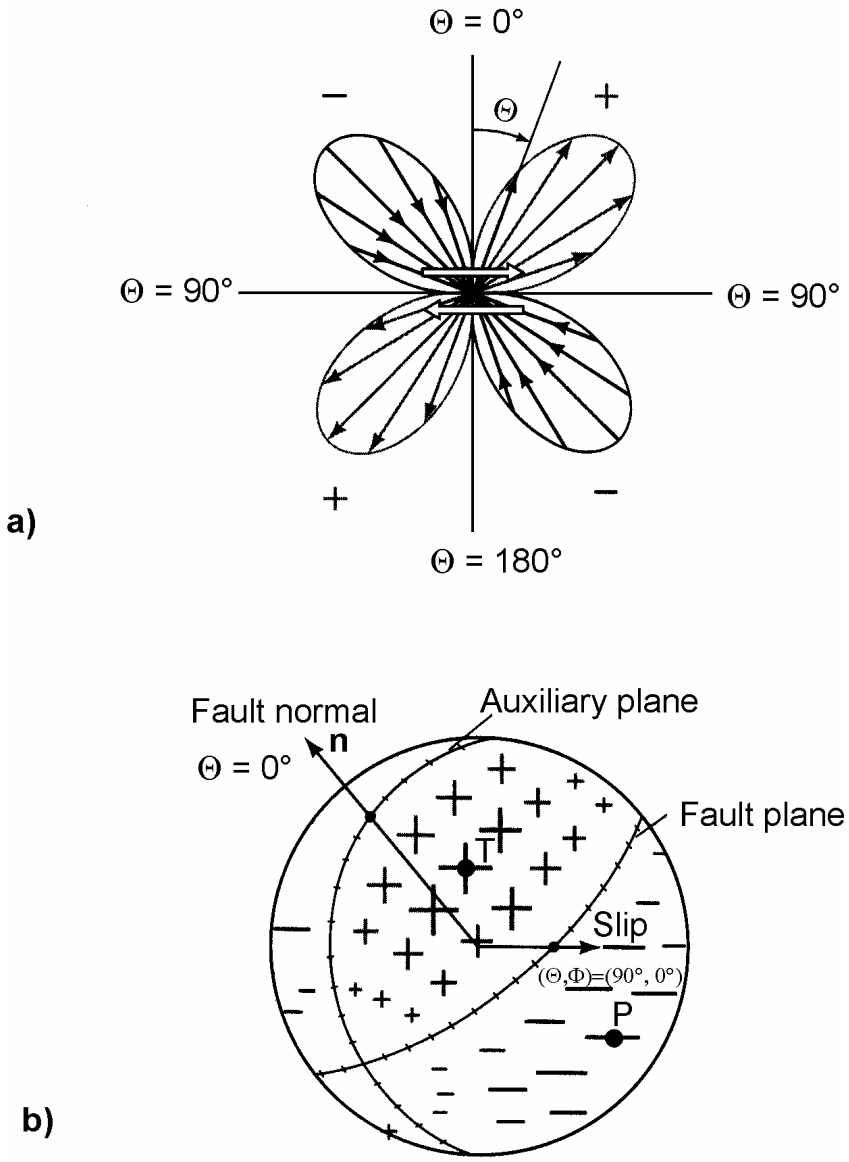

Fig. 3.25 Radiation pattern of the radial displacement component (P wave) due to a double-couple source: a) for a plane of constant azimuth (with lobe amplitudes proportional to $\sin 2\theta$) and b) over a sphere centered on the origin. Plus and minus signs of various sizes denote amplitude variation (with θ and ϕ) of outward and inward directed motions. The fault plane and auxiliary plane are nodal lines on which $\cos\phi \sin 2\theta = 0$. The pair of arrows in a) at the center denotes the shear dislocation. P and T mark the penetration points of the pressure and tension axes, respectively, through the focal sphere. Note the alternating quadrants of inward and outward directions of motion (compressional quadrant +; dilatational quadrant -) (modified from Aki and Richards 1980 ; with kind permission of the authors).

Fault-plane solutions based on P-wave first motion polarities will be better constrained if additionally the different radiation pattern of S waves displacement amplitudes is taken into account. An example is given in Fig. 3.26 for the same fault-plane solution as shown in Fig. 3.25 for P waves.

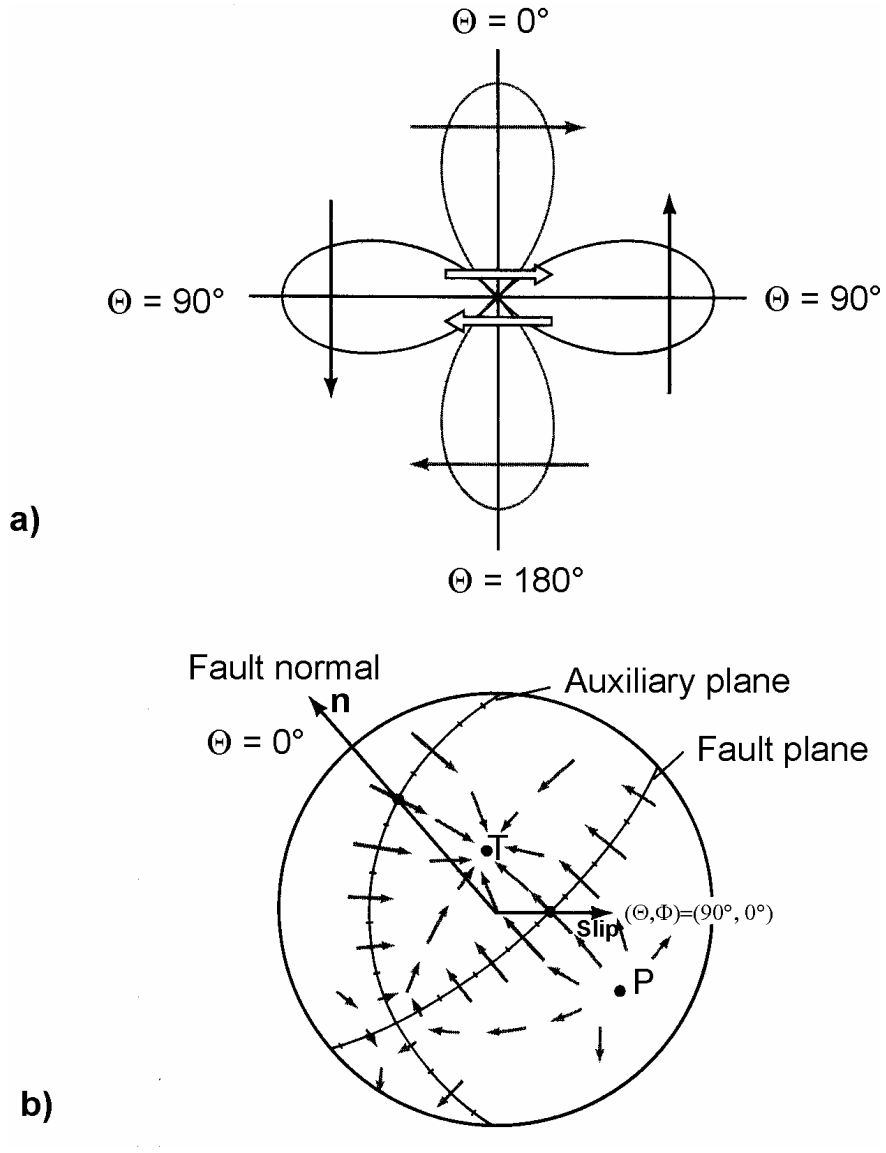

Fig. 3.26 Radiation pattern of the transverse displacement component (S wave) due to a double-couple source. a) in the plane $\{\phi = 0, \phi = \pi\}$ and b) over a sphere centered on the origin. Arrows imposed on each lobe in a) show the direction of particle displacement associated with the lobe while the arrows with varying size and direction in the spherical surface in b) indicate the variation of the transverse motions with θ and ϕ. P and T mark the penetration points of the pressure and tension axes, respectively, through the focal sphere. There are no nodal lines as in Fig. 3.25 but only nodal points where there is zero motion. The nodal point for transverse motion at $(\theta, \phi) = (45°, 0°)$ at T is a maximum in the pattern for longitudinal motion (see Fig.3.25) while the maximum transverse motion (e.g., at $\theta = 0$) occurs on a nodal line for the longitudinal motion. The pair of arrows in a) at the center denotes the shear dislocation (modified from Aki and Richards 1980; with kind permission of the authors).

In the case of a double-couple mechanism, according to Fig. 3.24, the S-wave amplitude pattern follows the relationship (see Aki and Richards, 1980)

$$\boldsymbol{A_S} = \cos 2\theta \cos\phi\,\boldsymbol{\theta} - \cos\theta \sin\phi\,\boldsymbol{\phi} \qquad (3.68)$$

with $\boldsymbol{\theta}$ and $\boldsymbol{\phi}$ - unit vectors in θ and ϕ direction, $\boldsymbol{A_S}$ - shear-wave displacement vector.

3.4.2 Manual determination of fault-plane solutions

Manually determined fault-plane solutions are normally based on P-wave polarity readings only which are plotted on two kinds of projections, either the equal-angle Wulff net or the Lambert-Schmidt equal area projection (Figs. 3.27a and b; see also Aki and Richards, 1980, Vol. 1, p. 109-110). The latter provides a less cluttered plot of data with take-off angles less than 45° but in principle the procedure of constructing the fault planes is the same (see EX 3.2 and EX 3.3).

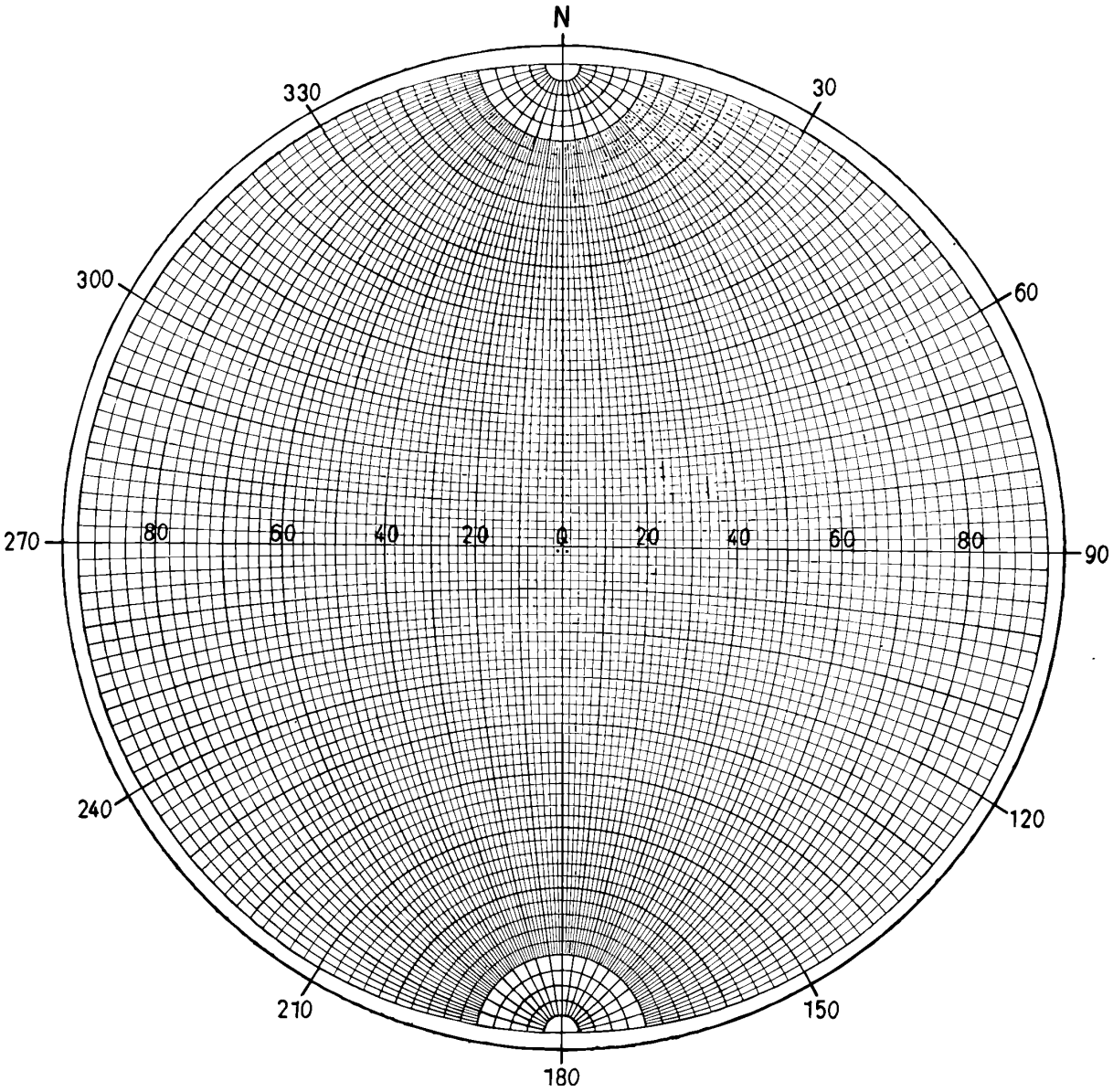

Fig. 3.27a The equal angle Wulff net. Note: Only the meridians are great circles!

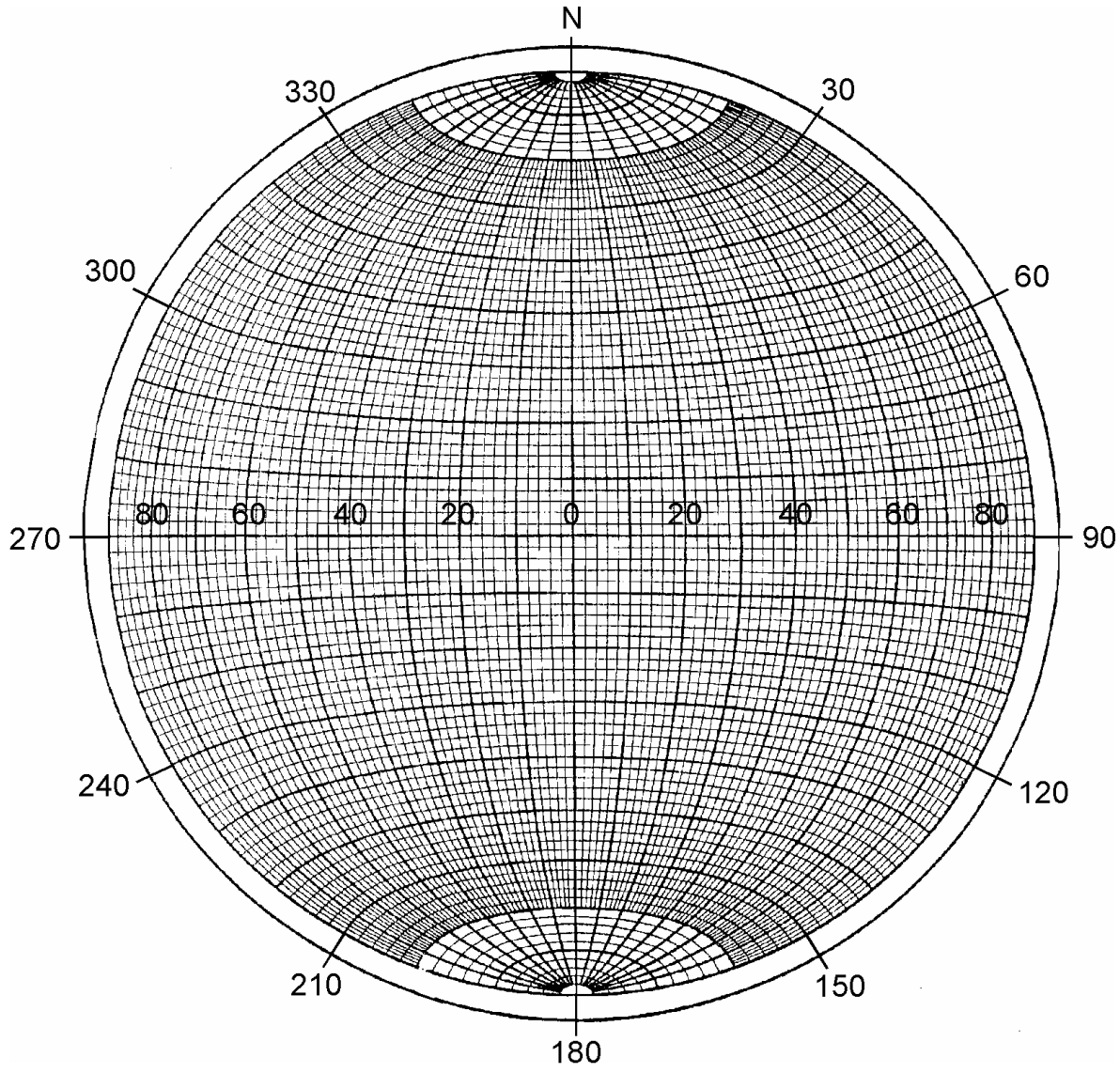

Fig. 3.27b The equal area Lambert-Schmidt net. Note: Only the meridians are great circles!

To obtain a fault-plane solution basically three steps are required:

(1) Calculating the positions of the penetration points of the seismic rays through the focal sphere which are defined by the ray azimuth AZM and the take-off (incidence) angle AIN of the ray from the source.
(2) Marking these penetration points through the upper or lower hemisphere in a horizontal projection of that sphere using different symbols for compressional and dilatational first arrivals. Usually, lower hemisphere projections are used. Rays which have left the upper hemisphere have to be transformed into their equivalent lower hemisphere ray. This is possible because of spherical symmetry of the radiation pattern (see Figs. 3.28 and 3.29).
(3) Partitioning the projection of the lower focal sphere by two perpendicular great circles which separate all (or at least most) of the + and - arrivals in different quadrants.

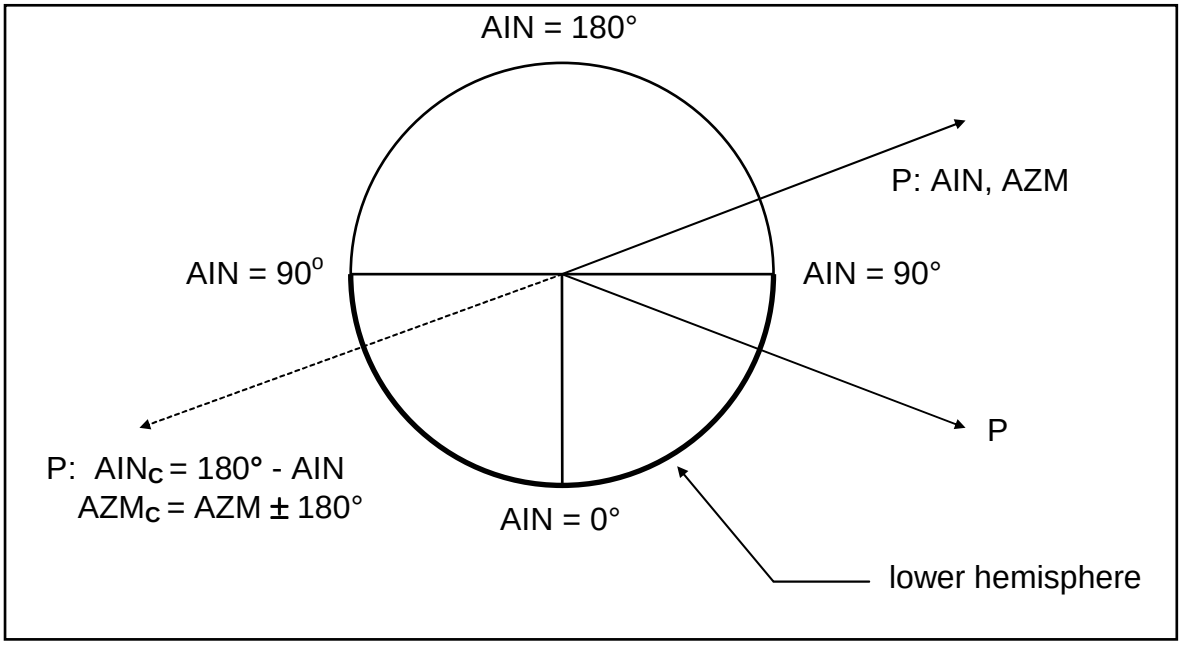

Fig. 3.28 Transformation of a ray leaving the focal sphere upwards with an incidence (take-off) angle AIN into an equivalent downward ray with same polarity and changed incidence angle AIN_c and azimuth AZM_c.

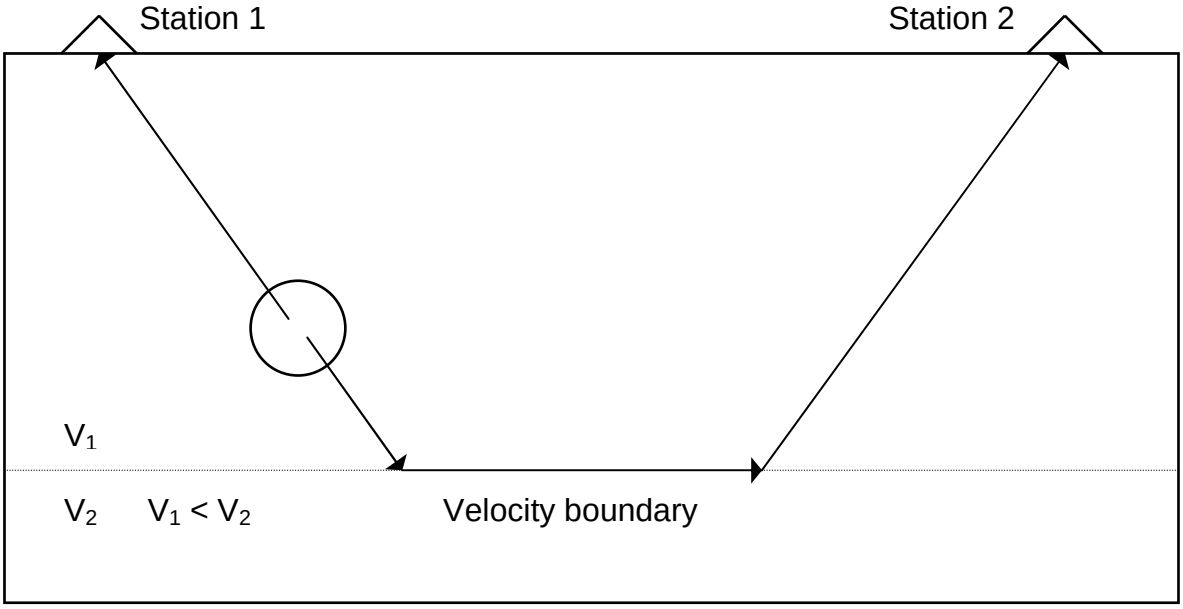

Fig. 3.29 Two rays, leaving the focal sphere in opposite directions, reach - because of the symmetry of radiation pattern - the stations 1 and 2 with the same polarity. The crossing point of the up-going ray with the focal sphere can, therefore, be remapped according to the formulas given in Fig. 3.28 into a crossing point with the lower hemisphere which coincides with the ray crossing-point for station 2.

Fig. 3.30 shows the angles which describe the orientation and motion of a fault plane and Fig. 3.31 shows their determination in the net projections. The **strike angle ϕ** is measured clockwise against North ($0° \le \phi \le 360°$). To resolve the 180° ambiguity, it is assumed that when looking into the strike direction the fault dips to the right hand side (i.e., its fault-trace projection is towards the right of the net center). The **dip angle δ** describes the inclination of the hanging wall against the horizontal ($0° \le \delta \le 90°$). The **rake angle λ** describes the displacement of the hanging wall relative to the foot wall ($-180° \le \lambda \le 180°$). $\lambda = 0$ corresponds to slip in strike direction, $\lambda > 0$ means upward motion of the hanging wall (i.e., *reverse or thrust faulting component*) and $\lambda < 0$ downward motion (i.e., *normal faulting component*).

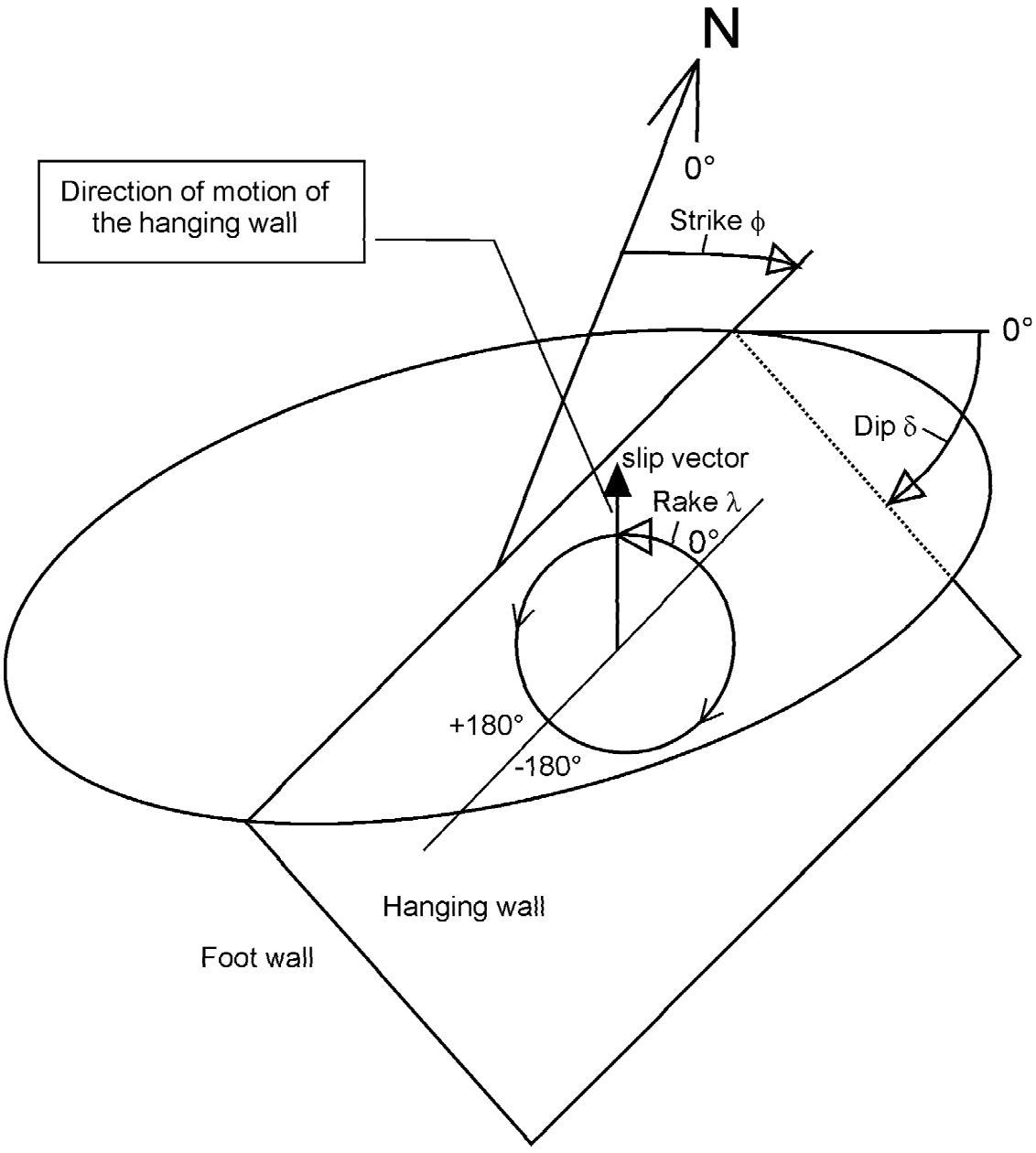

Fig. 3.30 Angles describing the orientation and motion of faults (see text).

In Fig. 3.31 P1, P2 and P3 mark the positions of the poles of the planes FP1 (fault plane), FP2 (auxiliary plane) and EP (equatorial plane) in their net projections. From Fig. 3.30 it is obvious that all three planes are perpendicular to each other (i.e., 90° apart) and intersect in the poles of the respective third plane, i.e., FP1 and FP2 in P3, FP1 and EP in P2 etc. Note that on the basis of polarity readings alone it can not be decided whether FP1 or FP2 was the active fault. Discrimination from seismological data alone is still possible but requires additional study of the *directivity effects* such as azimuthal variation of frequency (*Doppler* effect), amplitudes and/or waveforms. For sufficiently large shocks these effects can more easily be studied in low-frequency teleseismic recordings while in the local distance range, high-frequency waveforms and amplitudes may be strongly influenced by resonance effects due to low-velocity near-surface layers. Seismotectonic considerations or field evidence from surface rupture in case of strong shallow earthquakes may allow us to resolve this ambiguity, too. Figs. 3.32 and 3.33 depict several basic types of earthquake faulting and their related fault-plane solutions in so-called "beach-ball" presentations of the net projections.

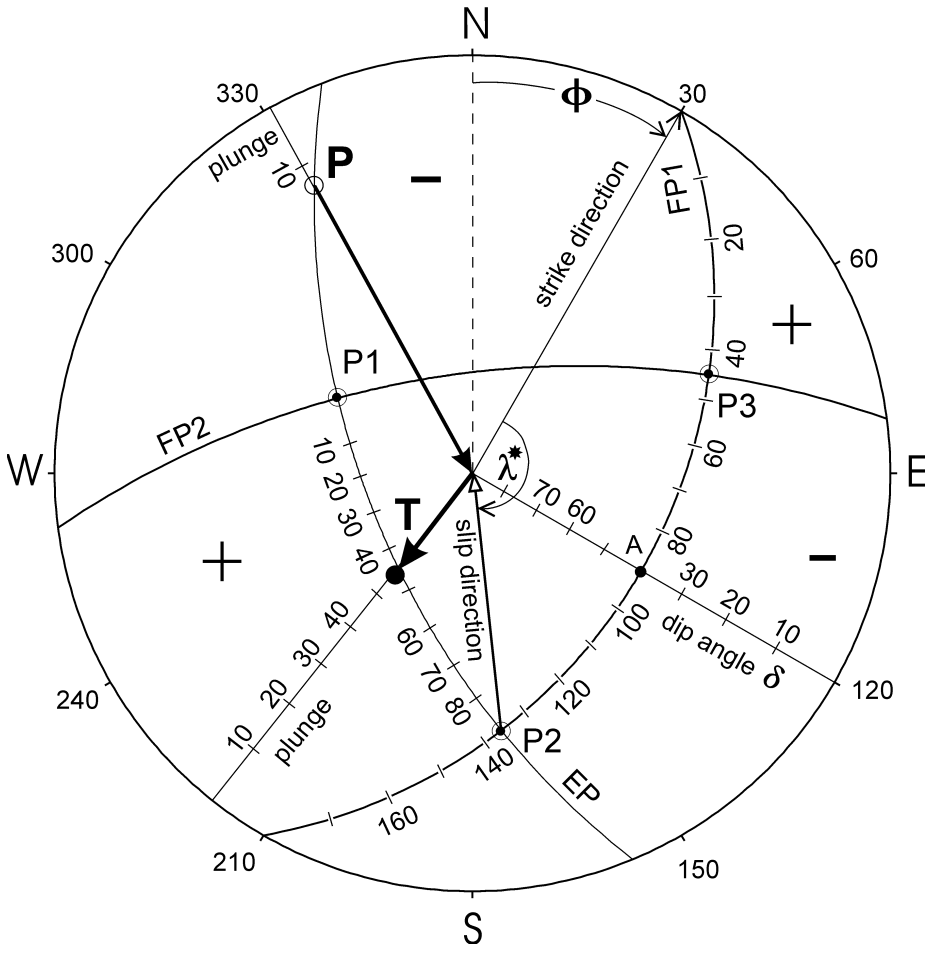

Fig. 3.31 Determination of the fault plane parameters ϕ, δ and λ in the net diagrams. The polarity distribution, slip direction and projection of FP1 shown qualitatively correspond to the faulting case depicted in Fig. 3.30. For abbreviations used see text. **Note:** $\lambda^* = 180° - \lambda$ when the center of the net lies in the tension (+) quadrant (i.e., event with thrust component) or $\lambda^* = -\lambda$ when the center of the net lies in the pressure quadrant (i.e., event with normal faulting component. P1, P2 and P3 are the poles (i.e., 90° off) of FP1, FP2 and EP, respectively. **P** and **T** are the penetration points (poles) of the pressure and tension axes, respectively, through the focal sphere. + and − signs mark the quadrants with compressional and dilatational P-wave first motions.

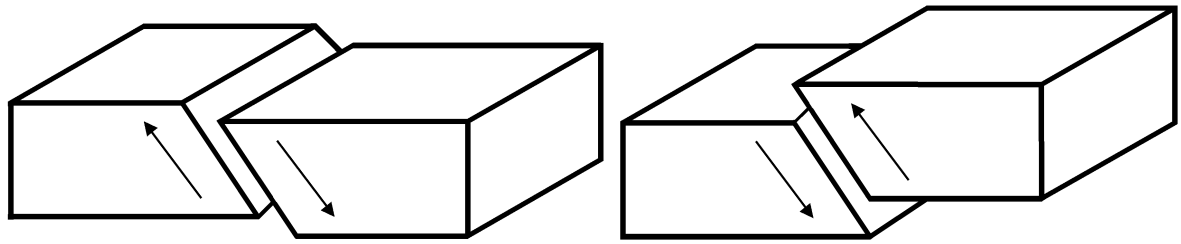

Pure normal faulting

dip $0^o < \delta < 90°$; rake = -90°

Pure thrust faulting

dip $0^o < \delta < 90°$; rake = +90°

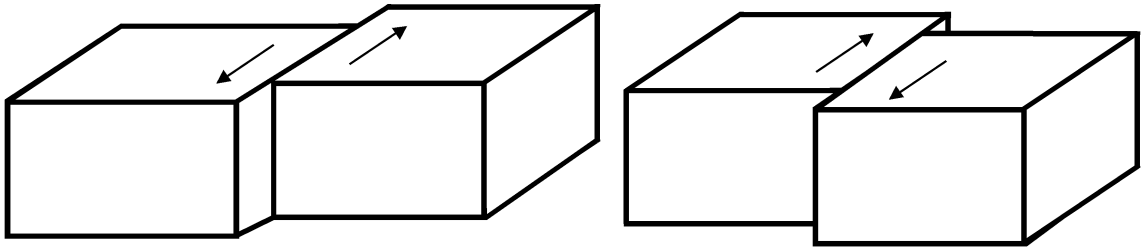

Pure strike slip
left lateral

Pure strike slip
right lateral

dip = 90° rake = 0° and 180°, respectively

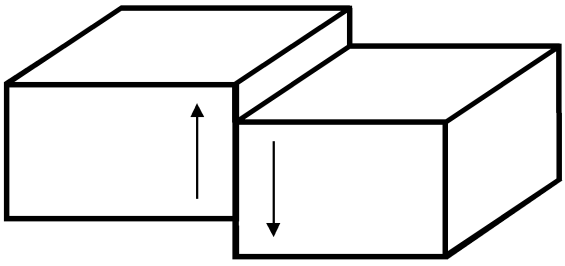

Down slip

dip = 90° rake = ± 90°

Fig. 3.32 Basic types of earthquake faulting for some selected dip and rake angles. Note that mixed types of faulting occur when $\lambda \neq 0$, 180^o or $\pm 90^o$, e.g., normal faulting with strike-slip component or strike-slip with thrust component. Also, dip angles may vary between $0^o < \delta \leq 90^o$. For fault plane traces and polarity distributions of these faulting types in their "beach-ball presentation" see Fig. 3.33.

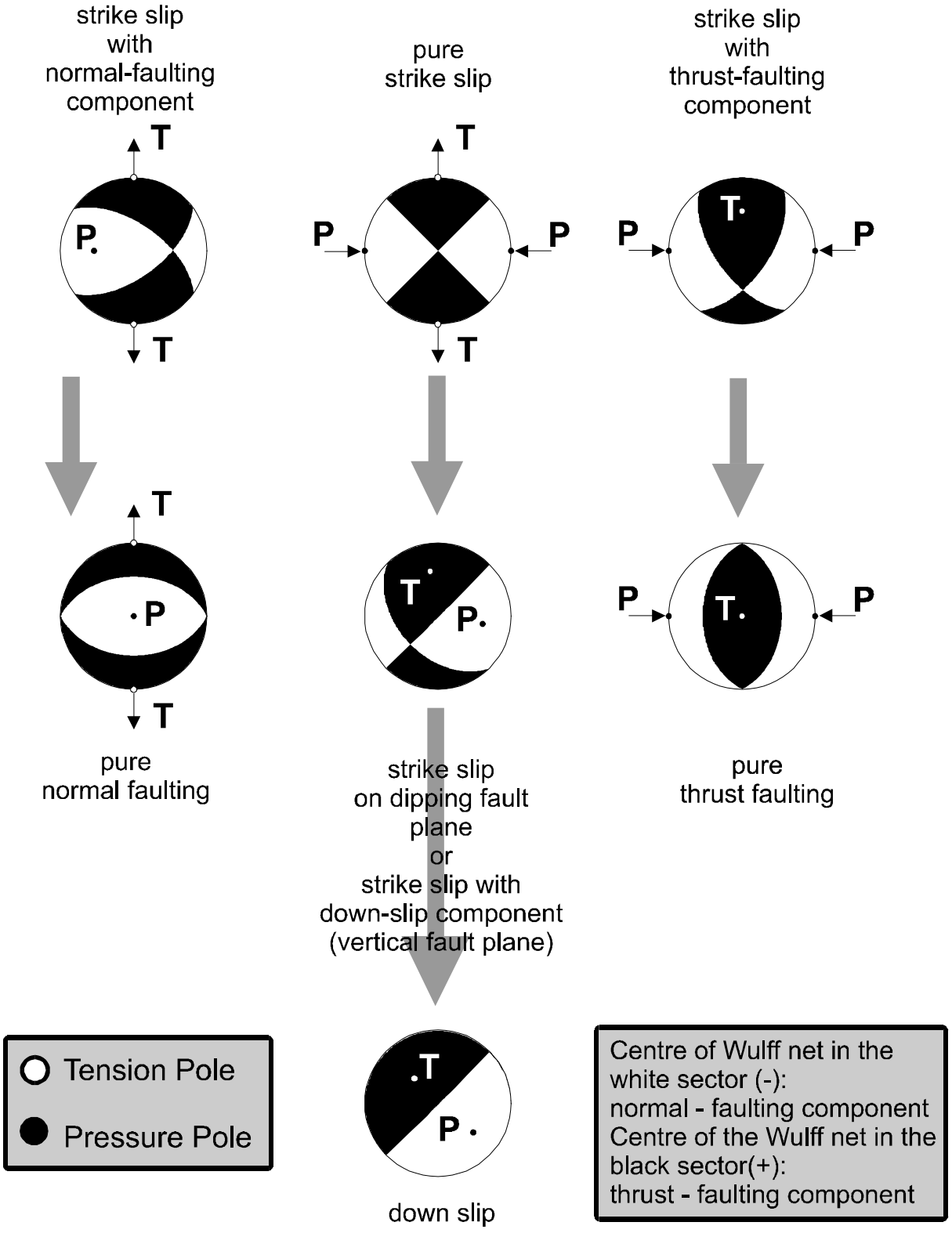

Fig. 3.33 "Beach-ball" presentation of the net projections of the fault plane cut-traces and of the penetration points (poles) of the P- and T-axes through the lower focal hemisphere for different faulting mechanisms. White sectors correspond to negative and black sectors to positive first-motion polarities.

3.4.3 Accuracy of fault-plane solutions

Fault planes determined by eye-fit to the polarity data may be uncertain by about $\pm 10^o$. This is acceptable. Even computer assisted best fits to the data will produce different acceptable solutions within about the same error range with only slightly different standard deviations (e.g., Figure 1 in EX 3.3, NEIC and HRVD solutions, respectively).

In addition, one has to be aware that different fitting algorithm or error-minimization procedures may produce different results within this range of uncertainty for the same data. A poor distribution of seismograph stations (resulting in insufficient polarity data for the net diagram), erroneous polarity readings and differences in model assumptions (e.g., in the velocity models used) may result in still larger deviations between the model solution and the actual fault planes. One should also be aware that the assumed constant angular (45^o) relationship between the fault plane on the one hand and the pressure and tension axis on the other hand is true in fact only in the case of a fresh rupture in a homogeneous isotropic medium. It may not be correct in the stress environment of real tectonic situations (i.e., P and $T \neq \sigma_1$ and $-\sigma_3$, respectively; see discussion in 3.1.2.4).

3.4.4 Computer-assisted fault-plane solutions

There exist quite a number of computer programs for the determination of both single and joint fault-plane solutions from first-motion data (e.g., Brillinger et al., 1980; Buforn and Udías, 1984; Udías and Buforn, 1988, and others referred to below). In most applications for local earthquakes homogeneous flat-layered velocity models are acceptable, i.e., layers with constant velocities and velocity discontinuities at the boundaries. The majority of location programs (e.g., HYPO71 by Lee and Lahr, 1975; HYPOELLIPSE by Lahr, 1989; HYPOINVERS by Klein, 1985) are based on this type of velocity model. Additionally, HYPOINVERS and HYPOELLIPSE do accept layers with linear velocity gradients. Moreover, HYPOELLIPSE may locate local events with predefined travel-time tables, too. During the location procedure the ray paths to the stations are calculated. The azimuth AZM and the take-off angle AIN at which the P wave, arriving at a given station, leaves the focal sphere are listed in the output files. The remaining problem to be solved is to find the distribution of P-polarities on the focal sphere and to estimate the angles describing the focal mechanism.

The computer program FPFIT (Reasenberger and Oppenheimer, 1985) calculates double-couple fault-plane solutions based on P-wave polarity readings. It accepts as input the output files of the localization programs HYPO71, HYPOELLIPSE and HYPOINVERSE. The inversion is accomplished through a grid-search procedure that finds the source model by *minimizing a normalized weighted sum of first-motion polarity discrepancies*. Two weighting factors are incorporated in the minimization. One of them reflects the estimated variance of the data while the other one is based on the absolute value of the P-wave radiation amplitude. In addition to the minimum-misfit solution, FPFIT finds alternative solutions corresponding to significant relative misfit minima. The existence of several minima may be due to insufficient number of polarity readings, localization errors, polarity misreadings or an inadequate velocity model (e.g., not modeled refractions) resulting in an incorrect position of the P-wave first-motion polarities on the focal sphere. One has also to be aware that it sometimes may happen that the seismometer component outputs have been wrongly plugged at a given station, resulting in systematically wrong polarity reportings by such a station. In

the case of models which perfectly fit the data, FPFIT applies an additional constraint. Its effect is to maximize the distance sum between the observation points and the nodal planes on the focal sphere. The display program FPPLOT shows the final fault-plane solution and the estimated uncertainty in terms of the range of possible orientations of the pressure and tension axes which is consistent with the data.

While the above programs accept only the output files of the hypocenter localization programs for local events, another widely used program package for seismogram analysis, SEISAN (Havskov, 1996; version 1.2 now available as CD-ROM from the International Seismological Centre in Thatcham, UK) uses a modified version of the program HYPOCENTER (Lienert et al., 1988; Lienert, 1991; Lienert and Havskov, 1995). The main modifications are that it can also accept secondary phases and locate teleseismic events. The output files are used in conjunction with the FOCMEC program (Snoke et al., 1984) for the determination of the fault plane parameters but currently on the basis of polarity readings only. The implementation of the additional use of S-P amplitude ratios is intended.

In the case of sparse networks or weak events, the number of polarity data may be too small for reliable estimation of fault-plane solutions. In this case P-, SV- and SH-amplitudes can be used in addition to polarities in order to get more stable and better constrained, i.e., less ambiguous fault-plane solutions. This is due to the difference in P-wave (Fig. 3.25) and S-wave (Fig. 3.26) polarity and angular amplitude pattern for a given source mechanism.

The program FOCMEC (Snoke, 1984) allows us to calculate best fitting double-couple fault-plane solutions from P, SH and SV polarities and/or SV/P, SH/P or SV/SH amplitude ratios provided that the ratios are corrected to the focal sphere by taking into account geometrical spreading, attenuation and free-surface effects. For surface correction the program FREESURF, which is supplied together with FOCMEC, can be used. The applied Q-model has to be specified according to the regional attenuation conditions or related corrections. When adopting a constant V_P/V_S velocity ratio, the geometrical spreading is the same for P and S waves and absolute changes in amplitude cancel each other in the above amplitude ratios. Head waves and amplitude changes at velocity boundaries require special treatment. The solution is obtained by grid search over strike, dip and slip of the double-couple source. The program FOCPLT, also provided together with FOCMEC, allows us to plot upper or lower hemisphere projections of the focal sphere and to show the data, i.e., the fault planes together with the poles of the pressure (P) and tension (T) axes for SH and SV waves. Note that S-wave amplitudes are zero in the direction of P and T.

While the program HYPO71 is available as part of Vol.1 of the IASPEI software library (Lee, 1995) the programs FOCMEC, FPFIT, HYPOELLIPSE and HYPOINVERSE are freely available through the Internet under the following addresses:

FOCMEC: http://www.iris.washington.edu or as for FPFIT
FPFIT: http://orfeus.knmi.nl/other.services/software.links.html#focalmech
HYPOELLIPSE: http://giseis.alaska.edu/pub/SOFTWARE/hypoel/
HYPOINVERSE: http://orfeus.knmi.nl/other.services/software.links.html#location

3.5 Source parameters and moment-tensor solutions (G. Bock ✞)

3.5.1 Introduction

The concept of first order *moment tensor* provides a complete description of equivalent body forces of a general seismic point source (see Fig. 3.34 in section 3.5.2). A source can be considered a point source if both the distance D of the observer from the source and the wavelength λ of the data are much greater than the linear dimension of the source. Thus, moment-tensor solutions are generally derived from low-frequency data and they are representative of the gross properties of the rupture process averaged over tens of seconds or more. The double-couple source model describes the special case of shear dislocation along a planar fault. This model has proven to be very effective in explaining the amplitude and polarity pattern of P, S and surface waves radiated by tectonic earthquakes. In the following, we briefly outline the relevant relations (in a first order approximation) between the moment tensor of a seismic source and the observed seismogram. The latter may be either the complete seismogram, one of its main groups (P, S or surface waves), or specific features of seismograms such as peak-to-peak amplitudes of body waves, amplitude ratios or spectral amplitudes. Then we outline a linear inversion scheme for obtaining the moment tensor using waveform data in the time domain. Finally, we will give an overview of some useful programs for moment-tensor analysis. Applications of moment-tensor inversions to the rapid (i.e., generally within 24 hours after the event) determination of source parameters after significant earthquakes will also be described.

3.5.2 Basic relations

Following Jost and Herrmann (1989), the displacement d on the Earth's surface at a station can be expressed, in case of a point source, as a linear combination of time-dependent moment-tensor elements M_{kj} ($\boldsymbol{\xi}$,t) that are assumed to have the same time dependence convolved (indicated by the star symbol) with the derivative G_{skj} (**x**,$\boldsymbol{\xi}$,t) of the Green's functions with regard to the spatial j-coordinate:

$$u_s(\mathbf{x},t) = M_{kj}(\xi,t) * G_{sk,j}(\mathbf{x},\xi,t)\,. \qquad (3.69)$$

u_s (**x**, t): s component of ground displacement at position x and time t
M_{kj} ($\boldsymbol{\xi}$,t): components of 2nd order, symmetrical seismic moment tensor M
G_{skj} (**x**,$\boldsymbol{\xi}$,t): derivative of the Green's function with regard to source coordinate ξ_j
x: position vector of station with coordinates x_1, x_2, x_3 for north, east and down
$\boldsymbol{\xi}$: position vector of point source with coordinates ξ_1, ξ_2, ξ_3 for north, east and down

Eq. (3.69) follows from the representation theorem in terms of the Green´s function (see Equations (21) and (38) in IS 3.1).The Green's function represents the impulse response of the medium between source and receiver and thus contains the various wave propagation effects through the medium from source to receiver. These include energy losses through reflection and transmission at seismic discontinuities, anelastic absorption and geometrical spreading. The M_{kj} ($\boldsymbol{\xi}$,t) from Eq.(3.69) completely describes the forces acting in the source and their time dependence. The Einstein summation notation is applied in Eq. (3.69) and below, i.e., the repeated indices k and j = 1, 2, 3 imply summation over x_1, x_2 and x_3. In Eq. (3.69) the higher order terms of the Taylor expansion around the source point of the Green's

functions $G_{sk,j}$ (**x**,ξ,t) have been neglected. Note that the source-time history s(t) (see 3.1, Figs. 3.4 and 3.7), which describes the time dependence of moment released at the source, is contained in c. If we assume that all the components of M_{kj} (ξ,t) have the same time dependence s(t) the equation can be written as:

$$u_s(\mathbf{x}, t) = M_{kj} \, [G_{sk,j}(\mathbf{x},\xi,t) * s(t)] \tag{3.70}$$

with s(t): source time history.

When determining M_{kj} (ξ,t) from seismic records, u_s(**x**, t) is calculated by convolution of the observed seismogram components y_s(**x**, t) with the inverse of the seismograph's displacement response function i(t):

$$u_s(\mathbf{x}, t) = y_s(\mathbf{x}, t) * \mathrm{Inv}\{i(t)\}$$

In the frequency domain (see Eq. (14) in IS 3.1) convolution is replaced by multiplication:

$$D_s(\mathbf{x}, \omega) = Y_s(\mathbf{x}, \omega) \, I(\omega)^{-1}$$

where ω is circular frequency. The D_s(**x**, ω), Y_s (**x**, ω), and $I(\omega)^{-1}$ are the respective Fourier transforms of the time series d_s(**x**, t), y_s(**x**, t), and $i(t)^{-1}$ (see 5.2.7 where $I(\omega)^{-1}$ is denoted as $H_d(\omega)^{-1}$).

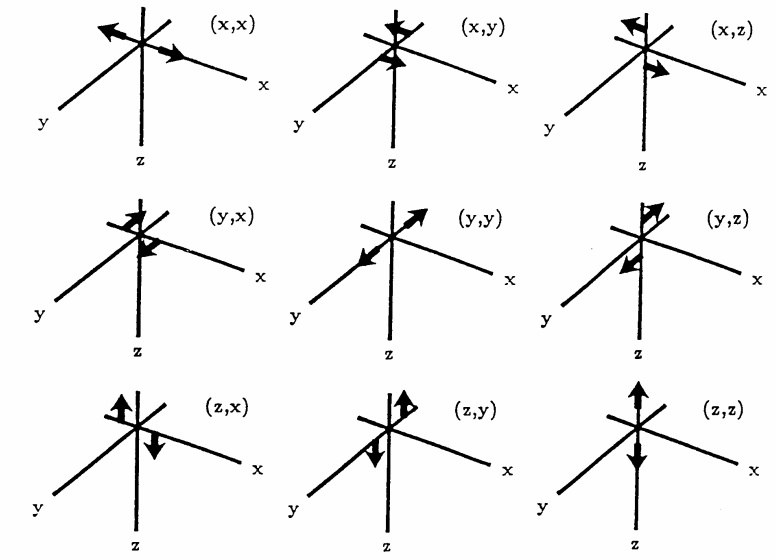

Fig. 3.34 The nine generalized couples representing $G_{sk,j}$(**x**, ξ, t) in Eq. (3.69). Note that force couples acting on the y axis in x direction or vice versa (i.e., (x,y) or (y,x)) will cause shear faulting in the x and y direction, respectively. Superimposition of vector dipoles in x and y direction with opposite sign, e.g., (x,x) + (-y,-y) will also cause shear faulting but 45° off the x and y direction, respectively. Both representations are equivalent (reproduced from Jost and Herrmann, A student's guide to and review of moment tensors. Seismol. Res. Lett., **60**, 2, 1989, Fig. 2, p. 39; ©Seismological Society of America).

In the following we assume that the source-time function s(t) is a delta function (i.e., a "needle" impulse). Then, $M_{kj}(\boldsymbol{\xi}, t) = M_{kj}(\boldsymbol{\xi})\cdot\delta(t)$, and the right side of Eq.(3.70) simplifies to $M_{kj}(\boldsymbol{\xi})\cdot G_{sk,j}(t)$. The seismogram recorded at x can be regarded as product of $G_{sk,j}$ and $M_{kj.}$ (e.g., Aki and Richards, 1980, Lay and Wallace, 1995; Udias, 1999). Thus, the derivative of G_{skj} with regard to the source coordinate ξ_i describes the response to a single couple with its lever arm pointing in the ξ_j direction (see Fig. 3.34). For k = j we obtain a vector dipole; these are the couples (x,x), (y,y), and (z,z) in Fig. 3.34. A double-couple source is characterized by a moment tensor where one eigenvalue of the moment tensor vanishes (equivalent to the Null or B axis), and the sum of eigenvalues vanishes, i.e., the trace of the moment tensor is zero. Physically, this is a representation of a shear dislocation source without any volume changes.

Using the notation of Fig. 3.32, double-couple displacement fields are represented by the sum of two couples such as (x,y)+(y,x), (x,x)+(y,y), (y,y)+(z,z), (y,z)+(z,y) etc. An explosion source (corresponding to M_6 in Eq. (3.76) and Fig. 3.34) can be modeled by the sum of three vector dipoles (x,x) + (y,y) + (z,z). A compensated linear vector dipole (CLVD, see 3.5.4 below) can be represented by a vector dipole of strength 2 and two vector dipoles of unit strength but opposite sign in the two orthogonal directions.

The seismic moment tensor **M** has, in general, six independent components which follows from the condition that the total angular momentum for the equivalent forces in the source must vanish. For vanishing trace, i.e., without volume change, we have five independent components that describe the deviatoric moment tensor. The double-couple source is a special case of the deviatoric moment tensor with the constraint that the determinant of **M** is zero, i.e., that the stress field is two-dimensional.

In general, **M** can be decomposed into an isotropic and a deviatoric part:

$$\mathbf{M} = \mathbf{M}^{\text{isotropic}} + \mathbf{M}^{\text{deviatoric}}. \tag{3.71}$$

The decomposition of **M** is unique while further decomposition of $\mathbf{M}^{\text{deviatoric}}$ is not. Commonly, $\mathbf{M}^{\text{deviatoric}}$ is decomposed into a double couple and CLVD:

$$\mathbf{M}^{\text{deviatoric}} = \mathbf{M}^{\text{DC}} + \mathbf{M}^{\text{CLVD}}. \tag{3.72}$$

For a double-couple source, the Cartesian components of the moment tensor can be expressed in terms of strike ϕ, dip δ and rake λ of the shear dislocation source (fault plane), and the scalar seismic moment M_0 (Aki and Richards, 1980):

$$\begin{aligned}
M_{xx} &= -M_0(\sin\delta\cos\lambda\sin2\phi + \sin2\delta\sin\lambda\sin^2\phi)\\
M_{xy} &= M_0(\sin\delta\cos\lambda\cos2\phi + 0.5\sin2\delta\sin\lambda\sin2\phi)\\
M_{xz} &= -M_0(\cos\delta\cos\lambda\cos\phi + \cos2\delta\sin\lambda\sin\phi)\\
M_{yy} &= M_0(\sin\delta\cos\lambda\sin2\phi - \sin2\delta\sin\lambda\cos^2\phi)\\
M_{yz} &= -M_0(\cos\delta\cos\lambda\sin\phi - \cos2\delta\sin\lambda\cos\phi)\\
M_{zz} &= M_0\sin2\delta\sin\lambda
\end{aligned} \tag{3.73}$$

As the tensor is always symmetric it can be rotated into a principal axis system such that all non-diagonal elements vanish and only the diagonal elements are non-zero. The diagonal elements are the *eigenvalues* (see Eq. (6) in Information Sheet 3.1) of **M**; the associated directions are the *eigenvectors* (i.e., the *principal axes*). A linear combination of the principal moment-tensor elements completely describes the radiation from a seismic source. In the case of a double-couple source, for example, the diagonal elements of **M** in the principal axis system have two non-zero eigenvalues M_0 and $-M_0$ (with M_0 the scalar seismic moment) whose eigenvectors give the direction at the source of the tensional (positive) T axis and compressional (negative) P axis, respectively, while the zero eigenvalue is in the direction of the B (or Null) axis of the double couple (for definition and determination of M_0 see Exercise 3.4).

Eq. (3.70) describes the relation between seismic displacement and moment tensor in the time domain. If the source-time function is not known or the assumption of time-independent moment-tensor elements is dropped, e.g., for reasons of source complexity, the frequency-domain approach is chosen:

$$u_s(\mathrm{x}, f) = M_{kj}(f) G_{sk,j}(\mathrm{x}, \xi, f) \tag{3.74}$$

where f denotes frequency. Procedures for the linear moment-tensor inversion can be designed in both the time and frequency domain using Eq. (3.70) or (3.74). We can write (3.70) or (3.74) in matrix form:

$$\mathbf{u} = \mathbf{G}\ \bar{m}. \tag{3.75}$$

In the time domain, the **u** is a vector containing n sampled values of observed ground displacement at various times, stations and sensor components, while **G** is a $6 \times n$ matrix and the vector $\bar{m}$ contains the six independent moment-tensor elements to be determined. In the frequency domain, **u** contains k complex values of the displacement spectra determined for a given frequency f at various stations and sensor components. G is a $6 \times$ k matrix and is generally complex like $\bar{m}$. For more details on the inversion problem in Eq. (3.75) the reader is referred to Chapter 6 in Lay and Wallace (1995), Chapter 12 in Aki and Richards (1980), or Chapter 19 of Udias (1999).

To invert Eq. (3.75) for the unknown $\bar{m}$, one has to calculate the derivatives of the Green's functions. The calculation of the Green's functions constitutes the most important part of any moment-tensor inversion scheme. A variety of methods exists to calculate synthetic seismograms (e.g., Müller, 1985; Doornbos, 1988; Kennett, 1988). Some of the synthetic seismogram codes allow calculations for the moment-tensor elements as input source while others allow input for double-couple and explosive point sources. The general moment tensor can be decomposed in various ways using moment-tensor elements of double-couple and explosive sources so that synthetic seismogram codes employing these source parameterizations can also be used in the inversion of (3.75).

3.5.3 An inversion scheme in the time domain

In this section, we will describe in short the moment-tensor inversion algorithm of Kikuchi and Kanamori(1991), where the moment tensor is decomposed into elementary double-couple sources and an explosive source. Adopting the notation used by Kikuchi and Kanamori(1991),

the moment tensor M_{kj} is represented by a linear combination of $N_e = 6$ elementary moment tensors M_n (Fig. 3.35):

$$M_{kj} = \sum_{n=1}^{N_e} a_n M_n \tag{3.76}$$

with

$$M_1 : \begin{bmatrix} 0 & 1 & 0 \\ 1 & 0 & 0 \\ 0 & 0 & 0 \end{bmatrix}; \quad M_2 : \begin{bmatrix} 1 & 0 & 0 \\ 0 & -1 & 0 \\ 0 & 0 & 0 \end{bmatrix}; \quad M_3 : \begin{bmatrix} 0 & 0 & 0 \\ 0 & 0 & 1 \\ 0 & 1 & 0 \end{bmatrix}$$

$$M_4 : \begin{bmatrix} 0 & 0 & 1 \\ 0 & 0 & 0 \\ 1 & 0 & 0 \end{bmatrix}; \; M_5 : \begin{bmatrix} -1 & 0 & 0 \\ 1 & 0 & 0 \\ 0 & 0 & 1 \end{bmatrix}; \quad M_6 : \begin{bmatrix} 1 & 0 & 0 \\ 0 & 1 & 0 \\ 0 & 0 & 1 \end{bmatrix}$$

The M_1 and M_2 represent pure strike-slip faults; M_3 and M_4 represent dip-slip faults on vertical planes striking N-S and E-W, respectively, and M_5 represents a 45° dip-slip fault. The M_6 represents an isotropic source radiating energy equally into all directions (i.e., an explosion).

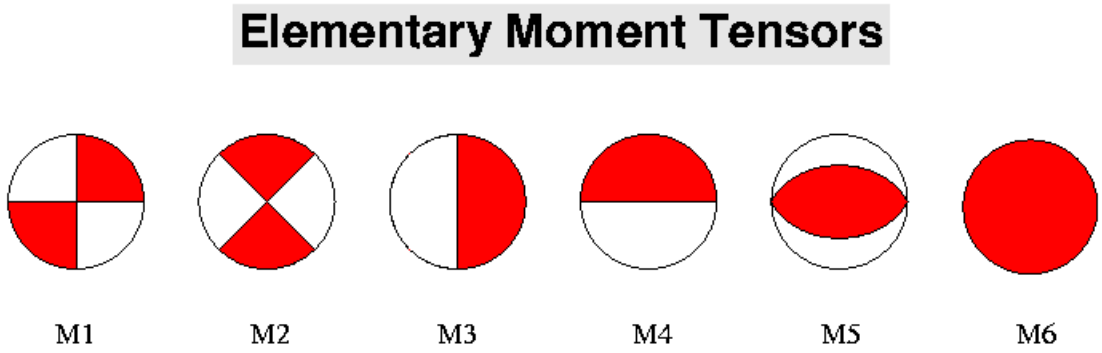

Fig. 3.35 Elementary moment tensors used in the inversion of the full moment tensor (after Kikuchi and Kanamori, 1991)

A pure deviatoric moment tensor (trace(M_{kj}) = 0) is entirely represented by the five elementary moment tensors M_1 to M_5. The following brief description of the linear inversion for the moment tensor (Kikuchi and Kanamori, 1991) is an example of an inversion performed in the time domain. It can be easily adopted for an inversion in the frequency domain by replacing the time series by their spectra. Let $w_{sn}(t)$ denote the Green's function derivative at station s in response to the elementary moment *tensor* M_n, and let $x_S(t)$ be the observed ground displacement as function of time at station *s*. The best estimate for the coefficients a_n in Eq. (3.76) can be obtained from the condition that the difference between observed and synthetic displacement functions be zero:

$$\Delta = \sum_{s=1}^{N_s} \int \left[x_s(t) - \sum_{n=1}^{N_e} a_n w_{sn}(t) \right]^2 dt$$

$$= R_x - 2\sum_{n=1}^{N_e} a_n G_n + \sum_{m=1}^{N_e} \sum_{n=1}^{N_e} R_{nm} a_n a_m$$

$$= Minimum \tag{3.77}$$

The N_e is the number of elementary moment tensors, and N_s is the number of displacement records used. The other terms in (3.77) are given by:

$$R_x = \sum_{s=1}^{N_S} \int [x_s(t)]^2 \, dt$$

$$R_{nm} = \sum_{s=1}^{N_S} \int [w_{sn}(t) w_{sm}(t)] \, dt$$

$$G_n = \sum_{s=1}^{N_S} \int [w_{sn}(t) x_s(t)] dt$$

Integration is carried out over selected portions of the waveforms. Evaluating $\partial\Delta/\partial a_n = 0$ for $n = 1,..., N_e$ yields the normal equations

$$\sum_{m=1}^{N_e} R_{nm} a_m = G_n \tag{3.78}$$

with n ranging from 1 to N_e. The solution for a_n is given by:

$$a_n = \sum_{m=1}^{N_e} R_{nm}^{-1} G_m \tag{3.79}$$

The inverse R_{nm}^{-1} of matrix R_{nm} can be obtained by the method of generalized least squares inversion (e.g., Pavlis, 1988). The resultant moment tensor is then given by

$$M_{kj} \begin{bmatrix} a_2 - a_5 + a_6 & a_1 & a_4 \\ a_1 & -a_2 + a_6 & a_3 \\ a_4 & a_3 & a_5 + a_6 \end{bmatrix} \tag{3.80}$$

The variance of the elements a_n can be calculated under the assumption that the data are statistically independent:

$$\mathrm{var}(a_n) = \sum_{m=1}^{N_e} (R_{nm}^{-1})^2 \sigma_m^2$$

where σ_m^2 is the variance of the data G_n. In the case where the variance of the data is not known, $\sum_{m=1}^{N_e} (R_{nm}^{-1})^2$ can be used as relative measure for the uncertainty.

3.5.4 Decomposition of the moment tensor

Except for the volumetric and deviatoric components, the decomposition of the moment tensor is not unique. Useful computer programs for decomposition were written by Jost and distributed in Volume VIII of the Computer Programs in Seismology by Herrmann of Saint Louis University (http://www.eas.slu.edu/People/RBHerrmann/ComputerPrograms.html or e-mail to R. W. Herrmann: rbh@slueas.slu.edu). The first step in the decomposition is the calculation of eigenvalues and eigenvectors of the seismic moment tensor. For this the program *mteig* can be used. It performs rotation of the moment tensor **M** into the principal axis system. The eigenvector of the largest eigenvalue gives the T (or tensional) axis; the eigenvector of the smallest eigenvalue gives the direction of the P (or compressional) axis, while the eigenvector associated with the intermediate eigenvalue gives the direction of the Null axis. The output of *mteig* is the diagonalized moment tensor

$$M = \begin{bmatrix} m_1 & 0 & 0 \\ 0 & m_2 & 0 \\ 0 & 0 & m_3 \end{bmatrix} \tag{3.81}$$

whose elements are input to another program, *mtdec*, which performs a moment-tensor decomposition. First, the moment tensor is decomposed into an isotropic and a deviatoric part (see Eq. 3.71):

$$M = \frac{1}{3}\begin{bmatrix} tr(M) & 0 & 0 \\ 0 & tr(M) & 0 \\ 0 & 0 & tr(M) \end{bmatrix} + \begin{bmatrix} m_1^1 & 0 & 0 \\ 0 & m_2^1 & 0 \\ 0 & 0 & m_3^1 \end{bmatrix} \tag{3.82}$$

with $tr(\mathbf{M}) = m_1 + m_2 + m_3$ being the trace of **M**. The isotropic part of **M** is important in quantifying volume changes of the source, but it is usually difficult to resolve so that isotropic parts of less than 10% are often not considered to be significant. The deviatoric part of the moment tensor can be further decomposed. Options include decompositions into three vector dipoles, into three double couples, into 3 CLVD sources, into a major and minor double couple, and into a best double couple and a CLVD having the same principal a**x**is system. The source mechanisms reported by Harvard and USGS are based on the decomposition of the moment tensor into a best double couple and a CLVD. In addition to the best double couple they also provide the moment-tensor elements. To estimate the double-couple contribution to the deviatoric moment tensor, the parameter

$$\varepsilon = \frac{|m_{\min}|}{|m_{\max}|}$$

is used (Dziewonski et al., 1981) where m_{min} and m_{max} are the smallest and largest eigenvalues of the deviatoric part of **M**, respectively, both in absolute terms. For a pure double-couple source, ε = 0 because m_{min} = 0; for a pure CLVD, ε = 0.5. The percentage double-couple contribution can be expressed as (1-2ε)×100. Significant CLVD components are often reported for large intermediate-depth and very deep earthquakes. In many cases, however, it can be shown that these are caused by superposition of several rupture events with different double-couple mechanisms (Kuge and Kawakatsu, 1990; Frohlich, 1995; Tibi et al., 1999).

Harvard and USGS publish the moment tensors using the notation of normal mode theory. It is based on spherical co-ordinates (r;Θ;Φ) where r is the radial distance of the source from the center of the Earth, Θ is co-latitude, and Φ is longitude of the point source. The 6 independent moment-tensor elements in the (x, y, z) = (north, east, down) coordinate system are related to the components in (r;Θ;Φ) by

$$M_{rr} = M_{zz}$$

$$M_{\Theta\Theta} = M_{xx}$$

$$M_{\Phi\Phi} = M_{yy}$$

$$M_{r\Theta} = M_{zx}$$

$$M_{r\Phi} = -M_{zy}$$

$$M_{\Theta\Phi} = -M_{xy}$$

3.5.5 Steps taken in moment-tensor inversion

Generally, the quality of moment-tensor inversion depends to a large extent on the number of data available and the azimuthal distribution of stations about the source. Dufumier (1996) gives a systematic overview for the effects caused by differences in the azimuthal coverage and the effects caused due to the use of only P waves, P plus SH waves or P and SH and SV waves for the inversion with body waves.

A systematic overview with respect to the effects caused by an erroneous velocity model for the Green function calculation and the effects due to wrong hypocenter coordinates can be found in Šílený et al. (1992), Šílený and Pšenčik (1995), Šílený et al. (1996) and Kravanja et al. (1999).

The following is a general outline of the various steps to be taken in a moment-tensor inversion using waveform data:

1) Data acquisition and pre-processing
   - good signal-to-noise ratio
   - unclipped signals

- good azimuthal coverage
- removing mean value and linear trends
- correcting for instrument response, converting seismograms to displacement

low-pass filtering to remove high-frequency noise and to satisfy the point source approximation

2) Calculation of synthetic Green's functions dependent on
- Earth model
- location of the source
- receiver position

3) Inversion
- selection of waveforms, e.g., P, S H or full seismograms
- taking care to match waveforms with corresponding synthetics
- evaluation of Eqs. (3.76) and (3.77)
- decomposition of moment tensor, e.g., into best double couple plus CLVD

The inversion may be done in the time domain or frequency domain. Care must be taken to match the synthetic and observed seismograms. Alignment of observed and synthetic waveforms is facilitated by cross-correlation techniques. In most moment-tensor inversion schemes, focal depth is assumed to be constant. The inversion is done for a range of focal depths and as best solution one takes that with the minimum variance of the estimate.

3.5.6 Some methods of moment-tensor inversion

3.5.6.1 NEIC fast moment tensors

This is an effort by the U.S. National Earthquake Information Center (NEIC) in co-operation with the IRIS Data Management Center to produce rapid estimates of the seismic moment tensor for earthquakes with body-wave magnitudes ≥ 5.8. Digital waveform data are quickly retrieved from “open" IRIS stations and transmitted to NEIC by Internet. These data contain teleseismic P waveforms that are used to compute a seismic moment tensor using a technique based on optimal filter design (Sipkin, 1982). The solution is then disseminated by e-mail to a list of subscribers. To register send a request by e-mail to sipkin@usgs.gov. More information is available under http://gldss7.cr.usgs.gov/neis/FM/fast_moment.html.

3.5.6.2 Harvard CMT solutions

The Harvard group maintains an extensive catalog of centroid moment-tensor (CMT) solutions for strong (mainly M > 5.5) earthquakes over the period from 1976 till present. Their solutions, as well as quick CMT solutions of recent events, can be viewed at http://www.seismology.harvard.edu/projects/CMT/. The Harvard CMT method makes use of both very long-period (T > 40 s) body waves (from the P wave onset until the onset of the fundamental modes) and so-called mantle waves at T > 135 s that comprise the complete surface-wave train.

Besides the moment tensor the iterative inversion procedure seeks a solution for the best point source location of the earthquake. This is the point where the system of couples is located in the source model described by the moment tensor. It represents the integral of the moment density over the extended rupture area. This centroid location may, for very large earthquakes,

significantly differ from the hypocenter location based on arrival times of the first P-wave onsets. The hypocenter location corresponds to the place where rupture started. Therefore, the offset of the centroid location relative to the hypocentral location gives a first indication on fault extent and rupture directivity. In case of the August 17, 1999 Izmit (Turkey) earthquake the centroid was located about 50 km east of the "P-wave" hypocenter. The centroid location coincided with the area where the maximum surface ruptures were observed.

3.5.6.3 EMSC rapid source parameter determinations

This is an initiative of the European-Mediterranean Seismological Center (Bruyeres-le-Chatel, France, http://www.emsc-csem.org/) and the GEOFON Programs at the GeoForschungs-Zentrum Potsdam (http://www.gfz-potsdam.de/geofon/). The EMSC method uses a grid search algorithm to derive the fault-plane solutions and seismic moments of earthquakes (M > 5.5) in the European- Mediterranean area. Solutions are derived within 24 hours after the occurrence of the event. The data used are P- and S-wave amplitudes and polarities. Fig. 3.36 shows an example of the kind of output data produced. More information can be obtained through http://www.gfz-potsdam.de/pb2/pb24/emsc/emsc.html.

3.5.6.4 Relative moment-tensor inversion

Especially for the inversion of local events so called relative moment-tensor inversion schemes have been developed (Oncescu, 1986; Dahm, 1996). If the sources are separated by not more than a wavelength, the Green's functions can be assumed to be equal with negligible error. In this case it is easy to construct a linear equation system that relates the moment-tensor components of a reference event to those of another nearby event. This avoids the calculation of high-frequency Green's functions necessary for small local events and all problems connected with that (especially the necessity of modeling site transfer functions in detail).

This is a very useful scheme for the analysis of aftershocks if a well determined moment tensor of the main shock is known. Moreover, if enough events with at least slightly different mechanisms and enough recordings are available, it is also possible to eliminate the reference mechanism from the equations (Dahm, 1996). This is interesting for volcanic areas where events are swarm-like and of similar magnitude, and where a reference moment tensor can not be provided (Dahm and Brandsdottir, 1997).

3.5.6.5 NEIC broadband depths and fault-plane solutions

Moment-tensor solutions, which are generally derived from low-frequency data, reflect the gross properties of the rupture process averaged over tens of seconds or more. These solutions may differ from solutions derived from high frequency data, which are more sensitive to the dynamic part of the rupture process during which most of the seismic energy is radiated. For this reason, beginning January 1996, the NEIC has determined, whenever possible, a fault plane solution and depth from broadband body waves for any earthquake having a magnitude greater than about 5.8 and it has published the source parameters in the Monthly Listings of the PDE. The broadband waveforms that are used have a flat displacement response over the frequency range 0.01-5.0 Hz. (This bandwidth, incidentally, is also commensurate with that

used by the NEIC to compute teleseismic E_S.) Initial constraints on focal mechanism are provided by polarities from P, pP and PKP waves, as well as by Hilbert-transformed body waves of certain secondary arrivals (e.g., PP), and from transversely polarized S waves. The fault-plane solution and depth are then refined by least-squares fitting of synthetic waveforms to teleseismically recorded P-wave groups (consisting of direct P, pP and sP). More information can be found under http://neic.usgs.gov/neis/nrg/bb_processing.html.

European-Mediterranean Seismological Centre
Centre Sismologique Euro-Mediterraneen

Double-couple solution provided by GFZ Potsdam

EMSC event parameters: 21-JUN-2000_00:51:46.6
63.88 N 20.69 W (Iceland)
Depth = 10 km (adopted in inversion)
Depth = 9 km (based on 32 depth phases)

32 stations used in inversion:

Station	Delta	Azimuth	Takeoff	Polarity
adk	63.06	343.55	20.3	C
aqu	29.12	121.60	27.6	C
biny	38.06	262.06	26.1	x
brg	22.41	109.49	33.8	C
cart	28.87	146.49	27.7	C
cmb	60.57	296.59	20.9	C
cmla	26.31	188.62	28.2	D
cor	56.07	302.72	22.0	C
css	43.52	105.32	24.9	C
dug	55.68	291.95	22.1	C
eil	48.77	107.33	23.7	C
ffc	39.71	296.00	25.8	C
furi	68.86	114.32	19.0	C
hgn	19.27	120.81	34.9	C
incn	75.70	26.33	17.4	D
kev	19.21	51.83	34.9	D
kmbo	77.57	119.84	17.0	C
kbs	17.85	20.07	40.1	D
kwp	27.08	101.36	28.0	C
morc	24.75	106.92	28.4	C
mrni	46.08	104.64	24.3	C
mte	24.76	155.63	28.4	C
pas	63.05	292.64	20.3	C
pet	58.94	331.77	21.3	C
rgn	19.51	103.10	34.8	C
selv	28.58	151.01	27.7	C
sfuc	28.62	155.24	27.7	C
sjg	55.09	235.67	22.2	D
sspa	40.16	262.47	25.7	D
suw	24.19	93.73	28.5	C
tns	20.68	118.00	34.5	C
tuc	61.55	285.54	20.7	C

Data provided by:
IRIS/USGS, MedNet, USNSN, GRSN, UCM/SFO/GEOFON, IRIS/IDA, GEOFON, GII/GEOFON, KNMI, IRIS/GEOFON, IRIS/AWI/GEOFON, TERASCOPE, GRSN/GEOFON, IAG, GTSN, U. Arizona

Corner frequencies of bandpass filter: 0.020 and 0.100 Hz

First fault plane: Strike = 358 degrees
Rake = 185 degrees
Dip = 85 degrees

Second fault plane: Strike = 268 degrees
Rake = -5 degrees
Dip = 85 degrees

M_0 = (4.3 +/- 2.1)*10**18 N*m
Mw = 6.4

Source duration = 4 s (from BB displacement seismograms)

Principal axes	Trend	Plunge
P	223	7
N	43	83
T	313	0

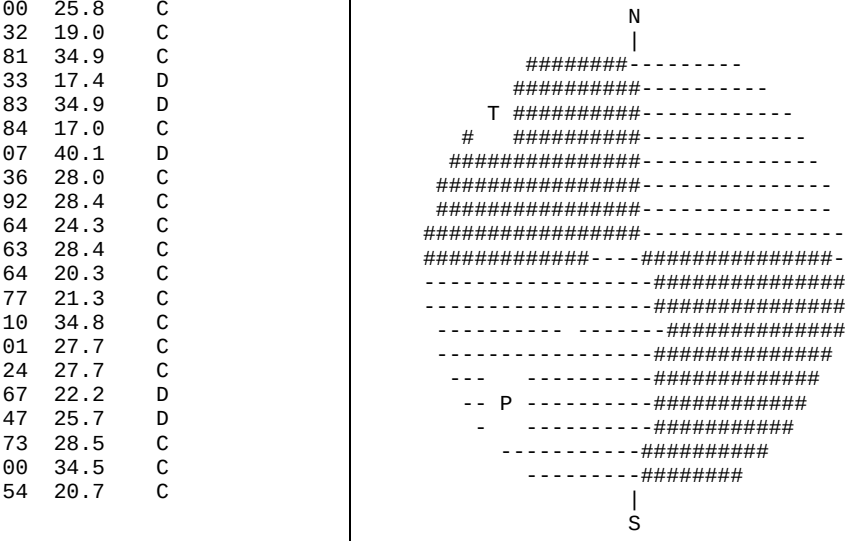

Done by G. Bock, GeoForschungsZentrum Potsdam.
Visit the GFZ-EMSC web page under http://www.gfz-potsdam.de/pb2/pb24/emsc/emsc.html

Fig. 3.36 Example of output data produced by the routine procedure for rapid EMSC source parameter determinations by the GEOFON group at the GFZ Potsdam.

3.6 Seismic scaling relations (P. Bormann)

3.6.1 Definition and use of seismic scaling relations

Empirical formulas relate one measured or calculated parameter to another. We have encountered such relationships in our discussions of seismic moment, energy and magnitude. Relations can also be found between other physical or geometrical parameters of earthquake size such as intensity, stress drop, duration of rupture, area or length of rupture, fault dislocation, area of felt shaking, etc. If any of these parameters appear to be related in a systematic and predictable manner over a wide range of earthquake size, scaling "laws" and similarity conditions may be inferred. These seismic scaling laws and similarity conditions allow the rough estimation of one parameter from another (e.g., E_S from M_0 or magnitude, or M_0 from field evidence such as surface rupture length and/or displacement). Therefore, the knowledge of theoretically well founded scaling laws or empirical scaling relationships is of crucial importance for both probabilistic and deterministic seismic hazard analyses. They aim at assessing the future earthquake potential of a region on the basis of data from past events, dating back as far as possible. Scaling laws are often the only way to estimate parameters of historical earthquakes which often lack instrumental measurements of magnitude, seismic energy or moment. Specifically, one often has to make reasonable estimates of the size of the largest earthquake that might have occurred at or could be generated by a particular fault or fault segment and of the kind of seismic spectrum it might (have) radiate(d). However, one has to be aware that seismic sources differ not only in their geometrical size and average slip. Ambient stress conditions, the dominant modes of faulting, ranges of stress drop and related seismic source spectra may also differ significantly from region to region. For instance, events of the same seismic moment may release seismic energies which differ by 2 to 3 orders. Therefore, the globally-derived scaling relations may not be appropriate for use for some areas. Regional scaling laws should be used, therefore, whenever available, particularly when inferences have to be drawn on regional seismic strain rates or on seismic hazard, the latter being mainly controlled by the frequency of occurrence and the potential of earthquakes to generate strong high-frequent motions.

3.6.2 Energy-magnitude-moment relations

Gutenberg and Richter (1956a) gave the following relationship between seismic energy E_S (in Joule ; 1 J = 10^7 erg) and the so-called unified magnitude m which is related to mB (see 3.2.5.2):

$$\log E_S = 2.4\ m - 1.2. \qquad (3.83)$$

Eq. (3.83) is supposed to have minimum of observation errors and yields, together with the relationship mB = 2.5 + 0.63 Ms in the same publication,

$$\log E_S = 1.5\ Ms + 4.8. \qquad (3.84)$$

After many revisions, Gutenberg and Richter (1956c) finally published Eq. (3.84) which is now most widely applied. It was also used by Kanamori (1977) in developing the seismic *moment magnitude* Mw (see 3.2.5.3). Recently, Choy and Boatwright (1995) found (see 3.3)

$$\log E_S = 1.5\ Ms + 4.4. \qquad (3.85)$$

From theoretical considerations Randall (1973) derived a relationship between E_S and the local magnitude Ml which was later confirmed empirically by Seidl and Berckhemer (1982) as well as by Berckhemer and Lindenfeld (1986). On the basis of direct energy calculations for earthquakes from the Friuli region, Italy, using digital broadband records of the Gräfenberg array in Germany, the latter obtained:

$$\log E_S \sim 2.0\ Ml. \tag{3.86}$$

This is close to the empirical findings by Gutenberg and Richter (1956a) ($\log E_S \sim 1.92$ Ml) for southern California and the more recent one by Kanamori et al.(1993). The latter got

$$\log E_S = 1.96\ Ml + 2.05 \tag{3.87}$$

for the magnitude range $1.5 < Ml < 6.0$. For $Ml > 6.5$ Ml saturates.

For short-period body-wave magnitudes mb Sadovsky et al. (1986) found the relationship

$$\log E_S = 1.7\ mb + 2.3 \tag{3.88}$$

which is applicable for both earthquakes and underground explosions. **Note:** According to the coefficient in the above equations one unit of magnitude increase in Ms, mb, Ml and mB, respectively, corresponds to an increase of E_S by a factor of about 32, 50, 100 and 250 times!

In this context one should mention that in the countries of the former USSR the energy scale after Rautian (1960), $K = \log E_S$ (with E_S in J), is widely used and given in the catalogs. It is based on the same elements as any other magnitude scale such as an empirical calibration function and a reference distance (here 10 km). K relates to magnitude M via

$$K = 1.8\ M + 4. \tag{3.89}$$

Riznichenko (1992) summarized data and relationships published by many authors (see Fig. 3.37) between magnitude M and K on the one hand and $\log M_0$ on the other hand. Depending on the range of distance and size M stands here for Ml, mb, mB or Ms.

Kanamori (1983) published linear relationships between $\log E_S$ and $\log M_0$ for both shallow and intermediate to deep events (see Fig. 3.38). They are rather similar and correspond, on average, to the relationship $E_S/M_0 = 5 \times 10^{-5}$ which he used in the development of the moment magnitude scale Mw (Kanamori 1977).

However, as previously mentioned in the sub-sections 3.2.5.3 and 3.2.6.1 on moment and energy magnitudes, scaling laws must be used with caution. Later investigations have revealed sometimes significant deviations from this average E_S/M_0 - relationship (e.g., Kikuchi and Fukao, 1988; Choy and Boatwright, 1995). This is due to local and regional differences in source mechanism, stress drop, time history of the rupture process, etc. It makes global relationships of this type often unsuitable for drawing inferences on regional differences in tectonic deformation and stress accumulation rates. Furthermore, scaling laws for source parameters derived from low-frequency data may not be suitable for inferring seismic hazard, which is affected by the high frequencies that cause most earthquake damage and are more relevant for earthquake engineers.

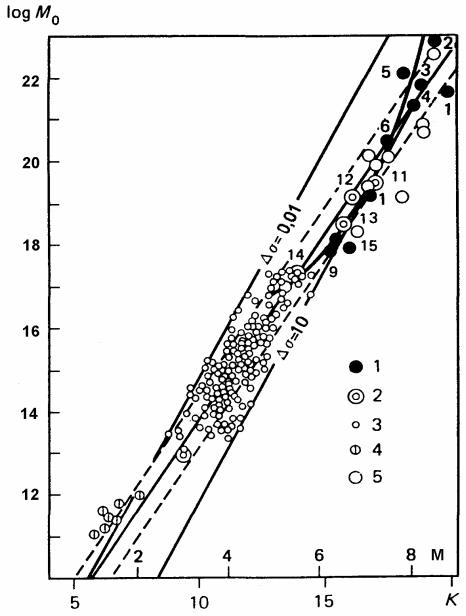

Fig. 3.37 Correlation between seismic moment M_0 (in Nm = J), magnitude M and Rautian´s (1960) energetic class K according to a compilation of data from many authors. Related stress drop $\Delta\sigma$ has been given in MPa (full straight lines). Broken lines mark the 68% confidence interval. 1 - large global earthquakes; 2 - average values for individual regions; 3 -earthquakes in the western USA; 4 - micro-earthquakes in Nevada; 5 - M_0 determinations from field data; 6 to 15 - individual values from different regions (modified from Riznichenko, 1992, Fig. 1; with permission from Springer-Verlag).

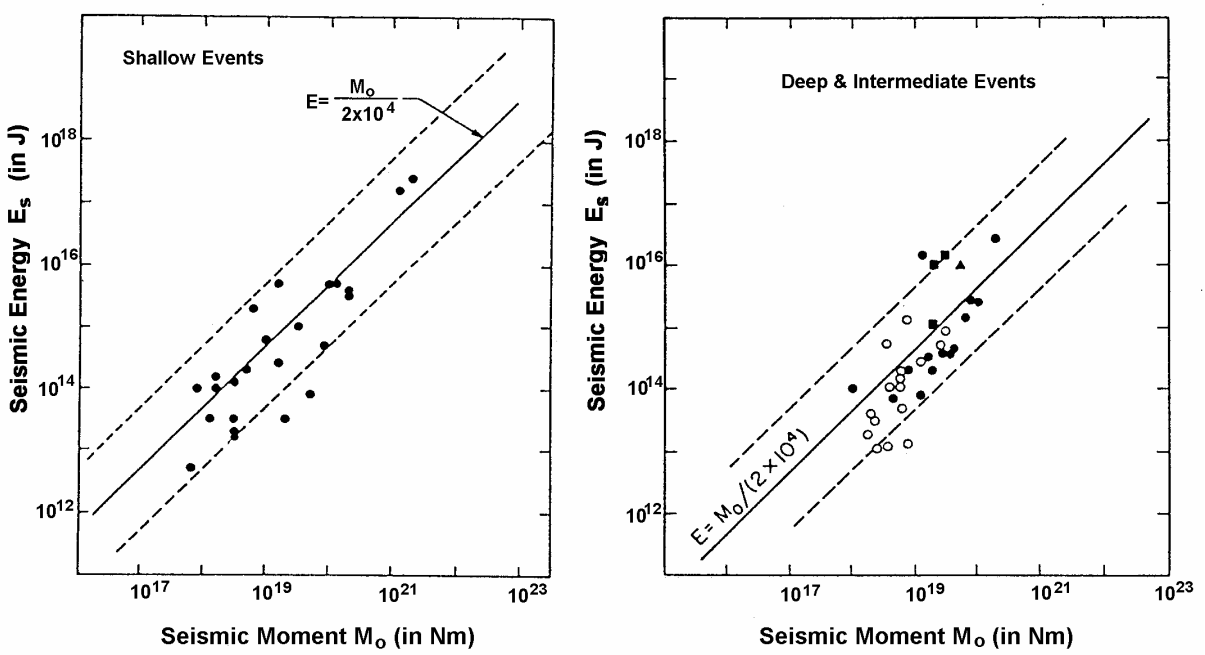

Fig. 3.38 Relations between seismic moment M_0 and energy E_S for shallow events (left) and intermediate to deep events (right) according to Vassiliou and Kanamori (1982). The solid line indicates the relation $E_S = M_0 /(2\times10^4)$ suggested by Kanamori (1977) on the basis of elastostatic considerations (modified from Kanamori, 1983 in Tectonophysics, Vol. 93, p. 191 and 192, with permission from Elsevier Science).

3.6.3 Moment-magnitude relations

Global relations between Ms and M_0 were derived by Ekström and Dziewonski (1988) from high quality determinations of M_0 from the Global Digital Seismic Network (GDSN). M_0 is given below in Nm (1 Nm = 1 J = 10^7 dyn cm = 10^7 ergs):

$\log M_0 = Ms + 12.24$ for $Ms < 5.3$, (3.90)

$\log M_0 = 23.20 - (92.45 - 11.40Ms)^{1/2}$ for $5.3 \leq Ms \leq 6.8$, (3.91)

$\log M_0 = 1.5\ Ms + 9.14$ for $Ms > 6.8$. (3.92)

Chen and Chen (1989) published detailed global relations between M_0 and Ms, as well as between mb and Ml, based on data for about 800 earthquakes in the magnitude range $0 < M < 8.6$. These authors also showed that their empirical data are well fit by theoretical scaling relations derived from a modified Haskell model of a rectangular fault which produces displacement spectra with three corner frequencies. Similar global scaling relations had been derived earlier by Gellert (1976), also based on the Haskell (1964 and 1966) model. In both papers these relations show saturation for Ml at about 6.3, for mb between about 6.0 and 6.5 and for Ms between about 8.2 and 8.5.

Other global relationships between M_0 and M_S were derived from Chen and Chen (1989) from a theoretical scaling law based on a modified Haskell source model. They fit well a set of global data with a standard deviation of individual values $\log M_0$ of about $\pm$ 0.4 and confirm the saturation of Ms at about 8.5:

$\log M_0 = 1.0\ Ms + 12.2$ for $Ms \leq 6.4$, (3.93)

$\log M_0 = 1.5\ Ms + 9.0$ for $6.4 < Ms \leq 7.8$, (3.94)

$\log M_0 = 3.0\ Ms - 2.7$ for $7.8 < Ms \leq 8.5$, and (3.95)

$Ms = 8.5 = \text{const.}$ for $\log M_0 > 22.8$ Nm. (3.96)

Also Ms-M_0 relations (and vice versa) show regional variability. According to Ambraseys (1990) the global relations (3.90) - (3.92) systematically underestimate Ms for events in the Alpine region of Europe and adjacent areas by 0.2 magnitude units on average. Abercrombie (1994) discussed possible reasons for the anomalous high surface-wave magnitudes of continental earthquakes relative to their seismic moment. This illustrates the need for regional scaling of moment-magnitude relationships even in the relatively long-period range.

For M_0 and body-wave magnitudes mb (of 1s period) Chen and Chen (1989) give the following global scaling relations (with saturation at mb = 6.5 for $\log M_0 > 20.7$):

$\log M_0 = 1.5\ mb + 9.0$ for $3.8 < mb \leq 5.2$, (3.97)

$\log M_0 = 3\ mb + 1.2$ for $5.2 < mb \leq 6.5$, (3.98)

and for M_0 and Ml for California (with saturation at Ml = 6.3 for $\log M_0 > 20.1$):

$\log M_0 = Ml + 10.5$ for $Ml \leq 3.6$, (3.99)

$\log M_0 = 1.5\ Ml + 8.7$ for $3.6 < Ml \leq 5.0$, (3.100)

$\log M_0 = 3\ Ml + 1.2$ for $5.0 < Ml \leq 6.3$. (3.101)

Average scaling relations among mb, Ms and M_0 for plate-margin earthquakes have been derived by Nuttli (1985). They yield practically identical values as the equations (3.93)-(3.95) for M_0 when Ms is known while the deviations are not larger than about a factor of 2 when using mb and Eqs. (3.97) and (3.98).

The need for regional relationships between M_0 and magnitudes is particularly evident for Ml. When calculating M_0 according to Eqs. (3.98) and (3.100) for California and comparing them with the values calculated for a relationship given by Kim et al. (1989) for the Baltic Shield

$\log M_0 = 1.01\ Ml + 9.93$ for $2.0 \leq Ml \leq 5.2$ (3.102)

we get for Ml = 2.0, 4.0 and 5.0, respectively, values for M_0 which are 3.5, 5.4 and 16.6 times larger for California than for the Baltic Shield. Using instead an even more local relationship for travel paths within the Great Basin of California (Chávez and Priestley, 1985), namely

$\log M_0 = 1.2\ Ml + 10.49$ for $1 \leq Ml \leq 6$ (3.103)

we get for the same magnitudes even 9, 21 and 32 times larger values for M_0 than for the Baltic Shield according to Eq. (3.102).

3.6.4 Scaling relations of M, M_0 and E_S with fault parameters

Scaling relations of magnitude, seismic moment and energy with fault parameters are used in two ways:

1) to get a rough estimate of relevant fault parameter when M, M_0 or E_S of the event are known from the evaluation of instrumental recordings; or
2) in order to get a magnitude, moment and/or energy estimates for historic or even prehistoric events for which no recordings are available but for which some fault parameters such as (maximum possible) length of surface rupture and/or amount of surface displacement can still be determined from field evidence.

The latter is particularly important for improved assessment of seismic hazard and for estimating the maximum possible earthquake, especially in areas with long mean recurrence times for strong seismic events. Of particular importance for hazard assessment are also relationships between macroseismic intensity, I, and magnitude, M, on the one hand (see Eqs. (3.22) to (3.28) in 3.2.6.7) and between ground acceleration and I or M, on the other hand. Unfortunately, the measured maximum accelerations for equal values of intensity I scatter in the whole range of I = III to IX by about two orders of magnitude (Ambraseys, 1975). The

reason for this scatter is many-fold, e.g., human perception is strongest for frequencies around 3 Hz while acceleration and damage might be strongest for more high frequent ground motions. Also, damage depends not only on the peak value of acceleration but also depends on its frequency with respect to the natural period of the shaken structures and on the duration of strong ground shaking. For some structures damage is also more closely related to strong ground-motion displacement or velocity and not to acceleration.

Relationships between M_0, Ms, and E_S with various fault parameters are mostly based on model assumptions on the fault geometry, rupture velocity and time history, ambient stress and stress drop etc. But sometimes these fault parameters can, at least partially, be confirmed or constrained by field evidence or by petrophysical laboratory experiments. As for other scaling relations discussed above, global relationships can give only a rough orientation since the scatter of data is considerable due to regional variability. Whenever possible, regional relationships should be developed.

Sadovsky et al. (1986) found that for both crustal earthquakes and underground explosions the following relationship holds between seismic energy E_S (in erg) and the seismic source volume V_s (in cm^3) :

$$\log E_S = 3 + \log V_s \tag{3.104}$$

with V_s for earthquakes being estimated from the linear dimensions of the aftershock zone. This means that the critical energy density for both natural and artificial crustal seismic sources is about equal, roughly 10^3 erg/cm^3 or 100 J/m^3. It does not depend on the energy released by the event. E_S increases only because of the volume increase of the source. Accordingly, it is not the type of seismic source but the properties of the medium that play the decisive role in the formation of the seismic wave field. However, local and regional differences in ambient stress and related stress drop $\Delta\sigma \approx 2\mu\ E_S/M_0$ may modify this conclusion (see 3.3).

Fig. 3.39 shows the relation between seismic moment M_0 and the area A_r of fault rupture as published by Kanamori and Anderson (1975). A_r is controlled by the stress drop $\Delta\sigma$; as $\Delta\sigma$ increases for a given rupture area, M_0 becomes larger. One recognizes that intraplate earthquakes have on average a higher stress drop (around 10 MPa = 100 bars) than interplate events (around 3 MPa). The data in Fig. 3.39 are also well fit by the average relationship suggested by Abe (1975), namely:

$$M_0 = 1.33 \times 10^{15}\ A_r^{3/2} \tag{3.105}$$

which is nearly identical with the relation by Purcaru and Berckhemer (1982):

$$\log M_0 = (1.5 \pm 0.02) \log A_r + (15.25 \pm 0.05) \tag{3.106}$$

with M_0 in Nm and A_r in km^2. Eq. (3.106) corresponds to the theoretical scaling relation derived by Chen and Chen (1989) for a modified Haskell model with the assumption L = 2W (L - length and W- width of fault rupture, $A_r = LW = 0.5\ L^2$) and an average displacement $\overline{D} = 4.0 \times 10^{-5}$ L. Note that experimental data indicate also other aspect ratios L/W up to about 30 (e.g., Purcaru and Berckhemer, 1982).Wells and Coppersmith (1994) gave another relation between moment magnitude and A_r :

$$Mw = (0.98 \pm 0.03) \log A_r + (4.07 \pm 0.06) \qquad (3.107)$$

derived from a very comprehensive data base of source parameters for historical shallow-focus earthquakes (h < 40 km) in continental interplate or intraplate environments.

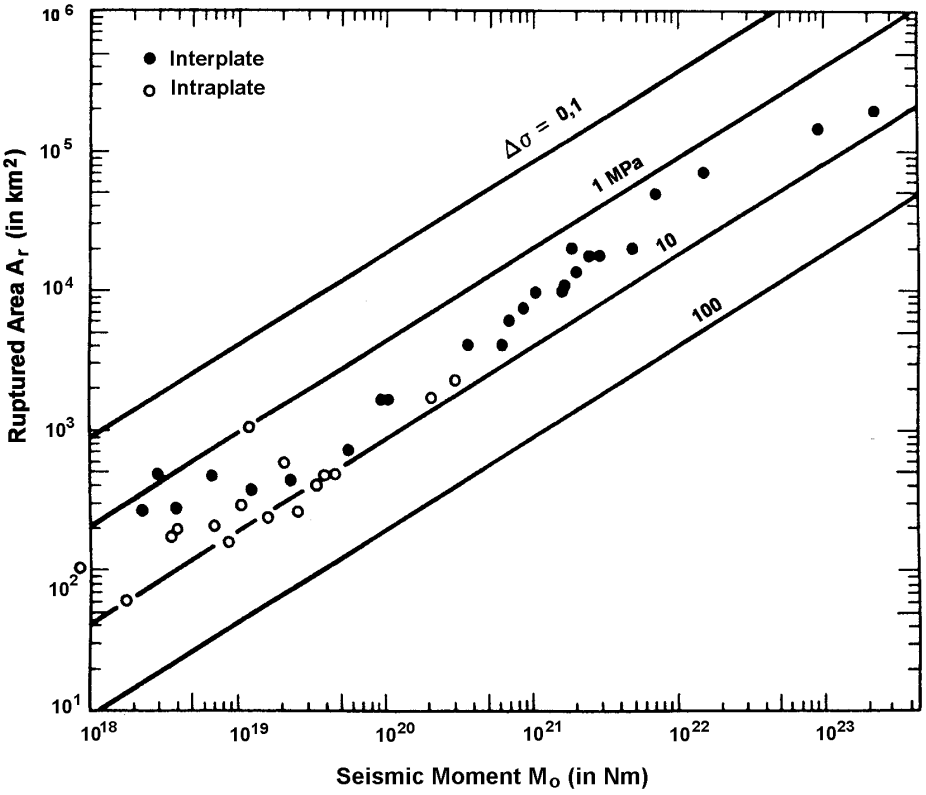

Fig. 3.39 Relation between area of fault rupture A_r and seismic moment M_0 for inter- and intraplate earthquakes. The solid lines give the respective relationships for different stress drop $\Delta\sigma$ (in MPa; 1 Pa = 10^{-5} bars) (modified from Kanamori and Anderson, Theoretical basis of some empirical relations in seismology, Bull. Seism. Soc. Am., Vol. 65, p. 1077, Fig. 2, 1975; © Seismological Society of America).

There also exists a linear log-log relation between L and M_0. Interestingly, for a given seismic moment L is on average about 6 times larger for interplate (strike-slip) events than for intraplate ones (see Fig. 3.40). The ratio α between average fault displacement (slip) $\overline{D}$ and fault length L is according to Scholz et al. (1986) $\alpha \approx 1 \times 10^{-5}$ for interplate and $\alpha \approx 6 \times 10^{-5}$ for intraplate events. Since this result is independent of the type of fault mechanism, it implies that intraplate faults have a higher frictional strength (and thus stress drop) than plate boundary faults but smaller length for the same seismic moments.

The slope of the curves in Fig. 3.40 is 0.5. This corresponds to a relation $M_0 \sim L^2$ (Scholz 1982; Pegeler and Das, 1996) which is only valid for large earthquakes (M > about 6.5 to 7). Then the width W of the fault is already saturated, i.e., equal to the thickness of the brittle fracturing zone in the lithosphere. Depending on heat flow and composition, the seismogenic zone in the crust is about 10 to 30 km thick. Accordingly, for large earthquakes, the growth of the fault area with increasing M_0 is in the length direction only.

Recently, there has been some serious debate on the scaling of large earthquakes and their ratio α (Scholz, 1994 and 1997; Romanowicz 1994; Romanowicz and Rundle, 1993 and 1994; Sornette and Sornette, 1994; Wang and Ou, 1998). Romanowicz (1992), who prefers to scale slip not with length but with width, even gives a relationship of $M_0 \sim L$ in case of very large earthquakes. In contrast, Hanks (1977) showed that earthquakes with rupture dimensions smaller than this seismogenic thickness scale according to $M_0 \sim L^3$ which is equivalent to Eq. (3.104).

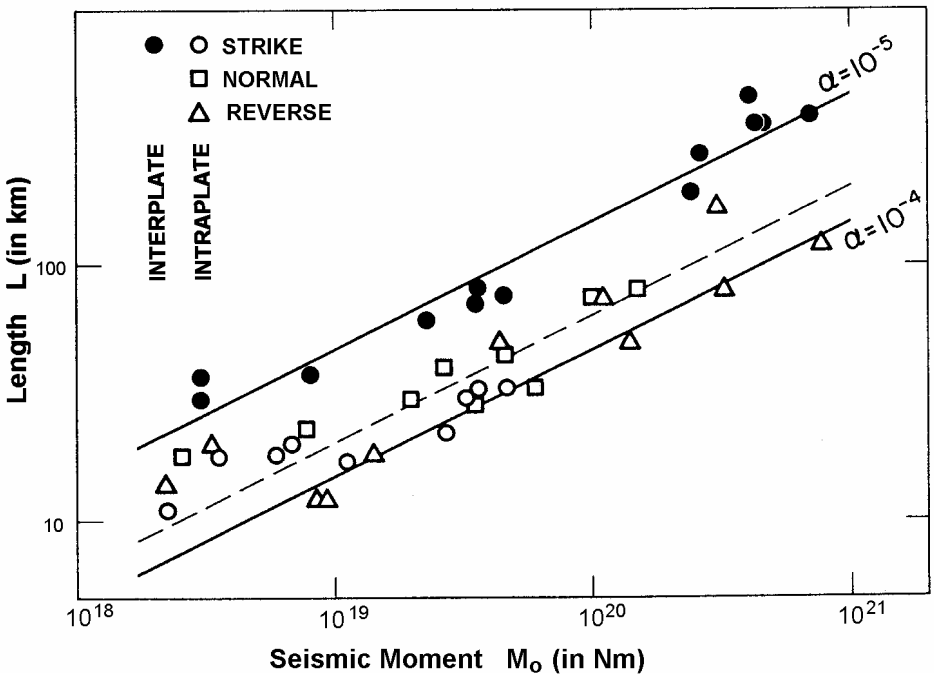

Fig. 3.40 Fault length L versus seismic moment M_0 for large inter- and intraplate earthquakes. The solid lines give the respective relationship for the ratio $\alpha = \overline{D}/L$ (modified from Scholz, Aviles, and Wesnousky, Scaling differences between large interplate and intraplate earthquakes, Bull. Seism. Soc. Am., Vol. 76, No. 1, p. 68, Fig. 1, 1986; © Seismological Society of America).

According to an older data compilation shown in Fig. 3.41 the correlation between source length L, magnitude M and energetic class K is not very good. Relations given by various authors for events in different environments often differ strongly.

Ambraseys (1988) published relationships derived from the dimensions of fault surface ruptures for Eastern Mediterranean and Middle Eastern earthquakes (with L - observed fault length in km, $\overline{D}$ - relative fault displacement in cm, M_{SC} - predicted surface-wave magnitudes):

$$M_{SC} = 1.43 \log L + 4.63 \qquad (3.108)$$

and

$$M_{SC} = 0.4 \log (L^{1.58} \ \overline{D}^{\,2}) + 1.1. \qquad (3.109)$$

They yield results which are in good agreement with those by Nowroozi (1985) for Iran but they differ significantly from the respective relations given by Tocher (1958) for Western USA and from Iida (1959) for Japan (see curves 1 and 2 in Fig. 3.41).

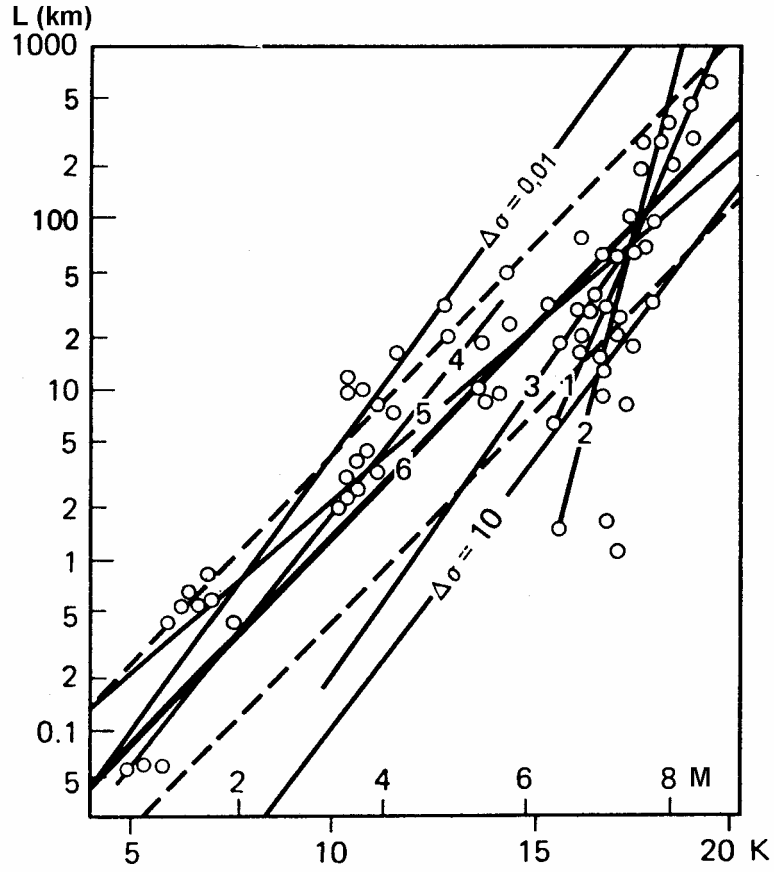

Fig. 3.41 Correlation of source length L with magnitude M and energetic class K according to data from various sources (e.g., curve 1 by Tocher, 1958, curve 2 by Iida, 1959; curve 6 average by Riznichenko, 1992). Thin straight lines: related stress drops $\Delta\sigma$ are given in MPa; broken lines mark the limits of the 68% confidence interval with respect to the average curve 6 (modified from Riznichenko, 1992, Fig. 3; with permission of Springer-Verlag).

Khromovskikh (1989) analyzed available data for more than 100 events of different faulting types from different seismotectonic regions of the Earth. He derived 7 different relationships between magnitude M and the length L of the rupture zone, amongst them those for the following regions:

a) the Circum-Pacific belt: $M = (0.96 \pm 0.25) \log L + (5.70 \pm 0.34)$ (3.110)
b) the Alpine fold belt: $M = (1.09 \pm 0.28) \log L + (5.39 \pm 0.42)$ (3.111)
c) rejuvenated platforms: $M = (1.25 \pm 0.19) \log L + (5.45 \pm 0.28)$ (3.112)

and compared them with respective relationships of other authors for similar areas.

Other relationships for estimating L (in km) when Ms is known were derived by Chen and Chen (1989) on the basis of their general scaling law based on the modified Haskell source model. These relationships clearly show the effect of width saturation:

$$\log L = Ms/3 - 0.873 \quad \text{for} \quad Ms \leq 6.4 \tag{3.113}$$

$$\log L = Ms/2 - 1.94 \quad \text{for} \quad 6.4 < Ms \leq 7.8 \tag{3.114}$$

$$\log L = Ms - 5.84 \quad \text{for} \quad 7.8 < Ms \leq 8.5. \tag{3.115}$$

The same authors also gave similar relations between the average dislocation $\overline{D}$ (in m) and Ms, namely:

$$\log \overline{D} = Ms/3 - 2.271 \quad \text{for} \quad Ms \leq 6.4 \tag{3.116}$$

$$\log \overline{D} = Ms/2 - 3.34 \quad \text{for} \quad 6.4 < Ms \leq 7.8 \quad \text{and} \tag{3.117}$$

$$\log \overline{D} = Ms - 7.24 \quad \text{for} \quad 7.8 < Ms \leq 8.5 \tag{3.118}$$

while Chinnery (1969) derived from still sparse empirical data a linear relation between magnitude M and $\log \overline{D}$ (with $\overline{D}$ in m) for the whole range $3 < M < 8.5$

$$M = 1.32 \log \overline{D} + 6.27 \tag{3.119}$$

which changes to

$$M = 1.04 \log \overline{D} + 6.96 \tag{3.120}$$

when only large magnitude events are considered.

Probably best established are the relations which Wells and Coppersmith (1994) have determined for shallow-focus (crustal) continental interplate or intraplate earthquakes on the basis of a rather comprehensive data base of historical events. Since most of these relations for strike-slip, reverse and normal faulting events were not statistically different (at a 95% level of significance) their average relations for all slip types are considered to be appropriate for most applications. Best established are the relationships between moment magnitude Mw and rupture area (see Eq. (3.107)), surface rupture length (SRL) and subsurface rupture length (RLD) (both in km). They have the strongest correlations (r = 0.89 to 0.95) and the least data scatter:

$$Mw = (1.16 \pm 0.07) \log (SRL) + (5.08 \pm 0.10) \tag{3.121}$$

$$Mw = (1.49 \pm 0.04) \log (RLD) + (4.38 \pm 0.06) \tag{3.122}$$

$$\log (SLR) = (0.69 \pm 0.04)\, Mw - (3.22 \pm 0.27) \tag{3.123}$$

$$\log (RLD) = (0.59 \pm 0.02)\, Mw - (2.44 \pm 0.11) \tag{3.124}$$

Comparing Eqs. (3.123) and (3.124) it follows that in general the surface rupture length is only about 75% of the subsurface rupture length.

The correlations between Mw and $\overline{D}$ as well as $\overline{D}$ and SLR are somewhat smaller (r = 0.71 to 0.78):

$$Mw = (0.82 \pm 0.10) \log \overline{D} + (6.693 \pm 0.05) \quad (3.125)$$

$$\log \overline{D} = (0.69 \pm 0.08) M_w - (4.80 \pm 0.57) \quad (3.126)$$

$$\log \overline{D} = (0.88 \pm 0.11) \log (SLR) - (1.43 \pm 0.18) \quad (3.127)$$

$$\log (SLR) = (0.57 \pm 0.07) \log \overline{D} + (1.61 \pm 0.04). \quad (3.128)$$

Wells and Coppersmith (1994) reason that the weaker correlation may reflect the wide range of displacement values for a given rupture length (differences up to a factor 50 in their data set!). These authors also give relations between SLR and the maximum surface displacement which is, on average, twice the observed average surface displacement while the average subsurface slip ranges between the maximum and average surface displacement.

Chen and Chen (1989) also derived from their scaling law the following average values:

- rupture velocity v_r = 2.65 km/s;
- total rupture time T_r (in s) = 0.35 (s/km) × L (km); (3.129)
- slip velocity dD/dt = (2.87 - 11.43) m/s.

However, v_r and dD/dt usually vary along the fault during the fracture process. From teleseismic studies we can obtain only spatially and temporally averaged values of fault motion but the actual co-seismic slip is largely controlled by spatial heterogeneities along the fault rupture (see Fig. 3.8). Large slip velocities over 10 m/s suggest very high local stress drop of more than 10 MPa. (Yomogida and Nakata, 1994). On the other hand, sometimes very slow earthquakes may occur with very large seismic moment but low seismic energy radiation (e.g., "tsunami earthquakes"). This has special relevance when deriving scaling relations suitable for the prediction of strong ground motions (e.g., Fukushima, 1996).

Scaling relationships between fault parameters, especially between D and L, are also controlled by the fault growth history, by age and by whether the event can be considered to be single and rare or composite and frequent (e.g., Dawers et al., 1993; Tumarkin et al., 1994). There exist also scaling relations between fault length and recurrence interval which are of particular relevance for seismic hazard assessment (e.g., Marrett, 1994).

Using Eqs. (3.108), (3.110)-(3.112) and (3.121), one gets for a surface rupture length of 100 km magnitudes M = 7.5, 7.7, 7.6, 7.95 and 7.4, respectively. Knowing the Ms or Mw and calculating L and $\overline{D}$ according to Eqs. (3.114)-(3.118), (3.123) and (3.126), one gets for magnitude 7.0 L = 36 km and 41 km, $\overline{D}$ = 1,4 m and 1,1 m and for magnitude 8.0 L = 145 km and 200 km, $\overline{D}$ = 3.8 m and 5.2 m. The good agreement of the calculated values for magnitudes 7 and the stronger disagreement for magnitudes 8 are obviously due to the

growing difference between Ms (used in the relations by Chen and Chen, 1989) and Mw (used in the relations by Wells and Coppersmith, 1994) for Ms > 7 (saturation effect). For the rupture duration we get according to Eq. (3.129) for Ms = 7 and 8 approximately 13 s and 51 s, respectively.

3.6.5 Similarity conditions

Under certain assumptions there exist several conditions of static (geometric) and dynamic similarity. With the assumption of a constant stress drop one gets

$$W/L = k_1 \quad \text{i.e., a constant fault aspect ratio} \quad \text{and} \tag{3.130}$$

$$\bar{D}/L = k_2 \quad \text{i.e., constant strain } \alpha. \tag{3.131}$$

One can combine Eqs. (3.130) and (3.131) with the definition of the seismic moment $M_0 = \mu \bar{D} W L = \mu k_1 k_2 L^3$ and get $M_0 \sim L^3$ which is valid for source dimensions smaller than the thickness of the seismogenic layer. In addition there is a dynamic similarity, namely, the rise time t_r required for reaching the total displacement, i.e., the duration of the source-time function, is

$$t_r = k_3 \times L/v_{cr} \tag{3.132}$$

with v_{cr} the crack or rupture velocity (see Fig. 3.4). This is equivalent to the Eq. (3.131) of constant strain. Lay and Wallace (1995) showed that this results in period-dependent amplitudes of seismic waves which scale with the fault dimension. For periods $T >> t_r$ the amplitude does not depend on fault length L. This corresponds to the plateau of the "source displacement spectrum". But if $T << t_r$ then the amplitudes scale as $1/L^2$ or f^{-2} (see Fig. 3.5). This explains the saturation effect when analyzing frequencies higher than the corner frequency of the source spectrum.

Acknowledgments

The authors acknowledge with thanks careful reviews by A. Udias and W. Brüstle. Their comments have helped to improve and streamline the first draft of this Chapter. The German authors are also much obliged to G. Choy who careful proofread the English in their contributions to the whole manuscript. Special thanks go to the members of the IASPEI WG on Magnitude Measurements, particularly to J. Dewey, S. Gregersen, A. A. Gusev, R. A. Uhrhammer and K. Veith. Discussions with these members and complementary information provided by them enabled the Editor to complete the sub-chapter on magnitudes and the information sheet IS 3.2 on a common basis of understanding. This sets the stage for future standardization of magnitude measurements from digital data and for reaching agreement on a more precise and unique specific magnitude nomenclature. It is also acknowledged that S. Wendt of the Observatory Collmberg, University of Leipzig, provided Figure 3 of the Data Sheet 3.1 and that F. Krüger from the University of Potsdam contributed a short complementary paragraph to sub-chapter 3.5 and related references on relative moment-tensor inversion.

Recommended overview readings (see References under Miscellaneous in Volume 2)

Richter (1958)
Aki and Richards (1980 and 2002)
Båth (1981)
Ben Menahem and Singh (1981)
Das and Kostrov (1988)
Duda (1989)
Scholz (1990)
Lay and Wallace (1995)
Udias (1999)